UNIVERSITÉ DU QUÉBEC À TROIS-RIVIÈRES

MÉTHODES AVANCÉES D'ANALYSE ET DE COMMANDE DU CONVERTISSEUR MULTINIVEAU DE TYPE PONT EN H POUR VARIATEURS DE VITESSE

THÈSE PRÉSENTÉE

COMME EXIGENCE PARTIELLE

DU DOCTORAT EN GENIE ÉLECTRIQUE

PAR

FILS PASCAL MPOMBOUM LINGOM

Juillet 2025

UNIVERSITÉ DU QUÉBEC À TROIS-RIVIÈRES
3739 - DOCTORAT EN GÉNIE ÉLECTRIQUE

Direction de recherche :

Mamadou Lamine Doumbia, Directeur de recherche
Université du Québec à Trois-Rivières

Joseph Song-Manguelle, Codirecteur de recherche
Shell International Exploration and Production Inc

Jury d'évaluation :

Alben Cardenas, Président
Université du Québec à Trois-Rivières

Mamadou Bailo Camara, Evaluateur externe1
Université Le Havre Normandie, France

Tahar Tafticht, Evaluateur externe2
Université du Québec à Abitibi-Témiscamingue

Mamadou Lamine Doumbia, Directeur de recherche
Université du Québec à Trois-Rivières

Joseph Song-Manguelle, Codirecteur de recherche
Shell International Exploration and Production Inc

Thèse soutenue le 16 Mai 2025

DÉDICACE

À mes parents, pour leur amour inconditionnel, leur soutien constant et indéfectible qui m'ont permis de poursuivre mes rêves. À mon épouse, pour sa patience, sa compréhension et son encouragement constant tout au long de ce voyage académique. Que ce travail soit le reflet de votre influence positive dans ma vie.

REMERCIEMENTS

Avant tout, je tiens à exprimer ma profonde gratitude à la **Direction des études** ainsi qu'au **Département de génie électrique de l'Université du Québec à Trois-Rivières** pour m'avoir offert l'opportunité de poursuivre ce parcours doctoral enrichissant.

Je souhaite adresser mes plus sincères remerciements à mon éminent superviseur, le **Professeur Mamadou Lamine Doumbia**, pour son soutien indéfectible tout au long de mes études doctorales. Son expertise remarquable, sa patience, sa motivation et son enthousiasme ont été des piliers essentiels dans l'avancement de mes travaux.

Je suis profondément reconnaissant envers mon co-directeur, **Dr Joseph Song-Manguelle**, pour m'avoir offert l'opportunité de mener cette recherche. Son encadrement rigoureux, ses connaissances précieuses et sa vision claire dans le domaine de l'électronique de puissance et des systèmes industriels ont été pour moi une source d'inspiration constante.

Je remercie chaleureusement tous **les membres de notre laboratoire** pour leur collaboration, leur disponibilité et les moments inoubliables partagés ensemble. Leur soutien, direct ou indirect, a été précieux pour mener à bien ce travail de recherche.

Enfin, je tiens à exprimer ma profonde reconnaissance à mes **parents**, à mon **épouse**, à mon **petit frère** ainsi qu'à mes **amis** pour leur amour, leur patience et leur soutien moral indéfectible tout au long de ces années.

RÉSUMÉ

Au cours des dernières décennies, parmi tous les convertisseurs multiniveaux disponibles sur le marché industriel, le convertisseur multiniveau de type pont en H est devenu une topologie majeure pour les systèmes d'entraînement électrique à convertisseur statique, en particulier dans les applications pétrolières et gazières, en raison de ses caractéristiques de modularité et de fiabilité. Cependant, ce convertisseur peut induire des distorsions de tension et de courant en raison du fonctionnement non linéaire de ses interrupteurs de puissance. Cela peut entraîner des pertes supplémentaires, des interférences électromagnétiques, ainsi que des couples pulsatoires susceptibles d'exciter des résonances électriques et mécaniques. De nos jours, il n'existe pas de critère de conception clairement défini pour guider les équipes d'ingénierie et de chercheurs dans l'analyse et le diagnostic des problèmes liés aux harmoniques de ces convertisseurs, en particulier lorsqu'ils fonctionnent avec des cellules défaillantes.

Cette thèse se focalise principalement sur le développement de nouveaux outils d'analyse et de commande du convertisseur multi-niveau de type pont en H fonctionnement normal et dégradé. Les développements théoriques proposées sont validés par des simulations numériques offline, couplée aux simulations en temps-réel, et en fin testés sur un prototype expérimental au laboratoire.

Mots-clés : Convertisseur multiniveaux de type pont en H, Fonctionnement normal et dégradé, Harmoniques, Machine électriques, Variateur de vitesse

ABSTRACT

Over the past decades, among the various multilevel converters available on the industrial market, the cascaded H-bridge multilevel converter has established itself as a leading topology for static converter-based electric drive systems, particularly in oil and gas applications due to its exceptional features of modularity and reliability. However, this converter can introduce voltage and current distortions due to the nonlinear operation of its power switches. This can lead to additional losses, electromagnetic interference, and pulsating torques that may excite both electrical and mechanical resonances. Currently, there is no clearly defined design criterion to guide engineering teams and researchers in analyzing and diagnosing issues related to the harmonics of these converters, mainly when operating with faulty cells.

This thesis focuses on developing new analysis and control tools for the H-bridge multilevel converter in normal and failure operating conditions. The suggested theoretical developments are validated through offline numerical simulations, coupled with real-time simulations, and finally tested on a scaled-down experimental prototype in the laboratory.
Index: Cascaded H-bridge multilevel converter, Normal and failure operation, Harmonics, Electric machines, Variable speed drives

TABLE DES MATIÈRES

LISTE DES FIGURES

LISTE DES TABLEAUX

LISTE D'ABRÉVIATIONS

CHB	Cascaded H-bridge
CHBMI	Chascaded H-bridge multilvel inverter
FC	Flying Capacitor
HiL	Hardware in the loop
MiL	Model in the loop
PWM	Pulse width modulation
RCP	Rapid Control Prototyping
PSP	Pumped storage power plants
VFD	Variable-frquency-drive
DC	Direct curent
AC	Alternative current
IM	Induction motor
PMSM	Permanent magnet synchronous motor

INTRODUCTION GENERALE

I. Contexte industriel du convertisseur CHB

Au cours des dernières décennies, des progrès technologiques significatifs ont été réalisés pour améliorer les performances énergétiques des systèmes d'entraînement électrique à convertisseurs statiques, où les machines électriques sont alimentées par des variateurs électroniques de vitesse [1], [2]. Ces technologies jouent un rôle crucial dans l'optimisation de l'efficacité énergétique, en particulier dans les applications industrielles et commerciales où la régulation précise de la vitesse et du couple est essentielle. L'intégration de convertisseurs de puissance, tels que les convertisseurs multiniveaux, permet de réduire les pertes énergétiques et d'améliorer la qualité de l'alimentation, ce qui est essentiel pour répondre aux exigences environnementales et économiques actuelles [3]. Dans ce contexte, les convertisseurs multiniveaux se sont imposés comme une solution viable pour les applications industrielles de moyenne et forte puissance [4]. Ils trouvent leur utilisation dans divers secteurs (Figure 0.1), tels que le domaine domestique, les véhicules électriques, le transport ferroviaire, urbain ou maritime, la propulsion marine, ainsi que dans les systèmes de conversion d'énergie électrique à partir de sources d'énergie renouvelable, comme l'éolien et le photovoltaïque [5-7]. Les convertisseurs multiniveaux, grâce aux avancées technologiques des semi-conducteurs de puissance et des processeurs de commande, sont capables de gérer des courants et des tensions élevés par la connexion en série et en parallèle des modules de puissance.

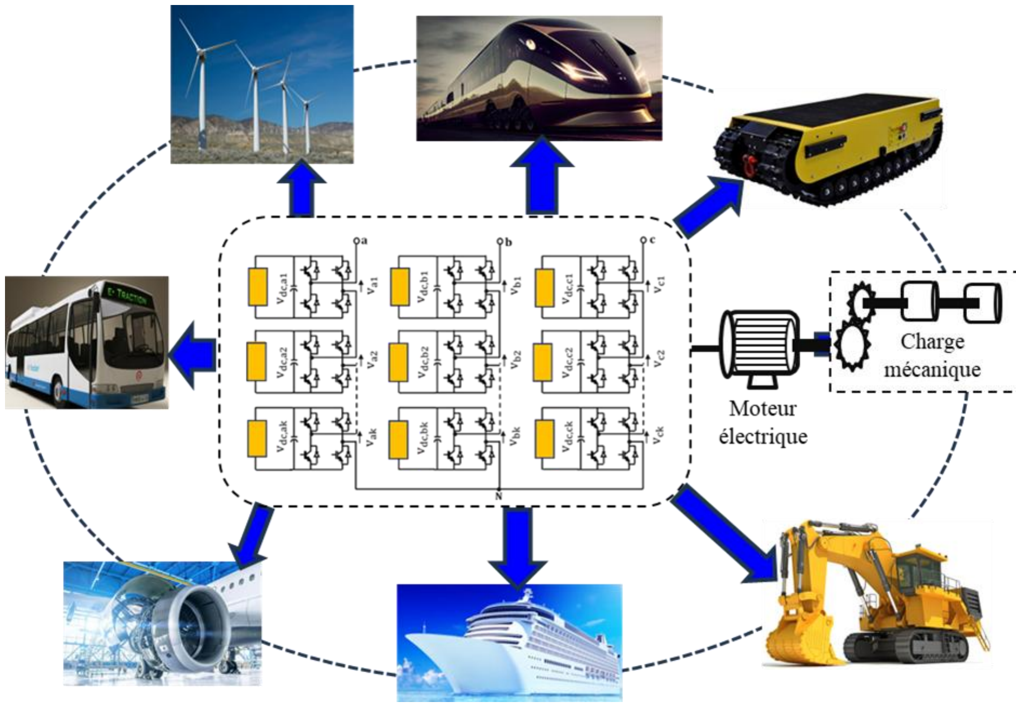

Figure 0. 1 : Quelques applications industriels pour convertisseur CHB.

En conséquence, la qualité de l’énergie électrique délivrée s’améliore considérablement par rapport aux convertisseurs classiques à deux niveaux, en raison de leur contenu harmonique réduit des formes d’onde de tension et de courant générées en sortie [8]. Ces caractéristiques confèrent aux convertisseurs multiniveaux une capacité accrue à satisfaire les exigences croissantes en termes de performance et de fiabilité dans les applications industrielles complexes, tout en minimisant les perturbations électriques et en optimisant le rendement énergétique.

Une large variété de topologies de convertisseurs multiniveaux a été proposée dans la littérature [9-11]. Ces convertisseurs sont classés en trois principales catégories : (i) la topologie à potentiel distribué, également connue sous le nom de Neutral Point Clamped (NPC), (ii) la topologie à condensateur flottant, ou Flying Capacitor (FC), et (iii) la topologie des ponts en H en série, ou Cascaded H-bridge (CHB). Parmi la large gamme de ces variateurs de vitesse, la topologie de type pont en H est devenue la plus courante dans de nombreux systèmes d'entraînement électriques industriels, où la fiabilité et la disponibilité sont d'une importance primordiale [12], [13]. Selon l'application, le convertisseur multiniveau de type CHB peut être configuré de manière symétrique, avec des sources DC égales, ou de manière asymétrique, avec des sources de tension continues inégales. Il est bien établi que, dans une configuration asymétrique, l'alimentation des cellules partielles par des tensions continues de valeurs différentes permet d'augmenter le nombre de niveaux de sortie du convertisseur sans en accroître la complexité structurelle. La configuration asymétrique offre l'avantage d'optimiser la résolution des niveaux de tension générés tout en limitant le besoin de composants de puissance [14].

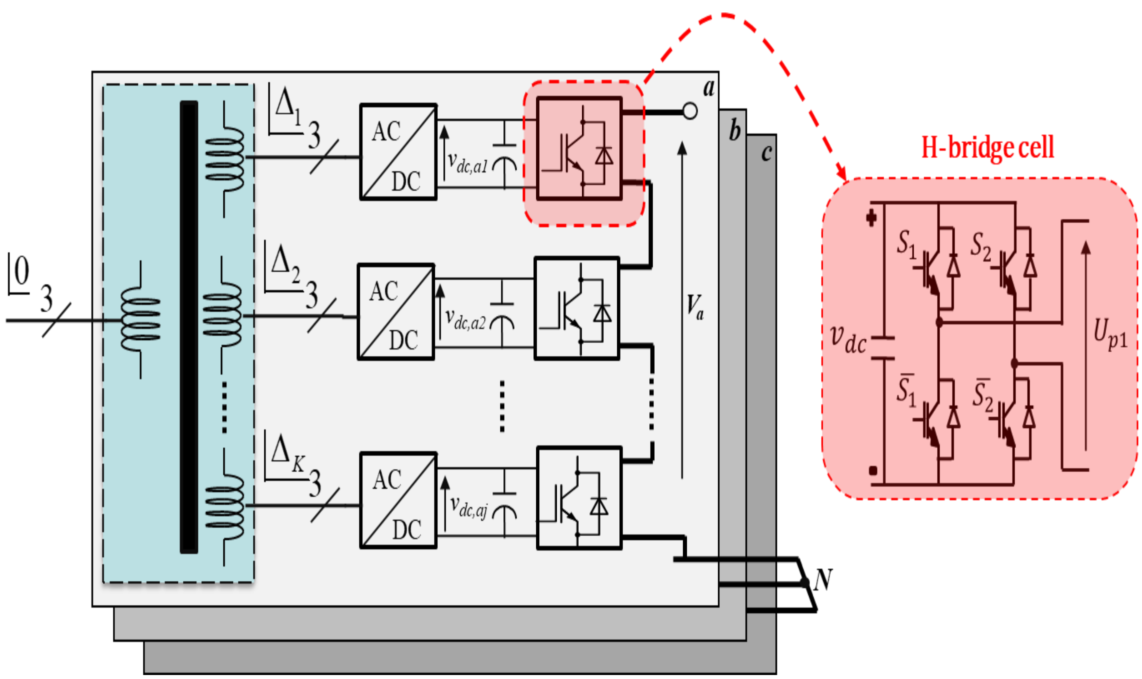

Figure 0. 2 : Configuration d'un convertisseur de type pont en H.

La Figure 0.2 présente la structure de puissance de la topologie CHB et la Figure 0.3 illustre la configuration générale d'un entraînement électrique à vitesse variable utilisé dans les applications de moyennes et hautes tensions telles que les pompes, les compresseurs, et les convoyeurs, entre autres. Ce système de configuration comprend l'association suivante : *Convertisseur statique - Machine électrique - Charge mécanique*, ou alternativement, *Mécanisme d'entraînement - Génératrice électrique - Convertisseur statique*. Ces architectures définissent le cadre d'étude de cette thèse, dans laquelle le variateur de vitesse sera basé sur la topologie de convertisseur multiniveau de type pont en H.

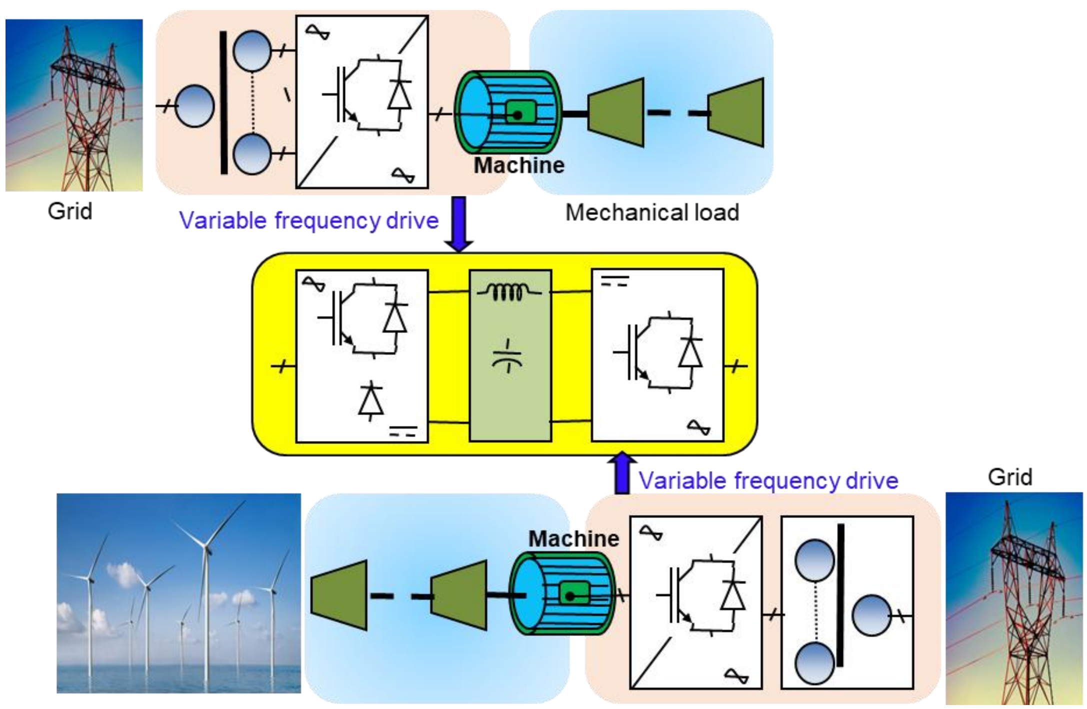

Figure 0. 3 : Configuration des systèmes d'entraînement de Machine à vitesse variable de très forte puissance.

II. Problématique

La topologie CHB présente plusieurs avantages qui expliquent son adoption croissante dans les systèmes de conversion d'énergie moyenne et haute tension. Sa modularité permet une extension facile du système en ajoutant ou en retirant des cellules H-bridge, ce qui simplifie la maintenance et l'adaptation aux exigences de puissance. Elle offre également une haute qualité de la tension de sortie, grâce à la synthèse de formes d'onde à plusieurs niveaux, réduisant ainsi les harmoniques et améliorant la performance globale. La structure CHB est par ailleurs fiable, capable de fonctionner en mode dégradé en cas de panne de certaines cellules. Son rendement élevé est attribuable à la réduction des pertes de commutation. De plus, cette topologie s'intègre facilement dans des systèmes à haute tension sans nécessiter de transformateur élévateur en sortie. Toutefois, elle présente aussi certains inconvénients, notamment une commande plus complexe en raison du nombre élevé d'interrupteurs à coordonner. Elle peut également poser des problèmes de répartition de puissance entre les modules, et elle nécessite plusieurs sources d'alimentation DC, ce qui peut compliquer l'infrastructure de l'entrainement. Cette thèse s'inscrit dans une démarche d'optimisation du fonctionnement des variateurs de vitesse utilisant les convertisseurs de type CHB.

Les harmoniques dans les variateurs de vitesse à convertisseur d'électronique de puissance représentent un problème majeur dans les systèmes électrotechniques modernes. Les composantes harmoniques générées par ces convertisseurs entraînent une distorsion des formes d'onde de tension et de courant, ce qui dégrade significativement la qualité de la puissance fournie aux charges. Cette dégradation se manifeste par divers effets indésirables, tels qu'un échauffement excessif des enroulements des moteurs, pouvant réduire leur durée de vie. De plus, dans l'entrefer des machines électriques, les harmoniques favorisent l'apparition de couples pulsatoires, susceptibles d'engendrer des vibrations mécaniques et une usure prématurée. Ils peuvent également provoquer des phénomènes de résonance électrique ou mécanique au sein des installations, amplifiant certains courants ou tensions à des niveaux potentiellement dangereux. La maîtrise des harmoniques s'avère donc essentielle pour garantir la fiabilité, la sécurité et la performance des systèmes à convertisseurs statiques.

À ce jour, aucun critère de conception bien défini ne permet aux ingénieurs d'analyser avec précision la propagation des harmoniques induites par les convertisseurs de type CHB, que ce soit en fonctionnement normal ou en mode dégradé. Le mode dégradé du convertisseur CHB correspond à une situation où une ou plusieurs cellules sont défaillantes sur une ou plusieurs phases du convertisseur.

L'analyse des effets des harmoniques dans les systèmes d'entraînement à vitesse variable demeure un défi en raison de la séparation traditionnelle entre l'ingénierie électrique et l'ingénierie mécanique. Ce cloisonnement disciplinaire limite la synergie nécessaire pour une compréhension globale du comportement électromécanique du système. D'un côté, les travaux en ingénierie mécanique se concentrent majoritairement sur les vibrations torsionnelles induites dans les moteurs, en s'appuyant sur l'étude de la dynamique des rotors (formes modales, vitesses critiques, contraintes de cisaillement, etc.). De l'autre, les recherches en ingénierie électrique portent principalement sur les aspects liés aux topologies de convertisseurs, aux algorithmes de commande et à l'analyse des harmoniques de tension et de courant. Ce manque d'intégration entre les approches limite l'identification et la modélisation précise des interactions entre les composantes électromagnétiques et mécaniques, pourtant essentielles pour évaluer l'impact réel des harmoniques sur la fiabilité et les performances globales des entraînements électromécaniques.

Par ailleurs, bien que plusieurs travaux récents aient cherché à améliorer la fiabilité de la topologie CHB en développant des algorithmes de compensation des défauts, ces approches ne parviennent pas à résoudre efficacement le problème des harmoniques engendrés en mode dégradé.

En effet, la littérature actuelle demeure lacunaire en ce qui concerne la formulation d'expressions analytiques permettant de quantifier les harmoniques de tension, de courant, ainsi que les harmoniques du couple électromagnétique dans l'entrefer de la machine, que ce soit avec ou sans mécanisme de compensation. En outre, les caractéristiques spectrales des différentes stratégies de compensation telles que le décalage de neutre, la réduction de crête, ou encore les techniques de modulation scalaire et vectorielle ainsi que leur impact sur les phénomènes de vibrations torsionnelles, restent à ce jour insuffisamment explorés et mal compris. Cette absence d'analyse approfondie limite la capacité à concevoir des solutions optimisées assurant à la fois la continuité de service et la qualité de la puissance dans les systèmes dégradés.

Cette thèse vise à combler les lacunes identifiées dans la littérature en s'attaquant à la problématique de la propagation des harmoniques électriques et électromécaniques induites par le convertisseur multiniveau de type pont en H, aussi bien en fonctionnement normal qu'en mode dégradé. Elle a pour objectif de fournir une compréhension approfondie des effets des défaillances sur la qualité de la puissance et sur le comportement global de la machine électrique. L'étude se concentre notamment sur l'évolution des harmoniques de tension et de courant, ainsi que sur les composantes harmoniques du couple électromagnétique généré dans l'entrefer, afin d'évaluer leur impact sur les performances, la fiabilité et les contraintes mécaniques subies par l'entraînement.

III. Objectif de la thèse

III.1. Objectif principal

Développer de nouveaux outils d'analyse et de commande permettant d'évaluer et de maîtriser la propagation des harmoniques dans les variateurs de vitesse en fonctionnement normal et dégradé, afin d'améliorer la performance et la fiabilité des applications industrielles variées.

III.2. Objectifs spécifiques (apports majeurs de cette thèse)

- Développer un modèle de commutation simplifié et généralisé pour le convertisseur CHB.

- Concevoir un modèle simplifié d'analyse harmonique applicable aussi bien aux systèmes avec un seul convertisseur qu'aux configurations multi-convertisseurs en parallèle.

- Établir les équations mathématiques décrivant les harmoniques de tension, de courant et du couple électromagnétique en fonctionnement normal et en mode dégradé, pour différents types de systèmes.

- Proposer une nouvelle méthode d'analyse graphique tridimensionnelle permettant de visualiser et d'interpréter le comportement harmonique du convertisseur CHB en modes normal et dégradé.

- Développer une méthode de commande tolérante aux défauts, généralisée et robuste, adaptée au convertisseur CHB fonctionnant en mode dégradé.

IV. Méthodologie et outils de validation

L'ensemble des développements théoriques, des outils analytiques, ainsi que des algorithmes de commande et de contrôle du convertisseur multiniveau de type pont en H, proposés dans le cadre de cette thèse, ont été rigoureusement validés à travers une démarche méthodologique combinant simulations numériques hors ligne, simulations temps réel et essais expérimentaux sur banc de test à échelle réduite en laboratoire. Des validations hybrides, alliant résultats expérimentaux et simulations numériques, ont également été mises en œuvre afin de garantir l'exactitude et la fiabilité des modèles théoriques et des expressions analytiques proposées.

IV.1. Outils de validation

Les simulations hors lignes ont impliqué le dimensionnement, la modélisation et l'implémentation du système machine électrique-convertisseur statique, ainsi que de ses algorithmes de modulation et de commande dans l'environnement MATLAB/Simulink.

Un ensemble de simulations temps réel ont été menés en utilisant les logiciels et équipements de l'OPAL-RT. Les deux méthodes de validations en temps réel suivantes ont été utilisés:

- Validation ''Model-in-the-Loop'' : le modèle du système (variateur de vitesse-machine électrique) et ses schémas de contrôle/modulation sont implémentés dans l'environnement RT-LAB, puis compilés et exécutés dans le simulateur en temps réel OP4510 ou OP4512.
- Validation ''Rapid Control Prototyping'': le modèle du système (partie étage de puissance) reste chargé dans le OP4510 ou OP4512, tandis que ses schémas de contrôle/modulation sont exportés vers le contrôleur externe OP8666. Le module RCP OP8666 est basé sur un microcontrôleur TI C2000 F28379D, qui prend en charge la programmation directe depuis MATLAB/Simulink, PSIM et le langage.

Une partie des travaux a été validée expérimentalement sur un banc d'essai de laboratoire, composé de neuf ponts en H, avec trois ponts connectés en série par phase, formant ainsi un onduleur triphasé à 7 niveaux en fonctionnement normal. Cet onduleur alimente une machine asynchrone triphasée de 3 kW et 4 pôles, couplée à une machine à aimants permanents de 8 pôles. Ce système a permis de valider expérimentalement la précision des expressions analytiques des couples pulsatoires dans l'entrefer du moteur à induction, résultant de l'interaction simultanée des composantes électromagnétiques et mécaniques. Pour simuler des cellules défaillantes, un contacteur de bypass est installé à la sortie de chaque pont monophasé.

IV.2. Méthodologie

Les outils d'analyse théorique développés s'appuient sur des expressions analytiques dans le domaine temporel permettant d'estimer avec précision les fréquences des tensions et des courants propres à chaque système étudié, ainsi que les composantes pulsatoires du couple électromagnétique dans l'entrefer de la machine. Ces expressions mathématiques sont validées par une analyse fréquentielle approfondie, reposant sur la transformée de Fourier (FFT) pour l'identification des harmoniques dominants, et sur l'utilisation du diagramme de Campbell pour l'analyse pulsatoire et l'évaluation des risques de résonance torsionnelle. L'ensemble de ces outils fournit une vision cohérente et détaillée du comportement harmonique du système, aussi bien en fonctionnement normal qu'en mode dégradé.

En raison de l'absence du capteur de couple dans le banc d'essai au laboratoire, les harmoniques du couple à l'entrefer du moteur sont obtenues par les étapes suivantes:

a) Transformation de Park des courants et tensions triphasés enregistrés ;
b) Calcul du flux statorique comme l'intégrale temporelle de la tension transformée
c) Reconstruction de la forme d'onde du couple à l'entrefer du moteur sur la base du diagramme montrée à la Figure 0.4;

d) Calcul de la transformée de Fourier pour extraire les fréquences harmoniques du couple électromagnétique. Les résultats sont présentés sous forme de diagrammes de Campbell, illustrant les zones critiques où les composantes de stress de torsion générées par l'onduleur CHB peuvent croiser les modes de résonance de l'arbre.

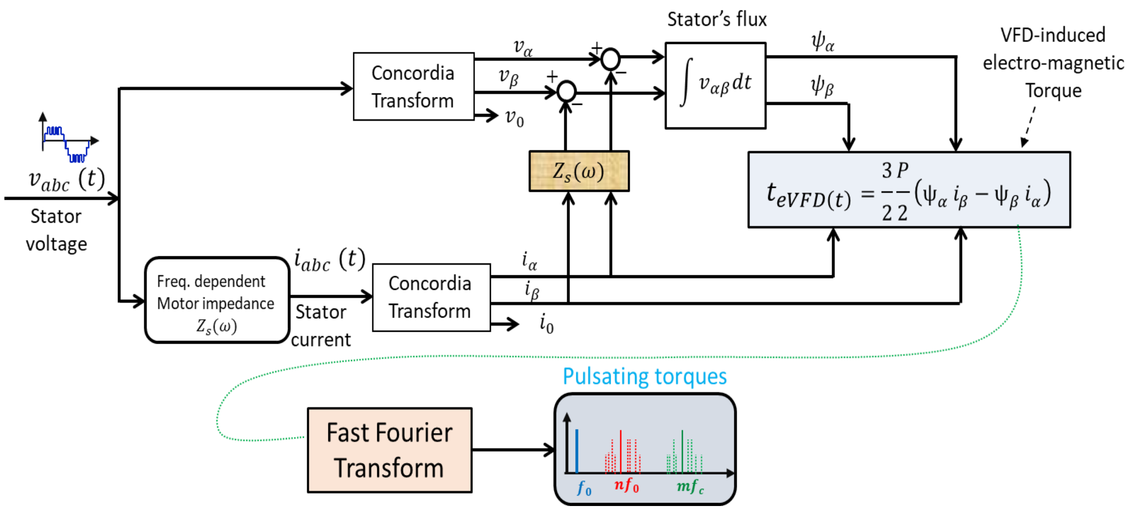

Figure 0. 4 : Principe de calcul des harmoniques de couple à partir des tensions et courant statoriques.

V. Contributions scientifiques et industrielles

V.1. Synthèse des contributions scientifiques

Les travaux de cette thèse ont donné lieu à une production scientifique et technique significative. À ce jour, cinq (05) articles ont été publiés dans des journaux scientifiques à comité de lecture, et six (06) communications ont été présentées dans des conférences internationales majeures, notamment. En parallèle, neuf (09) articles collatéraux ont été coécrits dans le cadre de collaborations actives avec d'autres chercheurs, reflétant la transversalité et la richesse des échanges scientifiques générés par cette recherche. De plus, ces travaux ont été soutenus par deux (02) subventions de recherche dans le cadre du programme **Mitacs Accélération**, soulignant leur pertinence appliquée et leur impact concret dans des contextes industriels réels.

❖ **Cinq (05) articles de journaux relatifs à cette thèse**

1. **P. M. Lingom**, J. Song-Manguelle, M. L. Doumbia, *et al*. "Graphical Analysis and Control of Cascaded H-bridge Multilevel Inverter Using Clarke Transformation with Neutral-Shift Strategy Under Non-Ideal Conditions," *IEEE Journal of Emerging and Selected Topics in Power Electronics*, Jan. 2025, DOI : 10.1109/JESTPE.2024.3523846.
2. **P. M. Lingom,** J. Song-Manguelle, M. L. Doumbia, *et al***. "**VFD-Induced Torsional Stresses in Pumped Hydropower Storage Applications**,"** *IEEE Access*, Vol.12, pp**.** 35984-36001, Feb. 2024.
3. **P. M. Lingom,** J. Song-Manguelle, M. L. Doumbia, *et al*. "A Comprehensive Review of Compensation Control Techniques Suitable for Cascaded H-bridge Multilevel Inverter Operation with Unequal DC-sources or Faulty Cells**.**" ***Energies***., Feb. 2024.
4. **P. M. Lingom,** J. Song-Manguelle, M. L. Doumbia, *et al***. "**A Power Quality Assessment of Electrical Submersible Pumps Fed by Variable Frequency Drives under Normal and Failure Modes**,"** *Energies*., vol. 16, no. 4, pp. 1–34, July. 2023.
5. **P. M. Lingom,** J. Song-Manguelle, M. L. Doumbia, *et al***. "**Electrical Submersible Pumps : A System Modeling Approach for Power Quality Analysis with Variable Frequency Drives**,"** *IEEE Transactions on Power Electronics***,** vol. 37, no. 6, pp.7039-7054**,** June 2022.

❖ **Six (06) articles de conférences relatifs à cette thèse**

1. **P. M. Lingom**, J. Song-Manguelle, D.L Mamadou, *et al*, "Pulsating Torque Harmonics in Electric Motors Driven by Carrier-Based PWM Multilevel Cascaded H-Bridge Inverter," *IEEE International Electric Machines & Drives Conference (IEMDC)*, Houston, Tx, USA, May 18 – 21, 2025.
2. **P. M. Lingom**, *et al*, "Inter-bridge Power-Sharing Capabilities in a Single-Phase 5-level Cascaded H-Bridge Inverter," *2024 IEEE Energy Conversion Congress and Exposition (ECCE)*, Phoenix, Arizona, USA, Oct. 20-24
3. **P. M. Lingom**, *et al*, "Comparison of Phase-Shifted and Phase-Disposition PWM Schemes an Asymmetrical Cascaded H-Bridge Converter," *IEEE Energy Conversion Congress and Exposition (ECCE)*, Phoenix, USA, Oct. 20-24
4. **P. M. Lingom,** J. Song-Manguelle, M. L. Doumbia, *et al*, "A Single-Carrier PWM method for Unifor Step Asymmetrical Multilevel Converters," *2023 IEEE Energy Conversion Congress and Exposition (ECCE)*, Nashville, TN, USA, Oct. 29-Nov. 2, 2023, DOI: 10.1109/ECCE53617.2023.10362685

5. **P. M. Lingom,** J. Song-Manguelle, M. L. Doumbia, *et al*, "Performance Evaluation of Multi-Modulation Single-Carrier PWM Strategies for Motor drive applications," *14th IEEE International Conference on Power Electronics and Drive Systems (PEDS)*, Montreal, DOI : 10.1109/PEDS57185.2023.10246565
6. **P. M. Lingom**, J. Song-Manguelle, M. L. Doumbia, *et al*, "A generalized modulation strategy for cascaded H-bridge Multilevel Inverter under Unequal DC Sources," *IEEE Energy Conversion Congress and Exposition (ECCE)*, Detroit, Oct. 9-13, 2022**,** DOI : 10.1109/ECCE50734.2022.9948005

❖ **Sept (09) autres articles de conférences comme co-authors durant la thèse**

1. S. P. Betoka, J. Song-Manguelle, **P. M. Lingom**, *et. al*, "Impact of Mechanical Stresses on Wind Turbine Drivetrain Components," *IEEE International Electric Machines & Drives Conference (IEMDC)*, Houston, Tx, USA, May 18 – 21, 2025.
2. H. Hamza, J. Song-Manguelle, **P. M. Lingom**, *et. al*, "Theoretical Analysis of Paralleled Cascaded H-Bridge Inverters Operating with Interleaved Phase-Disposition PWM for Variable Frequency Drives," *IEEE International Electric Machines & Drives Conference (IEMDC)*, Houston, Tx, USA, May 18 – 21, 2025.
3. Obinna, **P. M. Lingom**, *et al*, "High-Frequency Pulse Generator for Medium Voltage Motor Insulation Testing," *2024 IEEE Energy Conversion Congress and Exposition (ECCE)*, Phoenix, USA, Oct. 20-24
4. S. P. Betoka, **P. M. Lingom,** J. Song-Manguelle, M. L. Doumbia, *et al*, "Mechanical Stresses on Wind Turbine Drivetrain due to the Power Converters System" *2023 IEEE Energy Conversion Congress and Exposition (ECCE)*, Nashville, TN, USA, Oct. 29-Nov. 2, 2023.
5. S. P. Betoka Onyama, **P. M. Lingom,** J. Song-Manguelle, M. L. Doumbia, *et al*, "A Tool for Power Quality Assessment in Electric Submersible Pump Systems with Variable Frequency Drives" *Society of Petroleum Engineers (SPE) Guld coast section-Electric Submersible Pump Workshop*, the Woodlands, TX, USA, Sept, 2023, https://doi.org/10.2118/214710-MS
6. J. Menye, **P. M. Lingom,** J. Song-Manguelle, M. L. Doumbia, *et al*., "Effects of Control strategies on the Assessment of Power Converter losses in EV Drivetrains," *2023 IEEE Canadian Conference on Electrical and Computer Engineering (CCECE)*, Regina, Saskatchewan, Canada, Sept. 24-27, 2023, DOI: 10.1109/CCECE58730.2023.10288932
7. S. P. Betoka, **P. M. Lingom,** J. Song-Manguelle, M. L. Doumbia, *et al*, "Prediction of Mechanical Stresses on Wind Turbine Drivetrain due to the Power Converters System" *14th IEEE International Conference on Power Electronics and Drive Systems (PEDS)*, Montreal, Aug. 7-10, 2023, DOI : 10.1109/PEDS57185.2023.10246613

8. H. Hamza, **P. M. Lingom,** J. Song-Manguelle, M. L. Doumbia, *et al*, “A Review of Fault-Tolerant Control Methods for Cascaded H-Bridge Multilevel Inverters” *14th IEEE International Conference on Power Electronics and Drive Systems (PEDS)*, Montreal, Canada, Aug. 7-10, 2023., DOI : 10.1109/PEDS57185.2023.10246759
9. S. P. Betoka, **P. M. Lingom,** J. Song-Manguelle, M. L. Doumbia, *et al*, “An Interactive Tool for the Analysis of Mechanical Stresses on Wind Turbine Shafts,” *IEEE Energy Conversion Congress and Exposition (ECCE)*, Detroit, Michigan, Oct. 9-13, 2022**,** DOI : 10.1109/ECCE50734.2022.9947967

V.2. Contributions industrielles relatives à cette thèse

En complément des contributions scientifiques, les travaux de cette thèse ont été valorisés à travers deux projets industriels, réalisés en partenariat avec des entreprises dans le cadre de collaborations soutenues par le programme Mitacs, renforçant ainsi l’impact concret de la recherche.

- ❖ **Avril 2022 - Août 2023 : Canada Government Mitacs Accelerate Research Grant for Industrial research project (Application Ref. IT319712).**
  Project de recherche industrielle entre Opal-RT Technologies et L’UQTR : ‘’Rapid control Prototyping of Adjustable speed drive systems for Opal-RT coursewares with OP8666 module’’
- ❖ **Sept. 2021-May. 2022 : Canada Government Mitacs Accelerate Research Grant for Industrial research project (Application Ref. IT25920).**
  Project de recherche industrielle entre CFER-Technologies et L’UQTR **:** “A Simulation Tool for Power Quality of Electric Submersible’’

VI. Organisation de la thèse.

Cette thèse est organisée sous forme de compilation de publications scientifiques relatives à l’étude de la propagation des harmoniques en fonctionnement normal et dégradé dans l’interaction entre un convertisseur multiniveau de type pont en H, une machine électrique, et une charge mécanique. En dehors du chapitre 1, chacun des chapitres 2, 3, 4 constitue un résumé de chaque publication scientifique et présente les concepts clés, les analyses, ainsi que les résultats des simulations hors ligne et en temps réel, et des essais expérimentaux.

Le **chapitre 1** met en évidence les progrès réalisés, les lacunes encore présentes et les perspectives de recherche pour surmonter les limitations actuelles des convertisseurs CHB, dans le but d'améliorer leur fiabilité et leur performance dans des applications exigeantes.

Au **chapitre 2**, une étude s'est spécifiquement concentrée sur les systèmes d'entraînement électrique de forte puissance, rencontrés notamment dans les industries pétrolières et gazières, où il est crucial de comprendre les interactions entre les harmoniques électriques et les phénomènes électromagnétiques. Elle a porté sur l'intégration de systèmes impliquant des machines tournantes, telles que les pompes, les compresseurs, les turbines et les moteurs électriques, alimentées par des variateurs de vitesse. L'étude a traité en particulier des problèmes d'intégration liés à la fois au variateur et au câble de transmission, comme c'est le cas dans les applications de pompes submersibles électriques, où le variateur est situé en surface, tandis que le moteur est immergé à une distance pouvant dépasser 30 km.

Le **chapitre 3** présente une nouvelle approche d'analyse graphique tridimensionnelle du convertisseur CHB, en régime normal et dégradé, fondée sur une représentation vectorielle spatiale 3D permettant de diagnostiquer les déséquilibres de fonctionnement de l'onduleur. Une stratégie de commande généralisée, capable de compenser ces déséquilibres, y est également proposée. Enfin, l'étude examine l'impact des conditions non idéales sur la modification des spectres de tension et de courant de l'onduleur

Au **chapitre 4**, une étude de la propagation des harmoniques a également été étendue à l'interaction entre le convertisseur, la machine électrique et la charge mécanique dans les stations de transfert d'énergie par pompage, où plusieurs convertisseurs de puissance identiques sont connectés en parallèle et couplés par des inductances pour alimenter une machine triphasée. Dans ce type d'installation, des expressions analytiques permettant de quantifier et de prédire les fréquences des couples électromagnétiques causés par le variateur de vitesse en fonctionnement normal et dégradé ont été suggérées. Dans chaque étude de cas présenté, les harmoniques de couple pulsatoire obtenus ont été théoriquement discutés et analysés à l'aide des diagrammes de Campbell. Ces diagrammes ont été utilisés pour évaluer la plage de fonctionnement dans laquelle le convertisseur, en fonctionnement normal ou dégradé, pourrait exciter les modes de résonance torsionnelle de la charge mécanique.

CHAPITRE 1 : REVUE DE LITTERATURE

1.1. Introduction

Ce chapitre vise à fournir une vue d'ensemble des recherches existantes sur le convertisseur multiniveau de type pont en H, en mettant en lumière les principaux défis et les stratégies proposées pour y répondre. La première section explore les enjeux techniques fondamentaux liés à cette topologie, notamment l'amélioration de l'efficacité énergétique, l'équilibrage des sources DC, la simplification des algorithmes de contrôle, ainsi que l'amélioration de la fiabilité et de la qualité de puissance. La seconde section s'intéresse aux travaux récents portant sur le fonctionnement en mode dégradé des convertisseurs CHB, une problématique cruciale en raison de l'augmentation du nombre de semi-conducteurs et de la complexité des schémas de commande nécessaires pour compenser les défauts.

1.2. Défis techniques liés à la topologie CHB

Les convertisseurs multiniveaux de type pont en H (CHB) présentent plusieurs défis et enjeux techniques en raison de leur structure et de leur utilisation dans des applications exigeantes. Au cours des dernières décennies, de nombreuses recherches ont été réalisées sur la topologie de convertisseur multiniveau de type pont en H dans le but d’améliorer ses performances opérationnelles. Ces études soulèvent cinq problématiques principales:

i) **Amélioration de l’efficacité et du rendement** : Développement de méthodes de contrôle et de commande pour réduire les pertes par conduction et par commutation au sein du convertisseur [15].

ii) **Équilibrage et meilleure utilisation des sources d’alimentation DC** : Optimisation de la répartition de la puissance entre les cellules monophasées afin de garantir une utilisation équitable des sources d'alimentation [16].

iii) **Simplicité et rapidité des algorithmes de contrôle et de commande** : Mise au point d'algorithmes de contrôle et de commande plus rapides et plus simples [17].

iv) **Amélioration de la fiabilité et de la maintenabilité** : Développement de méthodes de contrôle et de commande tolérantes aux défauts, incluant des mécanismes de détection et de reconfiguration pour améliorer la fiabilité et la maintenabilité du système [18].

v) **Amélioration de la qualité de la puissance fournie par le convertisseur** : Élaboration de méthodes de contrôle et de commande visant à réduire la distorsion en tension et en courant à la sortie du convertisseur [19-21].

Parmi ces cinq défis techniques, le dernier, relatif à l’amélioration de la qualité de la puissance fournie par ce convertisseur, demeure particulièrement épineux pour l’ingénierie de l’électronique industrielle. Ainsi, bien que les autres problématiques soient également importantes, l’amélioration de la qualité de la puissance dans les variateurs de vitesse reste un domaine de recherche particulièrement exigeant, nécessitant des

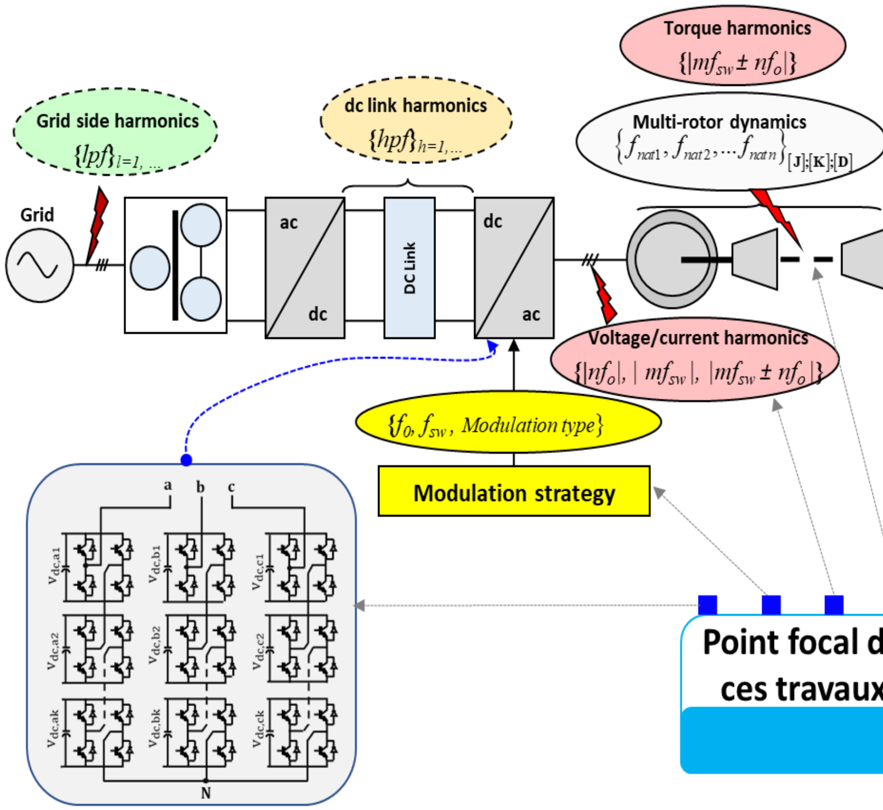

Figure 1. 1 : Contexte harmonique global et point focal des travaux recherche.

approches innovantes et une expertise approfondie pour répondre aux exigences des systèmes de forte puissance. La Figure 1.1 présente le contexte global des harmoniques dans les entraînements électriques à convertisseur statique. Les harmoniques générées par les convertisseurs de l'électronique de puissance sont souvent considérées comme des « tueurs silencieux » dans l'industrie des variateurs de vitesse.

1.3. Challenges liés à l'étude des harmoniques dans les variateurs de vitesse

L'étude des effets des harmoniques dans les entraînements à vitesse variable (VSD) représente un véritable défi en raison de la séparation traditionnelle entre les disciplines de l'ingénierie électrique et mécanique. Ce manque de synergie complique l'analyse globale du système électromécanique et limite la compréhension complète des interactions entre les harmoniques électriques et les phénomènes mécaniques tels que les vibrations et les couples pulsatoires.

Les publications en ingénierie mécanique se concentrent généralement sur l'analyse des vibrations torsionnelles dans les moteurs, en mettant l'accent sur la dynamique des rotors (formes modales, vitesses critiques, contraintes de cisaillement, etc.). En parallèle, les recherches en ingénierie électrique abordent principalement les topologies de convertisseurs, leurs stratégies de commande, ainsi que l'étude des harmoniques générées.

1.4. Etude des harmoniques en ingénierie électrique

Dans la configuration du système illustrée à la Figure 1.1, le variateur génère des harmoniques de tension haute fréquence, créant des pics de tension. Ces harmoniques sont le résultat du fonctionnement non linéaire des semi-conducteurs en commutation. Lorsqu'elles ne sont pas filtrées, ces harmoniques se propagent le long du câble, entraînant des distorsions et des pics de tension à l'entrée de la machine électrique [22].

Dans ce type de système, il est important d'évaluer les harmoniques à l'entrée du variateur pour respecter les normes comme IEEE 519 et celles de la Commission électrotechnique internationale [22], [23]. Le couple redresseur-transformateur aide à limiter les harmoniques côté réseau. Les harmoniques dans le lien DC proviennent surtout du redressement.

Des condensateurs bien dimensionnés sont utilisés pour réduire les ondulations en entrée de l'onduleur. Cependant, le vrai défi reste la prédiction et l'identification précise des fréquences harmoniques et interharmoniques en sortie de l'onduleur. Cette analyse est essentielle pour assurer une bonne qualité de puissance vers la machine d'entraînement.

Au-delà des pertes supplémentaires dans les enroulements des machines, qui accélèrent leur vieillissement, les harmoniques générées par l'onduleur créent des couples pulsatoires susceptibles d'exciter les résonances mécaniques de l'ensemble machine-charge, entraînant ainsi une détérioration prématurée des équipements [24]. La propagation des harmoniques dans l'interaction entre le convertisseur et la machine électrique augmente les risques d'excitation des résonances électriques et mécaniques au sein de ces systèmes [25]. Ces risques sont particulièrement préoccupants dans toutes les applications industrielles d'entraînement électrique à vitesse variable, telles que les éoliennes, les plateformes pétrolières, les stations de transfert d'énergie par pompage (STEP), ou « *pumped storage power plants* » (PSP) en anglais, et autres installations industrielles.

L'excitation des résonances peut conduire à des vibrations excessives, une usure prématurée des composants, et une réduction de la fiabilité et de la performance des systèmes [26].

L'approche classique pour l'analyse des harmoniques dans les systèmes d'entraînement consiste à modéliser l'ensemble du système, incluant le réseau électrique, le transformateur, le convertisseur statique, le moteur et la charge mécanique. Toutefois, cette méthode présente plusieurs contraintes majeures: des temps de simulation élevés pour atteindre le régime permanent, la nécessité de connaître en détail les topologies internes des variateurs de vitesse, ainsi que l’accès limité aux stratégies de commande, souvent propriétaires. De plus, la littérature ne propose pas de modèle simplifié et généralisé permettant d’étudier de manière efficace la propagation et en particulier la propagation réversible des harmoniques au sein de ces systèmes complexes.

Cette étude devient encore plus complexe lorsque le convertisseur fonctionne en mode dégradé, car les déséquilibres induits modifient significativement la génération, la propagation et l’interaction des harmoniques dans l’ensemble du système

1.5. Revue des travaux sur le fonctionnement dégradé des convertisseurs multiniveaux en pont en H

L’un des inconvénients associés à l’utilisation du convertisseur multiniveau de type pont en H est que l'augmentation du nombre de niveaux de tension de sortie entraîne une augmentation proportionnelle du nombre de semi-conducteurs de puissance et de cartes de commande associées. Cette croissance du nombre de commutateurs de puissance accroît la probabilité de défaillance d’un ou plusieurs modules de puissance.

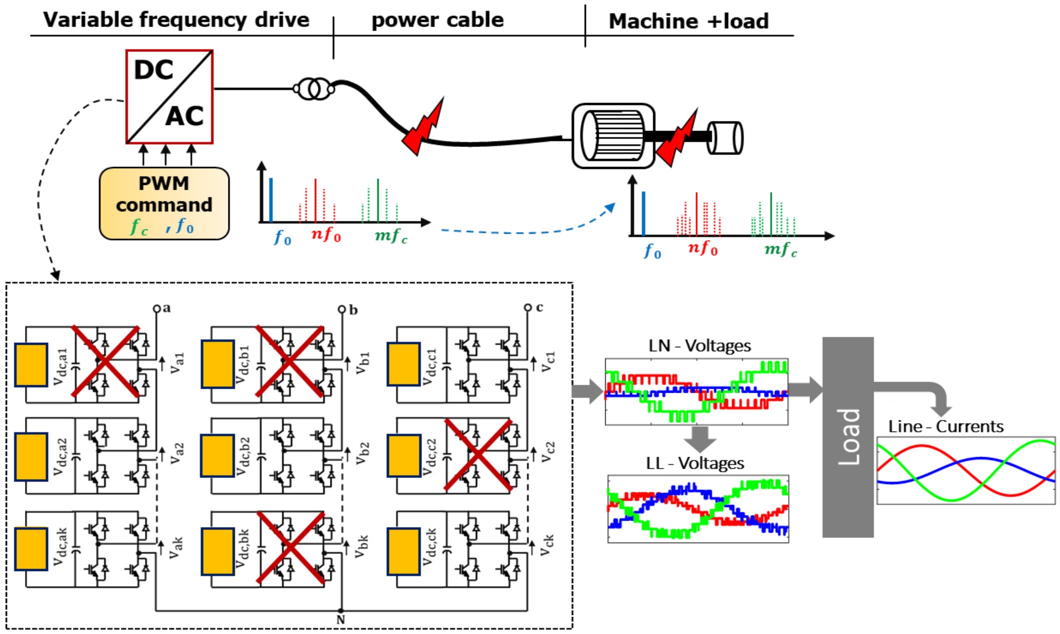

Figure 1. 2 : Fonctionnement du convertisseur CHB avec cellule défaillante.

Une défaillance dans ces modules peut provoquer une production de tensions et de courants déséquilibrés à la sortie du convertisseur comme illustré a la Figure 1.2.

Divers travaux dans la littérature ont proposé des stratégies de commande tolérantes aux défauts pour assurer le fonctionnement des convertisseurs CHBMI en présence de cellules défaillantes [27-29]. Ces stratégies permettent de maintenir des tensions de ligne équilibrées à la sortie de l'onduleur, même lorsque des déséquilibres de tension de phase surviennent à cause des cellules défaillantes. Le premier groupe utilise des méthodes de modulation par largeur d'impulsion (MLI) scalaire, qui reposent sur la comparaison de porteuses triangulaires avec une référence de tension sinusoïdale pour chaque phase [30], [31]. Le second groupe de stratégies emploie des techniques basées sur des vecteurs spatiaux, en particulier la modulation de largeur d'impulsion par vecteur spatial (SVPWM). Cette approche est largement documentée dans les références [32], [33].

Dans le groupe de la MLI scalaire, on retrouve principalement deux catégories de MLI sinus-triangle couramment évoquées dans la littérature [34]: MLI scalaire à porteuses déphasées où les porteuses sont déphasées horizontalement les unes par rapport aux autres [35]. MLI scalaire à porteuses à décalage de niveau où les porteuses sont décalées (verticalement) en niveau, ce qui modifie le profil harmonique et peut être avantageux pour certaines configurations de défauts [36].

Les deux techniques de compensation de défaut les plus couramment utilisées dans les schémas de modulation scalaire sont la méthode de décalage neutre conventionnelle et la méthode de réduction de crête [37], [38]. La méthode de décalage neutre ajuste les angles des tensions de phase du convertisseur pour maximiser l'amplitude des tensions de sortie entre phases. Cependant, déterminer les angles de tension de phase optimaux implique de résoudre un ensemble d'équations non linéaires en mode hors ligne, ce qui comporte plusieurs défis. Ces équations non linéaires présentent souvent plusieurs solutions, mais elles ne permettent pas toutes d'atteindre l'amplitude maximale des tensions de sortie entre phases. Trouver la solution optimale est donc crucial pour garantir la performance souhaitée. Pour pallier les limitations de la technique de commande par décalage neutre, des chercheurs ont proposé des méthodes tolérantes aux défauts par réduction de crête [39]. Ces méthodes consistent à ajuster les amplitudes des tensions de phase de référence pour équilibrer les tensions de ligne en sortie et maximiser l'utilisation des cellules encore opérationnelles. L'approche consiste à injecter une composante dynamique de moyenne min-max homopolaire dans les tensions de référence de la MLI, modifiant ainsi la nouvelle magnitude de référence de manière proportionnelle aux gains inégaux. Cependant, bien que cette méthode soit simple à mettre en œuvre, elle entraîne une augmentation des distorsions dans les formes d'onde de sortie de l'onduleur. Pour réduire ces distorsions, une autre méthode proposée dans [40], introduit une boucle de rétroaction avec un intégrateur afin d'améliorer la qualité des formes d'onde de tension de sortie de l'onduleur en conditions de fonctionnement déséquilibré. Toutefois, l'utilisation d'un intégrateur au niveau de l'étage de modulation peut compromettre la réponse dynamique du système, ce qui peut affecter la réactivité du système face aux variations rapides.

Contrairement aux méthodes à base de porteuses, les schémas de compensation basées sur la MLI vectorielle reposent sur une représentation orthogonale stationnaire des vecteurs de commutation de l'onduleur dans le repère $\alpha\beta$, avec un diagramme de vecteurs spatiaux présentant des coordonnées entières [41]. Ce diagramme, dans des conditions normales, est hexagonal, mais il change de forme et devient un polygone irrégulier à six côtés en présence de déséquilibres, comme des cellules défaillantes dans l'onduleur [42]. Sous des conditions déséquilibrées, la MLI vectorielle conserve de nombreux vecteurs de tension exploitables grâce aux états de commutation redondants de l'onduleur. Cette redondance permet de compenser les défauts en générant une tension de ligne équilibrée à la sortie AC de l'onduleur. Cela se fait en sélectionnant les vecteurs de référence en fonction des états de tension les plus proches dans le diagramme, ce qui assure un contrôle plus précis et une meilleure gestion des transitions de commutation. Les vecteurs de référence peuvent être sélectionnés de manière adaptative, ce qui rend la méthode plus efficace pour assurer la stabilité des tensions de ligne en cas de défaillances, tout en minimisant les distorsions harmoniques. Comparée aux stratégies de décalage neutre basées sur des porteuses, l'approche SVPWM offre une flexibilité accrue pour optimiser les commutations et réduire les pertes dans le convertisseur.

1.6. Conclusion

Ce chapitre a présenté une analyse des défis techniques et des solutions proposées pour améliorer les performances des convertisseurs multiniveaux de type pont en H. Nous avons identifié les problématiques majeures, telles que l'amélioration de l'efficacité énergétique, l'équilibrage des sources DC, la simplification des algorithmes de commande, l'amélioration de la fiabilité et de la qualité de puissance. Les méthodes de compensation proposées dans la littérature, centrées sur les techniques de modulation scalaire et vectorielle, ont également été présentées et discutées en lien avec le fonctionnement en mode dégradé. Ces approches permettent en effet de maintenir un fonctionnement stable du convertisseur en présence de défauts.

Cependant, un vide subsiste quant à l'analyse harmonique détaillée du convertisseur en mode dégradé, ainsi qu'à l'impact de ces méthodes sur la modification des spectres de tension et de courant. Ces limites sont abordées et approfondies dans les chapitres 2, 3 et 4.

CHAPTER 2 : A POWER QUALITY ASSESSMENT OF ELECTRIC SUBMERSIBLE PUMPS FED BY VARIABLE FREQUENCY DRIVES UNDER NORMAL AND FAILURE MODES

2.1 Introduction article 1

The electrical submersible pums systems generally consists of have à pulse-width-modulated (PWM) variable-frequency drive, a step-up transformer, an optional sinewave filter, a transmission line cable, and an induction motor coupled to a multi-inertia pump load. A successful ESP system integration requires complementary knowledge of rotor dynamics and VFDs operation and controls. These topics are substantially complex to be linked by the field engineering teams in their routine tasks. There is a need to understand the effects of VFDs on ESP's operation and possibly link these effects to their runtimes. It is evident that knowledge of how mechanical harmonics are sent back to the VFD is also necessary. There are no well-defined acceptance design criteria to guide the engineering teams when analyzing power quality in ESP systems. There are no international standards for the quality of VFD output power delivered downhole to ESP motor to date.

In a CHB VFD-ESP system operating with faulty cells, the neutral-shift method can maximize the fundamental component of the output line-to-line voltages while keeping them balanced even if the line-to-neutral voltages remain unbalanced. Such a goal is achieved by shifting the PWM reference phase voltage angles during the compensation mechanism. With such an approach, it is evident that the VFD output electric power spectrum is also shifted. However, because the locations of the modified harmonics are unknown, it is crucial for the completeness of the design to analytically calculate these harmonics in the frequency domain, assess their effects on the power transmission line, and evaluate the type of pulsating torque components they are generating in the motor's air gap.

2.2 General description of ESP systems

Electric submersible pumps are the most versatile and adaptative artificial lift methods in various oil and gas applications, from onshore to complex offshore, deepwater, or subsea applications [43], [44]. Figure 2.1 shows the generic electric power configuration of the ESP systems. Its installation typically includes a variable frequency drive (VFD), a step-up transformer for low voltage use, a surface cable, a downhole cable, a motor lead extension (MLE), connectors, and penetrators [45], [46]. The ESP motor is submerged at up to 30 km from the VFD, which is topside [47].

In such a system configuration, the rated VFD output voltage can be 4.16 kV or 6.6 kV, which should meet most voltage requirements in the field [48]. VFD output voltage is an unfiltered high-frequency pulse train that travels down the cable to the motor and reflects toward the VFD. A sinewave filter (SWF) can be installed at either the inverter output or on the secondary side of the step-up transformer, depending on the type of filter deployed [49]. The SWF is used to mitigate high-frequency harmonic traveling waves along the transmission cable. In addition, certain installations have a common-mode filter (CMF) installed at the output of the VFD to mitigate common-mode harmonics [50]

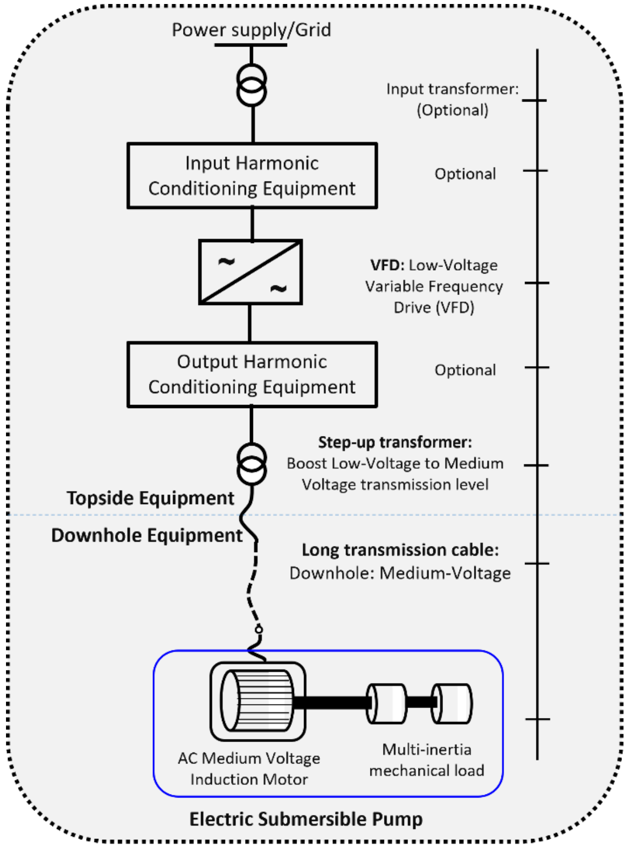

Figure 2. 1: Typical electric power configuration of an ESP system.

The electrical components of a downhole ESP system include a main downhole cable, a motor lead extension (MLE) cable, and an electrical submersible motor. The electrical submersible motors are dominated by three-phase two-pole squirrel cage induction-type electric motors with a nominal medium-voltage [51]. The downhole cables can reach depths from 300 to 4000 m. The surface and downhole main cables are usually round, while MLE cables are flat. Two VFD topologies are often used to power the ESP motor : the low-voltage (LV) VFD and the medium-voltage (MV) VFD. The LV ESP system is based on the classical two-level Inverter topology with a step-up transformer, as shown in Figure 2.2(a). The MV ESP system, in contrast, is built on a topology that does not use a step-up transformer and is based on a Neutral-point-clamped (NPC) inverter shown in Figure 2.2(b) or a multilevel cascaded H-bridge multilevel inverter (CHBMI) inverter shown in Figure 2.2(c).

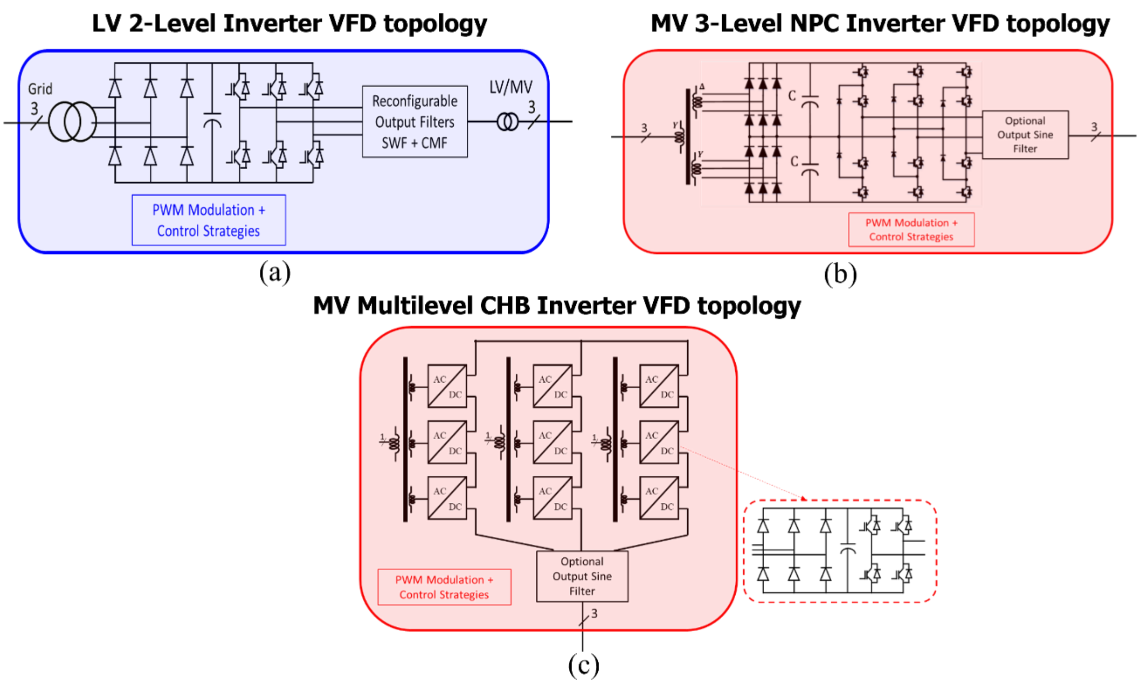

Figure 2. 2 : Investigated VFD topologies : (a) Low-Voltage 2-Level VFD Inverter (b) Medium-Voltage 3-Level NPC VFD Inverter (c) Medium-Voltage Multilevel CHB VFD Inverter.

2.3 Power quality challenges to operate ESP systems with VFDs

Anxieties about repetitive ESP failures have been reported mainly due to high-voltage stress along the cable, which might have been magnified by its impedance [52], [53]. Also, concerns about the torsional vibration phenomenon of rotating shaft systems have been continuously reported for several years from diversified ESP installations. The criticality of the issue varies from partial system failures to more severe failures, which may require the ESP system shutdown to avoid fatigue or harm to operators [54], [55]. It is estimated that the retrieval and re-installation of cable, pumping equipment, and service costs can exceed $100 000 for ESP system failure [56]. In addition, premature failures are undesired as they result in repair or replacement costs outside the scheduled maintenance window, and they induce unwanted downtime resulting in loss of production.

Several operators have reported issues leading to the loss of productivity by several operators, which are believed to be linked to both differential and common-mode harmonics and other aspects of poor power quality caused by VFD-generated waveforms. VFD voltage harmonics result from the modulation process utilized of controlling the power switches. Figure 2.3 illustrates ESP systems' common root cause failures resulting from poor power quality related to VFDs, including high-voltage stresses, repetitive voltage transients, reflected waves, common-mode harmonics, arcing currents, bearing currents, and pulsating torques [56]. The transmission line impedance can magnify VFD-generated harmonics if they are near line resonance modes. They create high-voltage stresses superposed to the regular system voltage along the cable and at the motor terminals. As a result, they can threaten the equipment insulation in a very short time [57]. Also, the Voltage and current harmonics produced by the VFD topologies are mixed in the motor’s air gap to generate the pulsating torque components. Some of these components might have relatively high magnitudes. Suppose some of these pulsating torque components have frequencies near one of the shaft’s natural frequencies. In that case, the shaft’s eigenmodes may be excited, potentially leading to mechanical shaft failures.

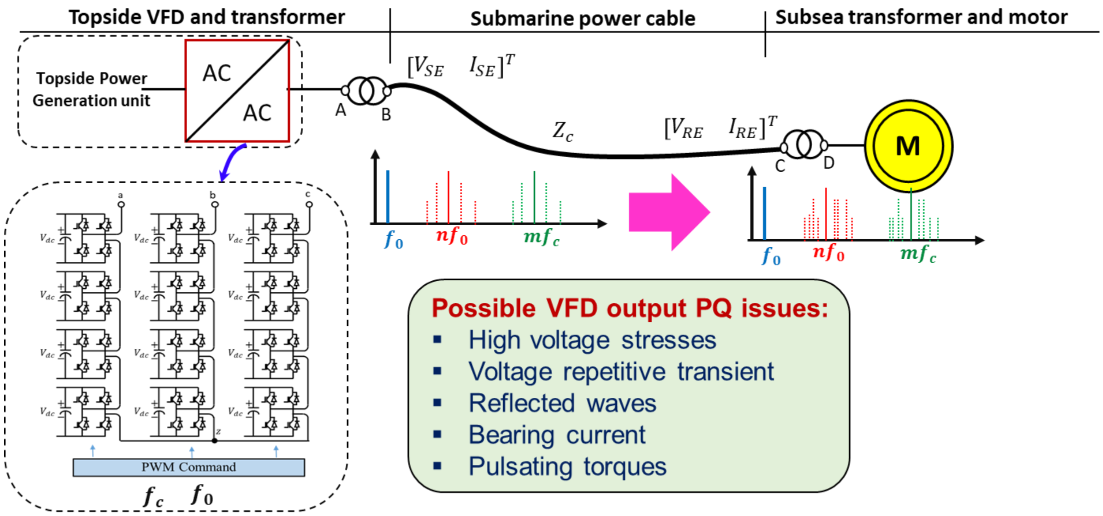

Figure 2. 3 : Some possible VFD output power quality issues

There are also process-induced excitation sources that may excite the resonance modes of a given ESP system. They include hydrocarbon fluid velocity, gas slug, and sand in the wells. This happens because load torque fluctuations may induce current pulsations from the motor windings to travel back to the VFD, potentially leading to failures [58-60]. As related to VFD-generated harmonics, these power quality problems pose significant risks that may shorten the ESP run-life and potentially induce failures, which involve significant damage and downtime [61]. Therefore, an ESP system must be appropriately designed and operated to prevent costly failures and production downtime.

Unbalanced voltage and current are other electrical power-related issues that frequently degrade the performance and shorten the life of the three-phase ESP systems. An unbalanced three-phase system can cause the ESP motor to experience poor performance or premature failure. Such risks are frequent in the specific case of a VFD-ESP system based on multilevel cascaded H-bridge inverter topology. For example, an unbalanced operation may result at least one H-bridge cell (failure of power devices or associated control hardware). This can lead to unbalanced VFD inverter output voltages and currents. The unbalanced voltages at the motor terminals cause a high unbalance of current, which can be 6 to 10 times larger than the voltage unbalance. Unbalanced currents induce high pulsating torque in the motor air gap, increase vibrations and mechanical stresses, and increase losses and motor overheating.

Each investigated ESP system has a pulse-width-modulated inverter, a step-up transformer, an optional sinewave filter, a transmission cable, and an induction motor coupled to a multi-inertia pump load. Therefore, a system integration analysis should be performed to understand the system behavior before installation. However, simulating such a system takes time and effort. It requires complex skill sets to design, model, and implement in simulation software. Unfortunately, in the industry, such exercises can be troublesome for field engineers due to the complexity of these systems. Hence, it is beneficial for drilling and artificial lift engineers involved in the design and selection of ESPs, to possess basic skills to perform high-level integrated system analysis of their systems, with minimum understanding of VFDs' operation and control strategies. This chapter proposes a simplified modeling approach to understand how VFDs impact the power quality of an ESP supplied through a transmission cable. It also explains how VFDs might excite mechanical-shaft torsional modes in such applications. The proposed model is an easy-to-use computer tool to replicate the steady-state behavior of low- and medium-voltage ESP systems under normal and abnormal operation modes, at different operating points, multiple cable cross-sections, short and long transmission distances, as well as low and high-power motors, combined with and without a sine filter. Engineers in charge of designing, selecting, integrating, and retrofitting ESP components and systems must have such tools for performing accurate power quality analysis.

Because ESP power quality is governed by the quality of the voltage generated by the VFD and the current flowing through the system, voltage and current behavior along the system have been deeply analyzed. Analytical expressions of different families of harmonics generated by each VFD and their accurate locations in the frequency domain, including inter-harmonics and common-mode harmonics, are derived, and discussed. Double-Fourier voltage harmonics resulting from two-level, neutral-point-clamped three-level, and cascaded H-bridge multilevel inverters are graphically presented in the frequency domain for easy understanding. The outcomes are crucial for a robust system integration design to avoid catastrophic failures. The results are also crucial for torsional analysis. International standards require a torsional analysis to ensure the integrity of the rotating shaft in its entire operating range [62-65]. Therefore, the magnitude and frequencies of the pulsating torque components in the motor airgap are needed for such evaluation.

2.4 Modeling of passive components of ESP systems

Figure 2.4 shows a generic example of an ESP system configuration circuit currently used in the oil and gas industry. Figure 2.5 shows the simplified single-phase electric model of the same system for the electrical resonance investigation. As explained in previous section, the VFD is represented as a controlled voltage source. The transformer is represented by its RL impedance, and the motor is represented by its steady-state impedance [66]. The transmission cable is a multiple pi-section network (e.g., one per km). A pi-section is formed using lumped R, L, and C elements. The interconnection of multiple inertias constructs the rotating shaft system through stiffness constants and viscous damping elements. This section describes how rotating shafts and cables are modeled for mechanical and electrical resonance analyses.

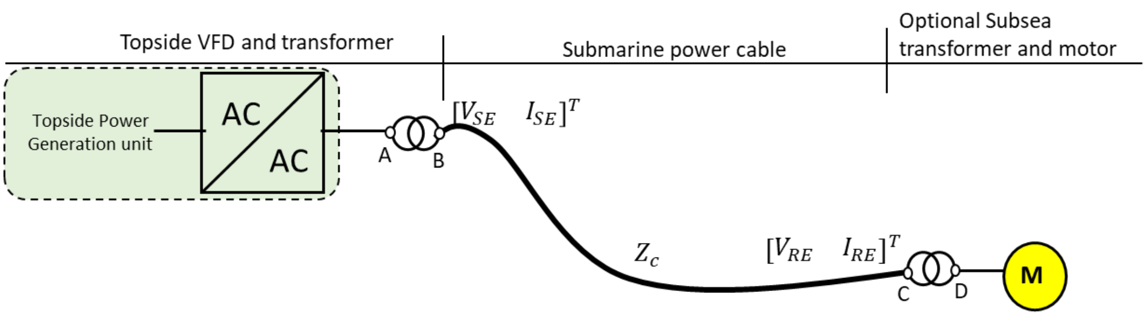

Figure 2. 4 : Typical electric power configuration of an ESP system : (a) Single-line diagram, (b) Electrical model.

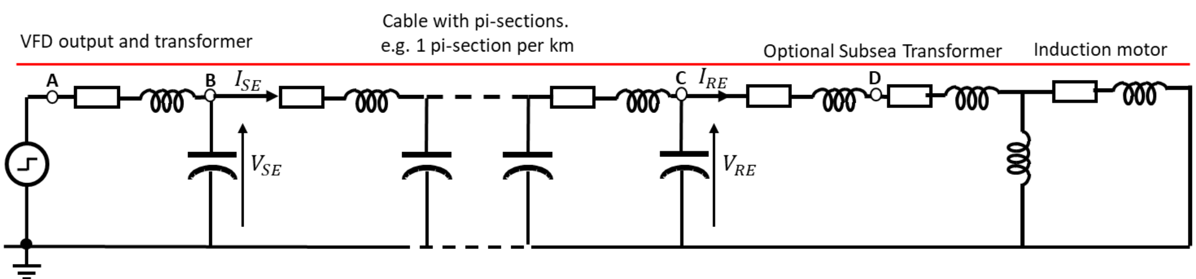

Figure 2. 5 : Single-line diagram of electrical ESP system model.

2.4.1 Modeling of transmission line cable

Figure 2.6(a) shows a series RLC circuit with a resistance R, an inductance L, and a capacitance C. Applying Kirchhoff's voltage law to the circuit gives the following relationships :

$$L\frac{di(t)}{dt}+Ri(t)+\frac{1}{C}\int i(t)dt=v(t) \tag{2.1}$$

$$\frac{di(t)^2}{dt}+2n\frac{di(t)}{dt}+k^2i(t)=0 \tag{2.2}$$

With $n=\dfrac{R}{2L}$ and $k^2=\dfrac{1}{LC}$

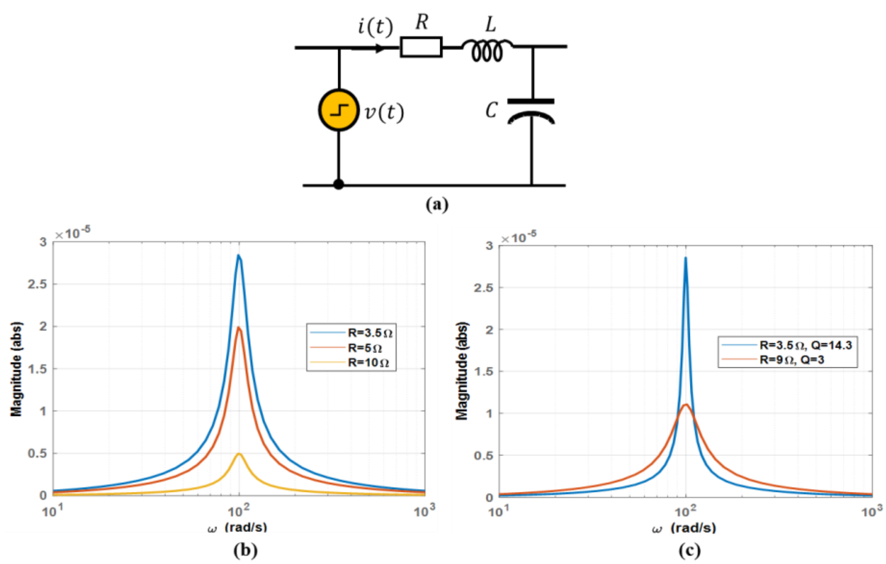

Figure 2. 6: Resonance phenomenon in single RLC circuit

Where $k=\omega_0$ is the system undamped natural frequency given by (1.3) :

$$L\omega_0-\frac{1}{C\omega_0}=0\rightarrow\omega_0=\frac{1}{\sqrt{LC}} \tag{2.3}$$

The relationship (2.1) is a second-order differential equation found in mechanical systems, as discussed in Subsection 2.2. Suppose the externally applied voltage $v(t)$ has a pulsating component near the undamped natural frequency ω_0. In that case, there is a continuous energy exchange between L and C, such that the energy stored in the inductance is transferred to the capacitor, back to inductance, repetitively. As a result, the current is only limited by the resistance, as shown in Figure 2.6(b) for different values of R. This energy exchange creates a power oscillation in the circuit and the current magnitude reaches its maximum value at the resonance frequency. This value can be significantly higher than the current value at frequencies far from the resonance frequency.

As shown in Figure 2.5, the cable can be split such that each certain length, for example, each kilometer, is represented by a pi-section. Because there are multiple LC branches, the system has multiple resonance frequencies. As a result, the voltage or current may reach very high values at those frequencies. Effects of load fluctuation can be analyzed with the same model. However, a current source replaces the motor model with multiple harmonics. Such analysis is suitable for understanding the effects of load dynamics (e.g., gas slugs) on the cable and its potentially destructive effects on the VFD.

2.4.2 Modeling of rotating shaft system

2.4.2.1. Shaft with one inertia

Figure 2.7 shows a rotating mechanical system with one inertia J, one damping coefficient D, and one stiffness constant K. The shaft's angular position is denoted θ.

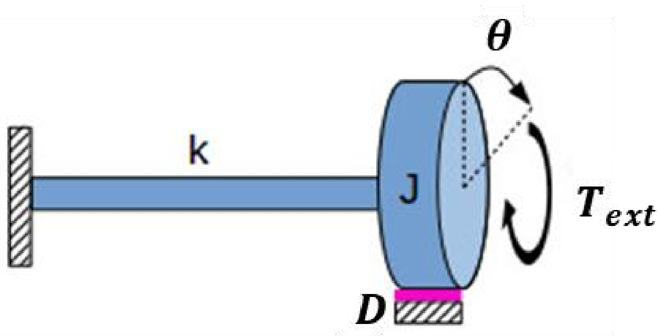

Figure 2. 7: A single-inertia rotating mechanical system.

Applying the 2nd Newton's law to the system gives :

$$\frac{d\theta(t)^2}{dt} + 2n\frac{d\theta(t)}{dt} + k^2\theta(t) = \frac{T_{ext}}{J} \tag{2.4}$$

With $n = \dfrac{D}{2k}$ and $k^2 = \dfrac{J}{K}$

This equation is identical to (2.1) given for an R, L, C-circuit. To better analyze the rotating system with one inertia, first it is assumed that the shaft system has no damping and the external applied torque T_{ext} is periodic such that :

$$T_{ext}(t) = T_a \sin(\omega_{nat} t) \tag{2.5}$$

In that case, the parameters in Eq (2.4) are to be set as follows : $n = 0$ and $k = \omega_{nat}$

Solving the differential equation in Eq (2.4) yields :

$$\theta(t) = \frac{T_a}{2\omega_{nat}}\left(\frac{1}{\omega_{nat}}\sin\left(\omega_{nat} t\right) - t\cos\left(\omega_{nat} t\right)\right) \tag{2.6}$$

According to (2.6), it is noticed that if an external torque component is applied to the shaft system with a frequency equal to the undamped natural frequency of the shaft, the resulting shaft position has two components :

i. One having the same pulsation as the shaft natural frequency, ω_{nat}, and a constante magnitude : $\frac{T_a}{2\omega_{nat}}$

ii. Another one also having the same pulsation as the natural frequency of the system, but with proportionally time-varying magnitude : $t \cdot \frac{T_a}{2\omega_{nat}}$

As a result, the amplitude of this component grows over time, even for small external torque magnitudes. An example of a system being excited is discussed in Figure 2.8. Figure 2.8(a) depicts the application of an external torque, T_{ext}, with a pulsation having a frequency equal to the natural frequency of the shaft. The resultant torque of the shaft, T_{shaft}, is linearly increasing with time, as shown in Figure 2.8(b). All motor's airgap torque components are fed to the electrical circuit as a controlled voltage source near the motor inertia. Consequently, VFDs should be designed to provide torque components with substantially low magnitude at specific frequencies to avoid the resonance excitation of the shaft. Process-induced mechanical torque, such as gas slugs, is supplied to the shaft model as an externally controlled voltage source for illustrative purposes only.

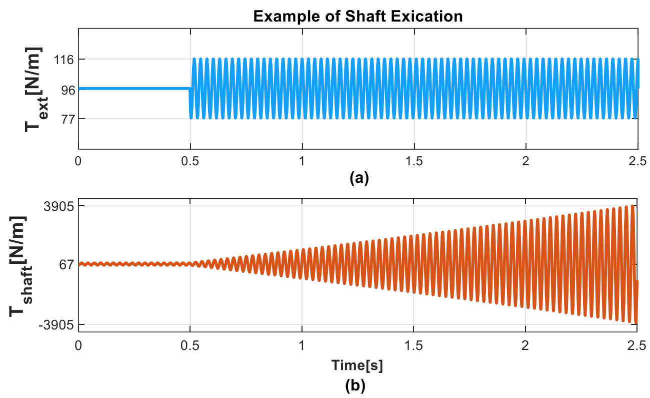

Figure 2. 8: Shaft's torque behavior (a) externally applied torque pulsating at a shaft's eigenfrequency ; (b) Shaft excited response

2.4.2.2. Shaft with multi-inertia

A generic representation of a multi-inertia shaft system is shown in Figure 2. 9. A dynamic shaft model can be established using the shaft element lumped parameters such as their mass moments of inertia, damping coefficients, and stiffness constants between inertias, derived from Newton's second law [67], shown in (2.7).

$$J\frac{d\theta(t)^2}{dt}+D\frac{d\theta(t)}{dt}+K\theta(t)=T_{ext} \tag{2.7}$$

Where θ is the vector of angular displacements of twists of individual disk to a common

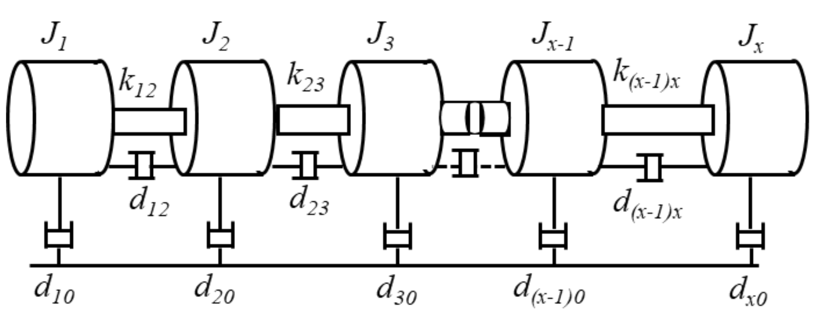

Figure 2. 9: A generic arrangement of a shaft system with multi-mass

reference en radians. J is the matrix of mass moment of inertia, D is the damping coefficient matrix, K is the stiffness matrix, and T_{ext} is the matrix of externally applied torque to the shaft system. With a base speed ω_b, these matrices are given as follows :

$$J = \frac{2}{\omega_b} diag\left(J_{1,} J_{2,} \ldots . J_x\right) \tag{2.8}$$

$$T_{ext} = \left[T_{1,} T_{2,} \ldots . T_x\right]^T \tag{2.9}$$

$$\begin{cases} K_{1,1} = k_{12} \\ K_{i,i} = k_{(i-1)i} + k_{i(i-1)} \\ K_{i,i+1} = K_{i+1,1} = k_{(i+1)i} = -k_{i(i+1)} \\ K_{n,n} = k_{(n-1)n} \end{cases} \tag{2.10}$$

$$\begin{cases} D_{1,1} = d_{12} + d_{10} \\ D_{i,i} = d_{(i-1)i} + d_{i(i-1)} + d_{i0} \\ D_{i,i+1} = D_{i+1,1} = d_{(i+1)i} = -d_{i(i+1)} \\ D_{n,n} = d_{(n-1)n} \end{cases} \tag{2.11}$$

Where $i = 2,3, \ldots .. x-1$. The undamped natural frequencies $\omega_{nat,i}$ of the system are calculated as the square root of the solutions of the characteristic equation :

$$\left[J^{-1} K - \lambda I\right] = 0 \tag{2.12}$$

$$\omega_{nat,i}^2 = \lambda_i \text{ and } i = 1,2,3, \ldots . x$$

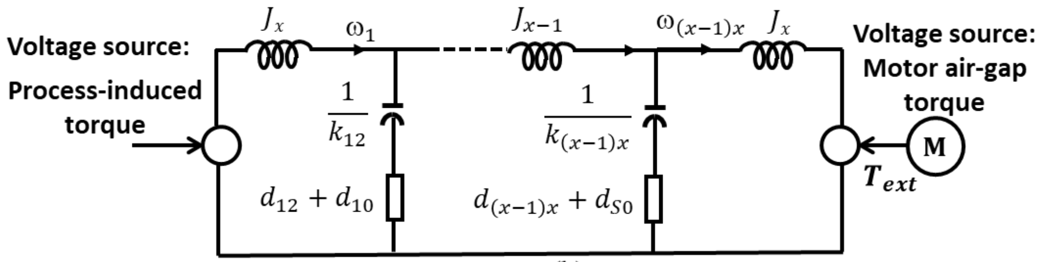

(b)

Figure 2. 10: Phenomenological electric analogy of the shaft system

Where I is a unity matrix**.** The system equations in (2.7) represent the shaft system dynamics. There are several other modeling approaches to represent the resulting equation of motion in the shaft system. Among these methods, the one based on its phenomenal equivalent electrical circuit model, as shown in Figure 2.10, is suitable for a torsional analysis [68-70].

According to the electromechanical phenological analogy [71], moments of inertia are equivalent to inductances, damping factors to resistances, and inverse stiffness constants to capacitances. Mechanical quantities also have their equivalent electrical quantities : angular velocity is equivalent to current, and torque to voltages [71].

2.5 VFD models for power quality analysis in ESP systems

2.5.1 Investigated VFD topologies for ESP systems.

Figure 2.11 shows the investigated VFD topologies, and their switching functions generated by the pulse-width-modulation (PWM) strategy : i) The low-voltage (LV) two-level inverter [Figure 2.11(a1)] ; ii) Three-level Neutral-Point-Clamped (NPC), [Figure 2.11(b1)] and iii) the multilevel cascaded H-bridge inverter systems [Figure 2.11(a1)]. The command strategy used is the sine-triangle PWM method.

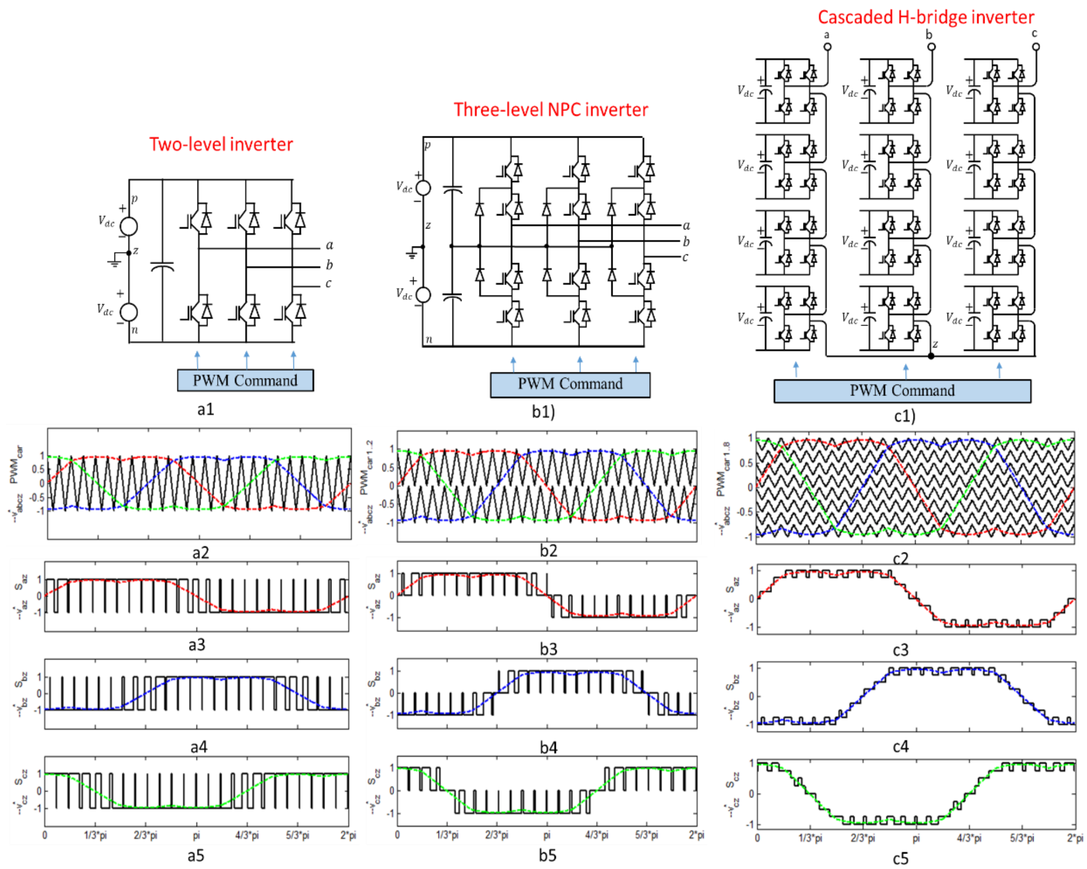

Figure 2. 11: Investigated VFD topologies for ESP and their PWM strategies and corresponding switching functions.

A sinusoidal reference wave is compared to one carrier signal per phase for the low-voltage two-level VFD, as shown in Figure 2.11(a2). For the NPC and the multilevel CHB (N-level) VFD topologies, there are $N-1$ triangles in phase-disposition, as illustrated in Figure 2.11(b2) and (c2), respectively. Such disposition of carriers produces fewer harmonics compared to other multicarrier-based PWM techniques [72]. The modulated command creates a set of switched three-phase voltages from a constant or slowly varying DC-link voltage through a switching command function.

2.5.2 VFD switching models for PQ analysis.

According to the above principle, the simplified switching function models two-level, three-level NPC, and *N*-level CHB VFD topologies are shown in Figures 2.12(a), (b), and (c), respectively. Only one phase is shown ; the other phases can be implemented by adding their respective references to the homopolar signal and comparing the results to the same carrier signals. A double-edge triangle carrier is compared to a reference voltage per phase. The average (min-max) homopolar component V_0 is injected into each reference phase voltage, such that the command pulses are equivalent to the space-vector PWM (SVPWM) pulses. A logic-to-real signal converter (''double'' block) is used because the result of each comparator is a Boolean number. The generated modulated PWM signals create a set of switched voltages from a constant or slowly varying DC-link voltage through a switching command function.

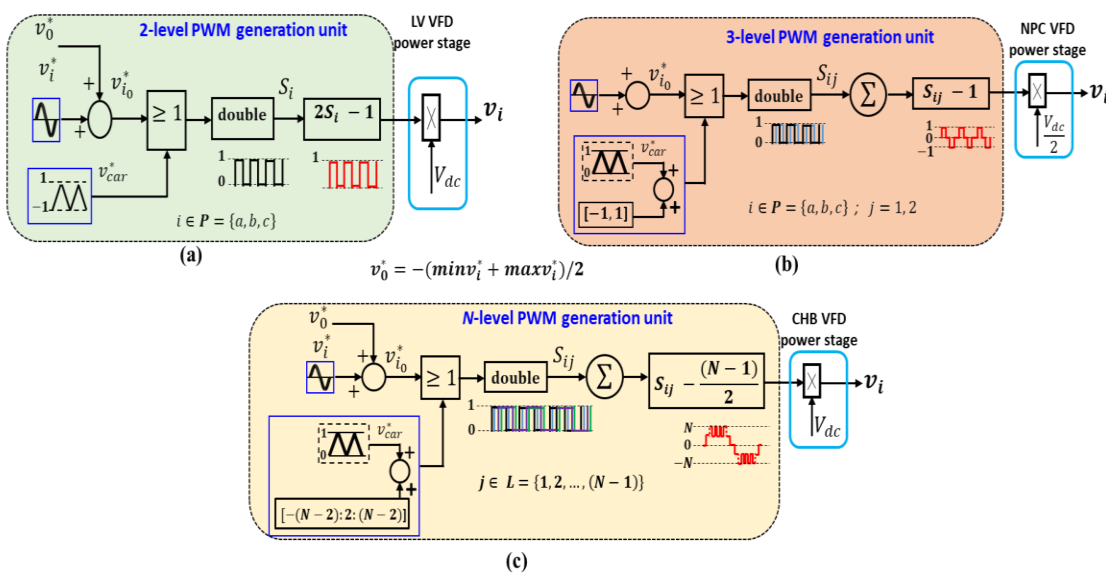

Figure 2. 12: VFD switching models : (a) two-level VFD ; (b) three-level NPC VFD ; (c) Multilevel CHB VFD

For a two-level VFD, V_{dc} is the total DC-link voltage. Only half of the total DC-link voltage is used for a three-level NPC VFD, and for an *N*-level model, V_{dc} is the DC-link voltage of a single power cell. Each switching model does not require a deep knowledge of the VFD's internal operation and control strategies. Regarding the harmonic analysis, the control strategies (PID, vector controls) do not impact the system performance at steady states. Such an approach simplifies the numerical simulation of VFD topologies.

2.6 Analytical expressions of VFD-induced voltage harmonics

This section provides detailed mathematical expressions of the harmonics at the output of each VFD topology discussed in Figure 2.11. These theoretical relationships are beneficial to understanding how each VFD creates high-frequency harmonic components that might excite the transmission cable and shaft system. In addition, they are needed to predict the location of the components in the frequency domain based on the VFD PWM's carrier frequency and fundamental frequency.

2.6.1 A general expression of a VFD switching function.

To mathematically formulate the switching function of each VFD in the steady state, the following assumptions are considered :

- ✓ VFD power switch is turned on and off with no rise and fall times.
- ✓ VFD DC-link is a constant DC-voltage.
- ✓ The voltage drops across the switch, and leakage currents through the VFD switches are zero.

The analytical switching function of any carrier-based PWM strategy applied to any VSI power topology can be obtained from a doublé Fourier transformation and written as follows [71-73] :

$$S_{aVFD}(t) = \sum_{m=0}^{\infty} \sum_{m=-\infty}^{\infty} S_{mn} \cos\left(n\omega_c t + n\omega_0 t + \theta_{mn}^{v}\right) \tag{2.13}$$

$$v_{aVFD}(t) = v_{aVFD}(t) \cdot V_{dc} \tag{2.14}$$

Where ω_c and ω_0 are the PWM triangle carrier and the fundamental frequencies ; θ_{mn}^{v} is the voltage harmonic phase-shift. S_{mn} and θ_{mn}^{v} are expressions dependent on the implemented PWM method. Only phase voltages are calculated with respect to a common reference point, chosen as the DC-link's mid-point. *m* refers to the integer multiple of the carrier frequency and *n* to the multiple of the fundamental frequency. The set of integers (m, n) is defined depending on the PWM strategy used. Different harmonic families can be derived depending on their values, as indicated in Figure 2.13(a). The following electrical harmonic families can be found in all voltage source inverters :

- ✓ If *m=0* and *n=0*, this corresponds to the DC component :
- ✓ If *m=0* and *n=1*, this combination represents the fundamental voltage component.
- ✓ If *m=0* and $n > 1$: this combination represents the baseband voltage harmonics. For three-phase systems, *n* can only be given in the form of negative and positive sequence component, i.e., in the following form : $n = 6l \pm 1$, with $l = 1, 2, 3, ...$

- ✓ If $m \neq 0$ and $n \neq 0$: this combination represents the sidebands or inter-harmonics. They are arranged around carrier harmonic components and are visible when even values m are paired with odd values of n and vice versa. Therefore, sum $m+n$ should always be an even number as shown in (2.12) :

  $m = 2,4,6,\ldots;\ n = \pm 1,3,5,\ldots$

  $m = 1,3,5,\ldots;\ n = \pm 2,4,6,\ldots$

$$f(t) = \frac{A_{00}}{2} + \sum_{n=1}^{\infty} A_{0n}\cos(n\omega_0 t) + \sum_{m=1}^{\infty} A_{m0}\cos(m\omega_c t) + \sum_{m=1}^{\infty}\sum_{\substack{n=-\infty \\ (n\neq 0)}}^{\infty} A_{mn}\cos((m\omega_c + n\omega_0)t)$$

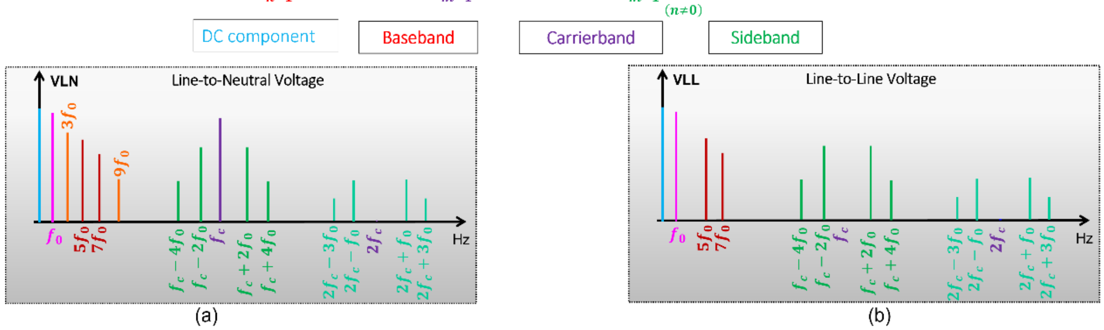

Figure 2. 13: General VFD output voltage harmonic families : (a) Line-to-Neutral voltage harmonics families (b) Line-to-Line voltage harmonics.

2.6.2 Harmonic expressions of investigated VFD topologies

The analytical model of a two-level switching function is given in (2.15). Where M is the modulation index such that $M = V_0 / V_{dc}$ with V_0 the output peak voltage maximum.

$$s_{az_{LV}}(t) = 1 + M\cos(\omega_0 t) \quad (2.15a)$$

$$+\frac{4}{\pi}\sum_{m=1}^{\infty}\sum_{n=-\infty}^{\infty} S_{mn}\cos(m\omega_c t + n\omega_0 t) \quad (2.15b)$$

The switching function expression of a three-level NPC VFD topology is given (2.16) :

$$s_{az_{NPC}}(t) = S_{01}\cos(\omega_0 t) \quad (2.16a)$$

$$+\sum_{n=2}^{\infty} S_{0,2n-1}\cos\left((2n-1)n\omega_0 t\right) \tag{2.16b}$$

$$+\sum_{m=1}^{\infty} S_{2m,0}\cos\left(2m\omega_c t\right) \tag{2.16c}$$

$$+\sum_{m=1}^{\infty}\sum_{n=-\infty}^{\infty} S_{2(m-1),2n}\cos\left(2\left(m-1\right)\omega_c t+2n\omega_0 t\right) \tag{2.16d}$$

$$+\sum_{m=1}^{\infty}\sum_{n=-\infty}^{\infty} S_{2m,2(n-1)}\cos\left(2m\omega_c t+2\left(n-1\right)\omega_0 t\right) \tag{2.16e}$$

The mathematical model of multilevel CHB VFD switching function is given in (2.17) :

$$s_{az_{CHB}}(t)=\frac{N-1}{2}S_{01}\cos\left(\omega_0 t\right) \tag{2.17a}$$

$$+\frac{N-1}{2}\sum_{n=2}^{\infty} S_{0,2n-1}\cos\left((2n-1)n\omega_0 t\right) \tag{2.17b}$$

$$+\frac{N-1}{2}\sum_{m=1}^{\infty} S_{2m,0}\cos\left(2m\omega_c t\right) \tag{2.17c}$$

$$+\frac{N-1}{2}\sum_{m=1}^{\infty}\sum_{n=-\infty}^{\infty} S_{2(m-1),2n}\cos\left(2\left(m-1\right)\omega_c t+2n\omega_0 t\right) \tag{2.17d}$$

$$+\frac{N-1}{2}\sum_{m=1}^{\infty}\sum_{n=-\infty}^{\infty} S_{2m,2(n-1)}\cos\left(2m\omega_c t+2\left(n-1\right)\omega_0 t\right) \tag{2.17e}$$

2.6.3 VFD-induced common-mode harmonics.

The common-mode currents and voltages can cause harmful side effects in the ESP system, such as additional losses, reflected waves, bearing currents, insulation stress, and magnetic saturation. common-mode voltage v_{CMV} . represents the difference between the entire three-phase system and the neutral or the ground. The common-mode current i_{CMV} travels in a single direction through all three wires, and it can only return to its source by using a different path, such as the neutral or ground, or perhaps parasitic components. Their mathematical expressions are shown in (2.18) -(2.19).

$$v_{CMV}(t)=\frac{v_{ag}(t)+v_{bg}(t)+v_{cg}(t)}{3} \tag{2.18}$$

$$i_{CMV}(t) = \frac{i_{ag}(t) + i_{bg}(t) + i_{cg}(t)}{3} \tag{2.19}$$

The common-mode voltage harmonics are components that are present in all phases. They are seen in phase-to-ground paths or to any common reference point through an impedance (phase-to-ground or leakage impedance). These components are not producing any energy to be transferred to the load because they are canceled through the differentiation of the phase voltages. Also, they are not seen by any sine-filter which usually acts on differential-mode components only. A common-mode component $v_{CMV}(t)$ is the one that has the same phase shift in all three phases, such as :

$$v_{CMV}(t) = V_{CMV_k} \cos(\lambda \omega_k t + \phi_k) \tag{2.20}$$

$$v_{ak}(t) = v_{bk}(t) = v_{ck}(t) \tag{2.21}$$

Where k, λ are arbitrary integers, ω_k an arbitrary frequency, ϕ_k an arbitrary phase-shift, and $v_{CMV}(t)$ is the magnitude of the common-mode harmonic component. The quantities v_{ak} , v_{bk} , and v_{ck} are the voltage of phases *a, b,* and *c,* respectively. In three-phase systems, all triplen baseband harmonics are common-mode quantities :

$$v_{ak}(t) = V_{CMV_k} \cos(k\omega_k t) \tag{2.22a}$$

$$v_{bk}(t) = V_{CMV_k} \cos(k\omega_k t - 2k\,\pi/3) \tag{2.22b}$$

$$v_{ck}(t) = V_{CMV_k} \cos(k\omega_k t + 2k\,\pi/3) \tag{2.22c}$$

$$v_{ak} = v_{bk} = v_{ck},\ \forall k = 3h,\ h \in \mathbb{N} \tag{2.22d}$$

From (1.13b), (12.14c), and (1.15c), it can be noticed that the modulation process inherently creates common-mode voltage components for the investigated VFD architectures. All carrier-band harmonics are, therefore, common-mode components and are respectively given en 2.23(a)-(c) for the investigated VFDs :

$$V_{CMV_{LV}}(t) = V_{dc} + V_{dc}\sum_{m=1}^{\infty} S_{m,0}\cos\left(m\omega_c t\right) \tag{2.23a}$$

$$V_{CMV_{NPC}}(t) = V_{dc}\sum_{m=1}^{\infty} S_{2m,0}\cos\left(2m\omega_c t\right) \tag{2.23b}$$

$$V_{CMV_{CHB}}(t) = V_{dc}\sum_{m=1}^{\infty} S_{(2m-1),0}\cos\left(\left(2m-1\right)\omega_c t\right) \tag{2.23c}$$

2.6.4 Numerical validation of VFD-induced harmonic expressions.

Selected time- and frequency domain simulation results from the two-level VFD switching models are shown in Figure 2.14, where the inverter line-to-neutral and line-to-line voltages waveforms are illustrated. Similar simulation comparison results in both time and frequency domains are shown in Figures 2.15 and 2.16 for a three-level NPC VFD and seven-level CHB VFD, respectively. The results from the simplified model (dotted red line) are superposed to the ones obtained from the complete VFD topology (straight blue line) with the entire PWM strategy and the inverter's power stages with IGBTs. In all the simulated cases, both models' generated voltage waveforms accurately match. The resulting spectra show a good fit between each VFD topology and its simplified model, where their generated harmonic components are located at similar frequencies with matching magnitudes. As the levels of output voltage increase, the output power quality is improved. The seven-level CHB VFD produces less harmonic distortion than the three-level NPC, which in turn shows fewer harmonic components than the two-level VFD at the same operating frequencies and same carrier frequencies. Therefore, the locations of VFD output voltage harmonic components are consistent with theoretical calculations.

In all the simulated cases, LN-voltages generated by each VFD produce three families of harmonics : baseband components which are proportional to the fundamental motor frequency, sideband or inter-harmonic components around the carrier frequency, and common-mode harmonics, which are triplen baseband and carrier band components. All these common-mode harmonic components are seen canceled through the differentiation of the LL-voltages generated by each VFD topology. The simplified VFD model provides high flexibility to perform VFD output power quality analysis with a wide range of operating conditions at reduced computation time. Double-Fourier voltage harmonics resulting from two-level, neutral-point-clamped three-level, and cascaded H-bridge multilevel simplified models with the fundamental frequency varying from 35 Hz to 60 Hz, with a step of 5 Hz are graphically presented in Figure 2.17.

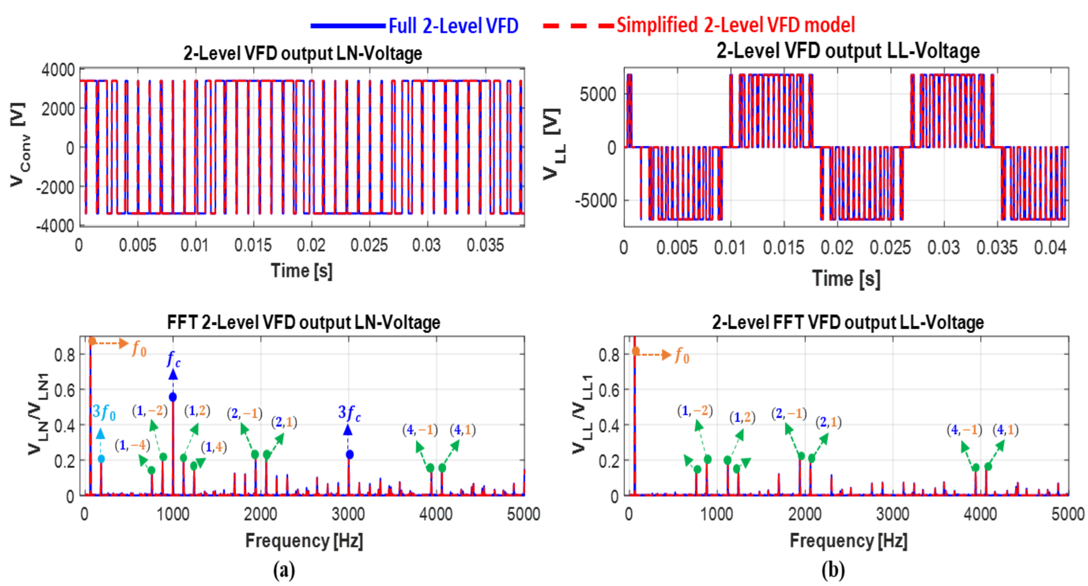

Figure 2. 14: Sample comparison simulation results between the two-level VFD and its simplified model both in time and frequency domains at *fc* = 1 kHz and *f*0 = 60 Hz. (a) Time domain. (b) Frequency domain.

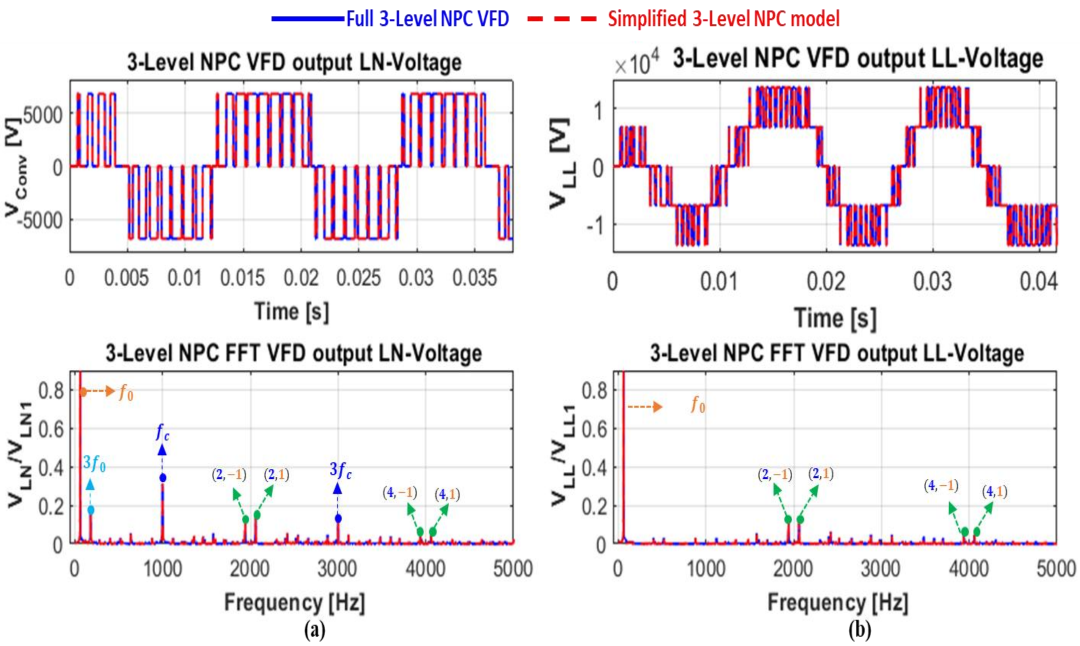

Figure 2. 15: Sample comparison simulation results between the three-level NPC VFD and its simplified model both in time and frequency domains at *fc* = 1 kHz and *f*0 = 60 Hz. (a) Time domain. (b) Frequency domain.

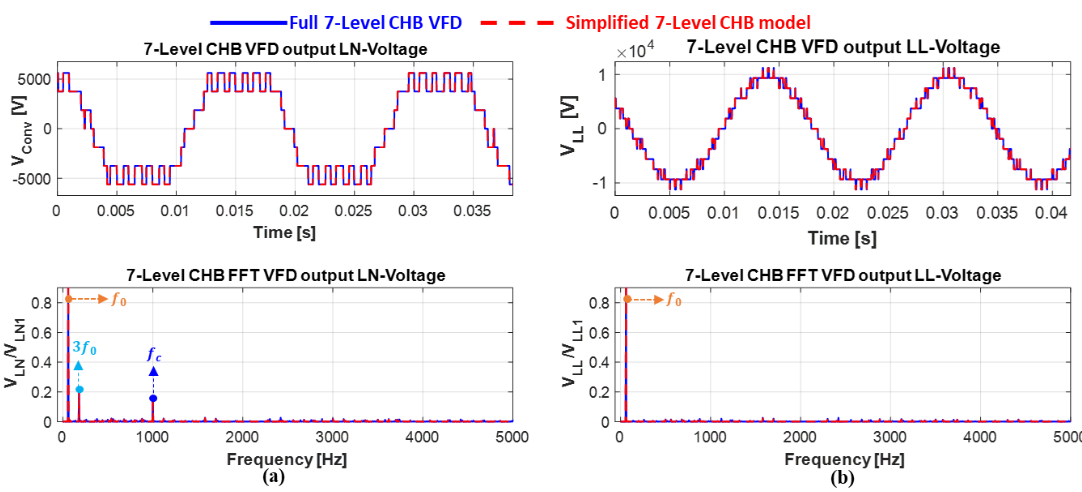

Figure 2. 16: Sample comparison simulation results between the seven-level CHB VFD and its simplified model both in time and frequency domains at *fc* = 1 kHz and *f*0 = 60 Hz. (a) Time domain. (b) Frequency domain.

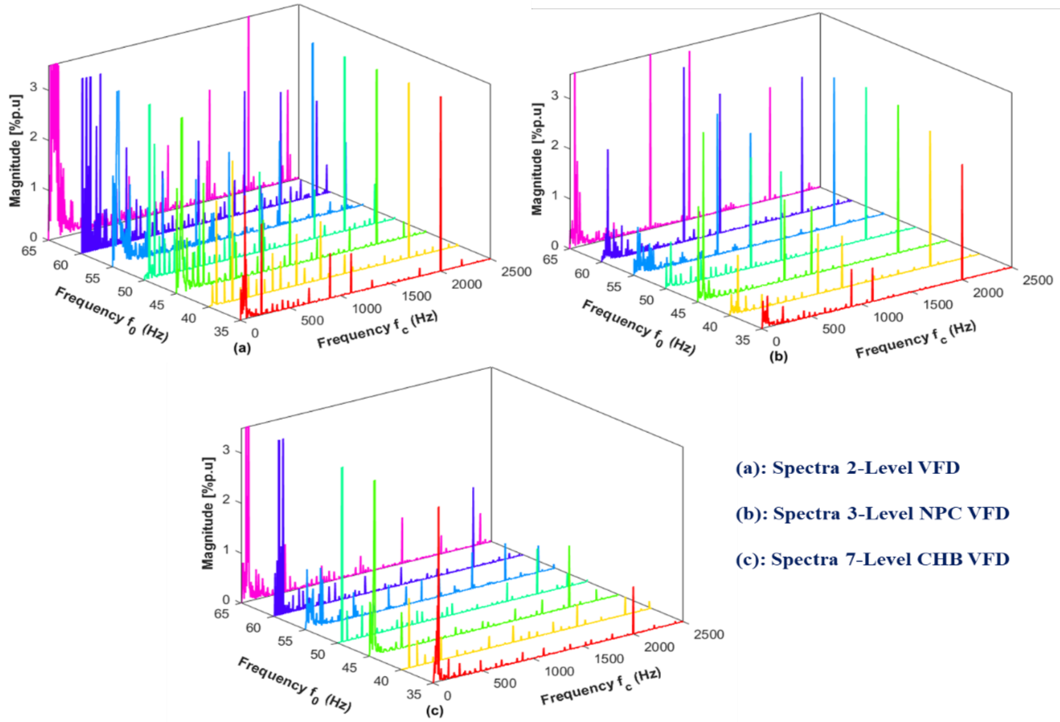

Figure 2. 17: Operational range spectra of the line-to-neutral voltage generated by (a) Two-level VFD ; (b) three-level NPC VFD, and (c) seven-level CHB VFD, with $f_c = 1\,kHz$ for all cases.

2.7 Modeling of ESP motor air-gap system

One of the most challenging engineering issues involving VFD systems is the interactions between the airgap torque they are creating and the natural frequencies of the shaft system. Voltage and current harmonics produced by the VFD topologies are mixed in the motor's air gap to generate the pulsating torque components. As a result, some of these components might have relatively high magnitudes that may induce abnormally high stress on the shaft materials. For example, suppose some oscillating torque components have frequencies at or near one of the shaft's undamped natural frequencies. In that case, the shaft's eigenmodes may be excited, potentially leading to mechanical shaft failures.

Consequently, VFDs should be designed to provide torque components with substantially low magnitude at specific frequencies to avoid the resonance excitation of the shaft. A simple time-domain model is proposed to reconstruct the electromagnetic torque dynamic in ESP motor airgap. In addition, analytical ESP motor airgap torque harmonic components, are also derived when supplied by each investigated VFD topology.

2.7.1 Electromagnetic motor air-gap torque model

For a *P*-pole motor (induction or synchronous), the electromagnetic torque in the ESP motor airgap is produced by the interaction of the motor stator flux derived from the back electromotive force (EMF) and the current produced by the VFD. The stator flux is the time integral of the stator voltage, as defined in (2.24) :

$$\psi_{abc} = \int \left(v_{abc} - Z_s i_{abc} \right) dt \tag{2.24}$$

The torque should be expressed in the stationary and orthogonal coordinates αβ [74] :

$$t_e(t) = \frac{3}{2}\frac{P}{2}\left(\psi_\alpha i_\beta - \psi_\beta i_\alpha \right) \tag{2.25}$$

where i_α and i_β are the currents in $\alpha\beta$ reference, and ψ_α and ψ_β are the stator fluxes in $\alpha\beta$ reference. Figure 2.16 shows the motor electromagnetic torque model that only depends on the quality of voltages and currents being applied to the motor terminals [75]. This model shows that the voltage drop caused by stator windings has been neglected for simplicity. It has a negligible impact on the accuracy of the results because the stator impedance does not influence the location of torque components in the frequency domain. Therefore, it may only slightly modify their respective magnitudes.

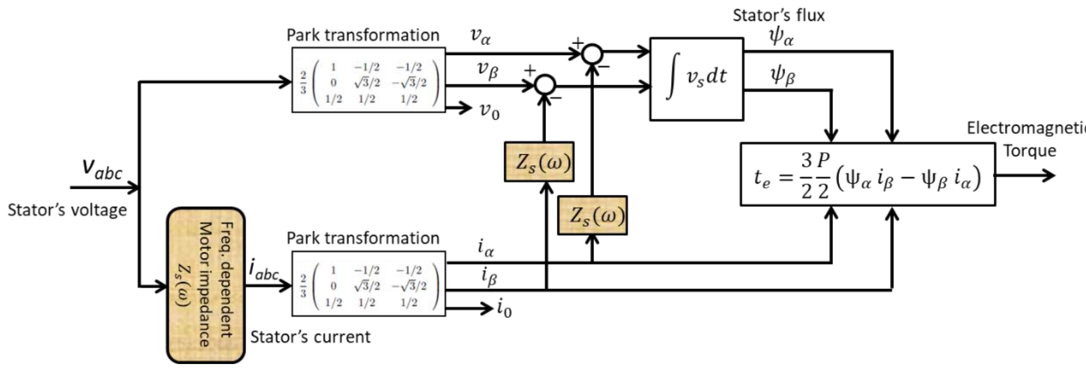

Figure 2. 18: Electromagnetic torque model of a motor.

2.7.2 VFD-induced electromagnetic torque harmonics.

Regardless of the operation mode of the ESP motor, voltage and current harmonic quantities in steady state can be written in a generic form as given by [75] :

$$v_a(t) = \sum_{m=0}^{\infty}\sum_{n=0}^{\infty} V_{m_v,n_v} \cos\left(m_v\omega_c t + n_v\omega_0 t + \theta^{v}_{m_v n_v}\right) \tag{2.26}$$

$$i_a(t) = \sum_{m=0}^{\infty}\sum_{n=0}^{\infty} I_{m_i,n_i} \cos\left(m_i\omega_c t + n_i\omega_0 t + \theta^{i}_{m_i n_i}\right) \tag{2.27}$$

Where ω_c is carrier frequency and ω_0 the fundamental frequency ; m_v, n_v and m_i, n_i are arbitrary integers ; V_{m_v,n_v} and I_{m_i,n_i} are the voltage and current magnitudes. The arbitrary integer sets (m_v, n_v) and (m_i, n_i) depend on the VFD inverter topology and its modulation strategy. Equation (2.28) is a generic motor electromagnetic instantaneous torque equation induced by any VFD with all harmonic families. It includes the DC-component, baseband, and sideband harmonic families, which might have relevant magnitudes.

$$t_e(t) = \sum_{m=0}^{\infty}\sum_{n=-\infty}^{\infty} T_{e,m,n} \cos\left(m\omega_c t + n\omega_0 t + \theta^{T_e}_{m,n}\right) \tag{2.28}$$

The following airgap torque components and their sources of electrical (voltage and current) harmonic families are found in all investigated VFDs.

Airgap torque components from electrical fundamental and baseband harmonics :

$$t_{e,Z_{0,6N}}(t) = T_{eDC} + \sum_{n=1}^{\infty} T_{e,0,6n} \cos\left(6n\omega_0 t\right) \tag{2.29}$$

Airgap torque components from sidebands around even multiple of carrier frequency of electrical harmonics

$$t_{e_{2m\pm 2n}}(t) = \sum_{m=1}^{\infty}\sum_{n=0}^{\infty} T_{e_{2m,6n}} \cos\left(2m\omega_c t \pm 6n\omega_0 t\right) \tag{2.30}$$

Airgap torque components from sidebands around odd multiple of carrier frequency of electrical harmonics

$$t_{e_{2m\pm 2n-1}}(t) = \sum_{m=1}^{\infty}\sum_{n=0}^{\infty} T_{e_{2m,2n}-1} \cos\left(2m\omega_c t \pm \left(2n-1\right) n\omega_0 t\right) \tag{2.31}$$

A summary of possible locations of the airgap torque components induced by any VFD inverter topology in the frequency domain is given in Table 2.1.

Table 2. 1 : Example of possible locations of the airgap torque components in the frequency domain.

Fundamental and baseband harmonics		
(m, n)	**Voltage/Current**	**Torque**
$(\mathbf{0}, \mathbf{1})$	ω_c	0
$(\mathbf{0}, \mathbf{5})$	$5\omega_0$	$6\omega_0$
$(\mathbf{0}, \mathbf{7})$	$7\omega_0$	
$(\mathbf{0}, \mathbf{11})$	$11\omega_0$	$12\omega_0$

$(0, 13)$	$13\omega_0$	
Carrier band and sideband harmonics around odd multiple of carrier frequency		
$(1, 0)$	ω_c	None
$(1, 2)$	$\omega_c \pm 2\omega_0$	$\omega_c \pm 3\omega_0$
$(1, 4)$	$\omega_c \pm 4\omega_0$	
$(1, 6)$	$\omega_c \pm 6\omega_0$	None
$(1, 8)$	$\omega_c \pm 8\omega_0$	$\omega_c \pm 9\omega_0$
$(1, 10)$	$\omega_c \pm 10\omega_0$	
Carrier band and sideband harmonics around even multiple of carrier frequency		
$(2, 0)$	None	None
$(2, 1)$	$2\omega_c \pm \omega_0$	$2\omega_c$
$(2, 3)$	$2\omega_c \pm 3\omega_0$	None
$(2, 5)$	$2\omega_c \pm 5\omega_0$	$2\omega_c \pm 6\omega_0$
$(2, 7)$	$2\omega_c \pm 7\omega_0$	
$(2, 9)$	$2\omega_c \pm 9\omega_0$	None
$(2, 11)$	$2\omega_c \pm 11\omega_0$	$2\omega_c \pm 12\omega_0$
$(2, 13)$	$2\omega_c \pm 13\omega_0$	

2.8 Key power quality parameters

Most of the reported ESP electrical failures have been related to poor VFD output power quality [54], [76-80]. Therefore, attention is paid to the quality of voltages and current delivered downhole to the ESP motor. The quality of power can be evaluated through a set of performance factors. By quantifying the profile of power quality supplied to the ESP motor, the user can clearly understand the impact of these factors on the quality of power supplied to the ESP motor. This section provides the theoretical foundations for assessing key power quality parameters in ESP systems supplied by VFDs. The following parameters are of particular interest :

- ✓ RMS and peak voltages and currents
- ✓ Maximum dv/dt
- ✓ Voltage and current THDs
- ✓ Common-mode voltage and current

These parameters are discussed in this chapter for pedagogical purposes only. However, the common-mode quantities are discussed in dept to analytically clarify their origins through the PWM modulation process applied to the three VFD topologies under investigation.

2.8.1 RMS and Peak Voltages and Currents

The RMS (root-mean-square) value of a quantity is the square root of the mean value of the squared value of the quantity taken over an interval. It is the measurement used for any time-varying signal's effective value. The peak value is the maximum instantaneous value of a signal as measured from zero-level.

Take a sine wave representing either voltage or current with peak y_{peak} :

$$y(t) = y_{peak} \sin\left(\omega t\right) \tag{2.32}$$

The RMS value y_{RMS} is given by :

$$y_{RMS} = \sqrt{\frac{1}{T}\int_{0}^{T} y^2(t)dt} = \sqrt{\frac{1}{T}\int_{0}^{T} A^2 \sin^2(\omega t)dt} = 0.7 * y_{peak} \tag{2.33}$$

2.8.2 Maximum dv/dt

VFD-generated voltage waveforms look like square waves. However, when zooming in on the leading edge of the voltage pulse, the pulse's rise-time of the pulse becomes apparent. The change in voltage 'dv' and the change in time 'dt' can be obtained to determine the voltage gradient, *dv/dt*. Figure 2.19 shows an example of the enlarged view of a single pulse of a VFD output waveform. The rise time (t_r), shown as *dt,* is the time required for the voltage to rise from 10% to 90% of the peak voltage. The *dv/dt* is the slope of the voltage rise in volts per microsecond (μ). The *dv/dt* can be approximated as 80% of the peak voltage divided by the rise time. High *dv/dt* due to short rise times may lead to voltage spikes at the leading edge of the voltage pulse. Voltage spikes can create ringing effects because of the cable impedance, potentially leading to higher voltage stresses on the system insulation [82].

$$dv / dt = \frac{0.8 * V_{peak}}{tr} \tag{2.34}$$

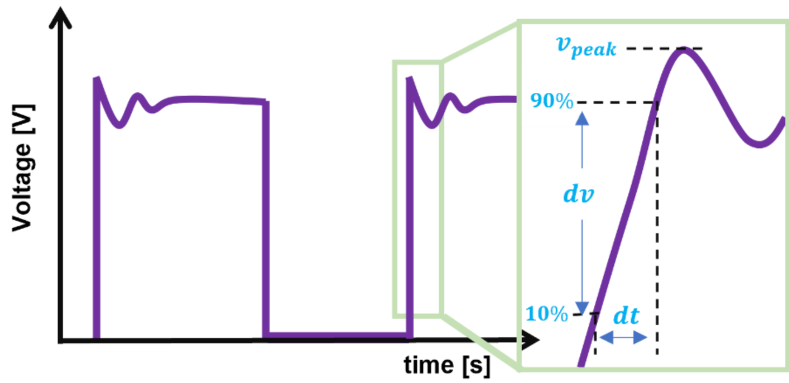

Figure 2. 19: Definition of *dv/dt*

In calculating *dv/dt* from the stated rise time, it is essential to know the definition used for its calculation. This chapter uses the definition of pulse rise time given in NEMA standard MG1 [87]. The rise time can be determined by the switching characteristics of the VFD power switches (IGBTs, MOSFETs, etc.) and associated components. Some other aspects of the VFD circuit that can influence the rise time and height of the overshoot include :

- ✓ The snubber circuit design
- ✓ The internal resistance, inductance, and capacitance of all the components
- ✓ The wiring and mechanical elements of the circuits

According to NEMA standard MG1 [88], considering various VFD brands and models, the rise time is typically $0.1\mu s$ using third generation IGBTs. The first generation of IGBTs had a rise time of about $2.5\mu s$.

2.8.3 Voltage and current THDs

THD is a measurement that indicates how much of the voltage or current distortion is due to the harmonic signal. As described in section 2.8.3, the harmonic frequencies of a periodic voltage or current are frequency components in the signal at an integer multiple of the frequency of the fundamental component (baseband components), and components that are the combination of switching and fundamental frequencies, called sidebands harmonics or inter-harmonics. THD is defined as [88] :

$$THD = 100\frac{\sqrt{\sum_{k=2}^{\infty} V_{k,RMS}^{2}}}{V_{1,RMS}} \tag{2.35}$$

Where, $V_{k,RMS}$: is the RMS voltage of the k^{th} harmonic and : is $V_{1,RMS}$ the RMS voltage of the fundamental frequency. Equation (2.35) shows the mathematical definition of THD ; the voltage is used in this equation, but current could be used instead.

2.9 MATLAB-based simulation of VFD-ESP system model

2.9.1 Implemented VFD-ESP system model.

The closed-form time and frequency domain models of VFDs developed in the previous section are crucial to understanding the location of voltage harmonics generated and analyzing their propagation along the transmission cable and motor terminals. Once the closed-form VFD models are known, the VFD power stage configurations, including IGBTs, are not needed anymore for the overall ESP system simulation and analysis. Because ESP power quality is governed by the quality of the voltage generated by the VFD and the current flowing through the system, the behavior of the voltage and current applied at the motor terminal is analyzed in this section. This section also investigates the electromagnetic torque resultant from the imperfection of the power quality supplied to the ESP motor.

The integrated equivalent simplified model of the overall ESP system is shown in Figure 2.20. As can be seen in this figure, the VFD behavior is represented as a per-phase PWM switching function. This function is in per unit with respect to the total DC-link voltage. Next, the VFD-switched waveform is applied to the cable sending-end. The cable model is shown as a multiple pi-section, and the mechanical load is also shown as a multi-inertia system through the electromechanical analogy. Finally, the airgap torque model is inserted between the two subsystems. The proposed model is generally valid for all topology candidates in the oil and gas industries, specifically for all ESP systems. In addition, it is suitable for power quality analysis, including torsional analysis.

The simplified model is built and simulated in MATLAB/Simulink. The motor input voltage and current, and torque waveforms are recorded for post-process analyses in the time domain. A fast Fourier Transform is applied to the recorded time-domain. Results, and harmonic locations in the frequency domain have been extracted and compared to the predicted theoretical harmonics for validation purposes.

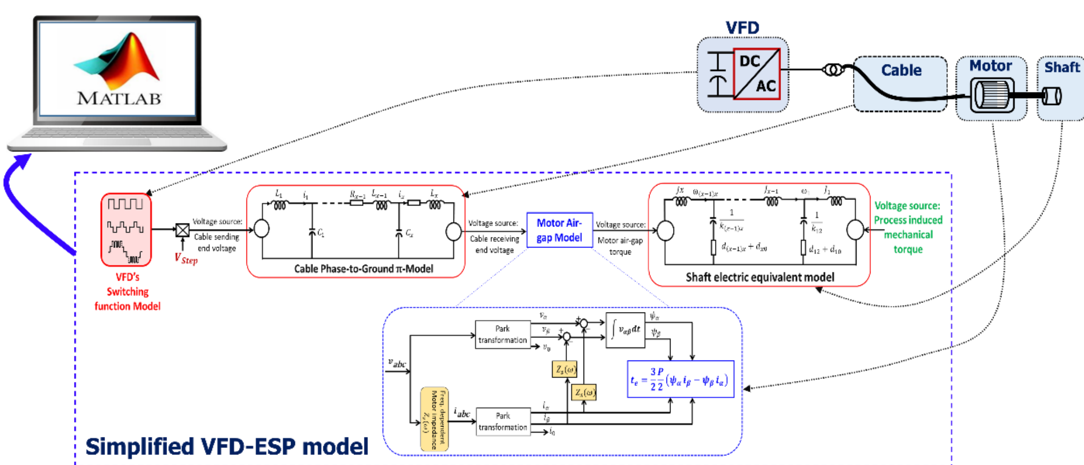

Figure 2. 20: Integration of subsystem models for numerical validation purposes

Key power quality characteristics are also measured for further analysis at each simulation operating point. System parameters used for simulated are shown in Appendix A, Table 2.1.

2.9.2 Offline simulation results and discussions

More than 1000 operating points have been simulated. The detailed results of specific cases, where $f_c = 1kHz$ and $f_c = 60Hz$ are discussed for the three investigated VFD-ESP systems. Sample simulation results for the ESP system with a low-voltage 2-level VFD model are depicted in Figure 2.21. Similar results for three-level NPC and seven-level CHB ESP systems are shown in Figures 2.22 and 2.23, respectively. Each simulated ESP system model shows time and frequency domain results for each state variable. Simulation results obtained from the model in all investigated systems are consistent with theoretical predictions. Motor input voltage harmonics are at identical frequencies to VFD-generated harmonics. As expected, the common-mode voltage (triplen baseband and carrier band) harmonics with a significantly high magnitude in the motor LN-voltages are canceled in the motor LL-voltage. There are no other harmonics in the frequency range of motor LL-voltages. Only the sideband harmonics are present. The impedance of the line cable impacts the sideband harmonics' amplitudes in the motor current, which are already present in the motor voltage.

Families of torque harmonic frequencies match those of the current harmonics that have created them. Sideband current harmonics around an odd multiple of the carrier frequency $\omega_c \pm 2\omega_0$ produces torque harmonics at $\omega_c \pm 3\omega_0$. Also, sideband current harmonics around an even multiple of the carrier frequency $2\omega_c \pm \omega_0$ create torque harmonics at $2\omega_c$. A detailed analysis of the motor current and torque harmonic families for a two-level VFD-ESP system [Figures 2.24(c2) and 2.24(d2)] is provided below for illustrative purposes :

- ✓ Sideband current harmonics around f_c the PWM frequency are :

  $880 = |1000 - 2 \times 60|\,\text{Hz}$; $1120 = |1000 + 2 \times 60|\,\text{Hz}$;

- ✓ Resulting sideband torque harmonics around f_c the PWM frequency:

  $820 = |1000 - 3 \times 60|\,\text{Hz}$; $1180 = |1000 + 3 \times 60|\,\text{Hz}$;

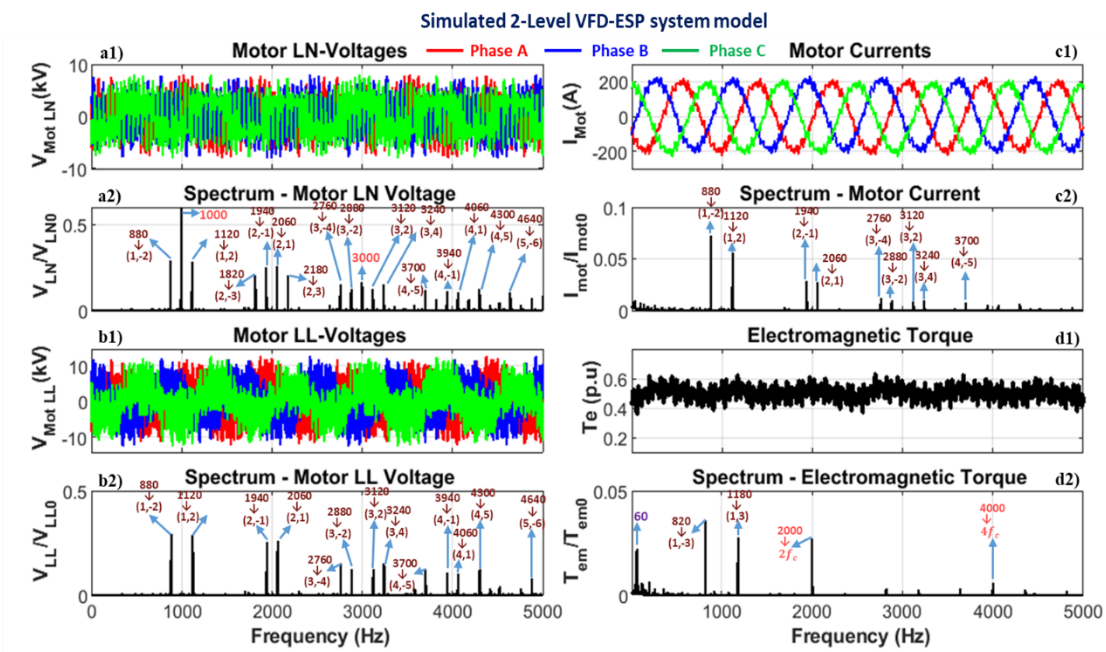

Figure 2. 21: Simulation results of two-level VFD ESP system model with $f_c = 1kHz$; $f_0 = 60Hz$: (a1) motor LN-voltages, (a2) spectrum of motor LN-voltage, (b1) motor LL-voltages, (b2) spectrum of motor LN-voltage, (c1) motor currents, (c2) spectrum of motor current, (d1) motor electromagnetic torque, (d2) spectrum of motor electromagnetic.

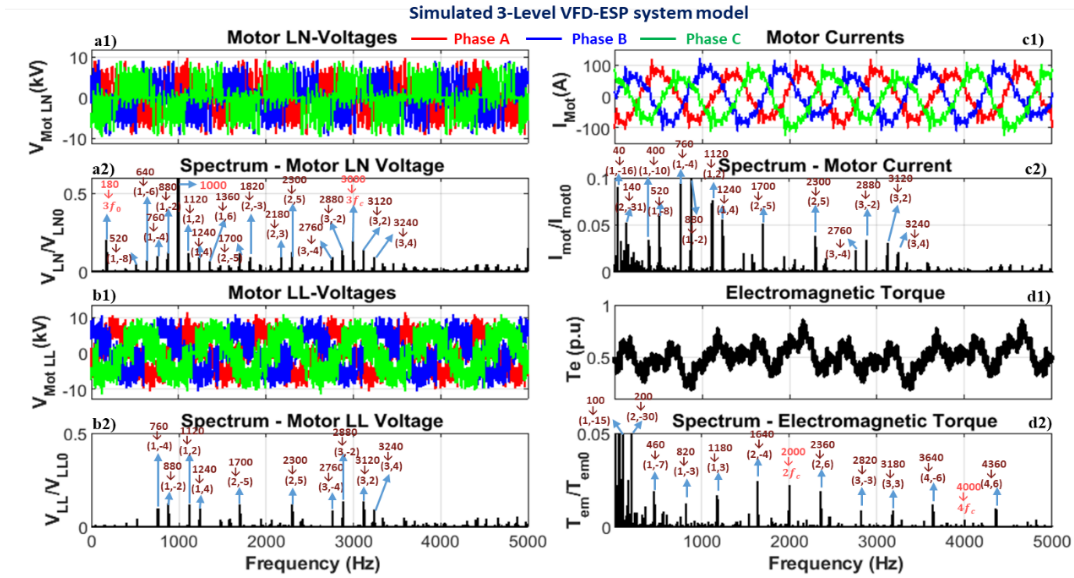

Figure 2. 22: Simulation results of three-level NPC VFD ESP system model with $f_c = 1kHz$; $f_0 = 60Hz$: (a1) motor LN-voltages, (a2) spectrum of motor LN-voltage, (b1) motor LL-voltages, (b2) spectrum of motor LN-voltage, (c1) motor currents, (c2) spectrum of motor current, (d1) motor electromagnetic torque, (d2) spectrum of motor electromagnetic.

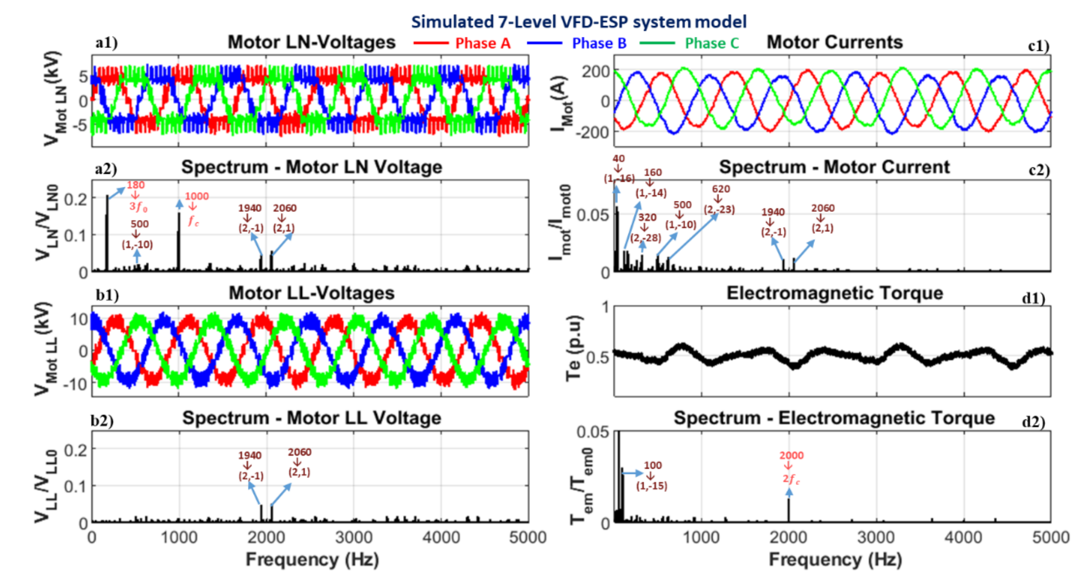

Figure 2. 23: Simulation results of seven-level CHB VFD ESP system model with ith $f_c = 1kHz$; $f_0 = 60Hz$: (a1) motor LN-voltages, (a2) spectrum of motor LN-voltage, (b1) motor LL-voltages, (b2) spectrum of motor LN-voltage, (c1) motor currents, (c2) spectrum of motor current, (d1) motor electromagnetic torque, (d2) spectrum of motor electromagnetic.

✓ Sideband current harmonics around $2 \cdot f_c$ the PWM frequency are :

$$1940 = |2 \times 1000 - 1 \times 60| \text{ Hz} \;;\; 2060 = |2 \times 1000 + 1 \times 60| \text{ Hz} \;;$$

For further power quality study, the key PQ parameters stated in section 4 were computed from a MATLAB code and then plotted as a table. The 2-level, 3-level, and 7-level VFD-ESP system models' measured PQ parameters obtained when $f_0 = 60Hz$ are shown in Figures 2.24(a), (b), and (c), respectively. It can be observed that the measured RMS voltages and currents and Peak voltages in each case are close to their rated values. The 2-level system model, as predicted, presents high THD of voltage and current than the 3-level NPC system model, which exhibits higher THDs than the 7-level CHB system model.

PQ Parameters from Two-Level VFD-ESP system model

	Voltages	Currents
RMS PhA	4140.1	137.94
RMS PhB	4165.5	140.27
RMS PhC	4141.8	137.67
Peak PhA	5854.9	NaN
Peak PhB	5890.9	NaN
Peak PhC	5857.4	NaN
THD PhA	35.86	3.8834
THD PhB	35.532	3.8801
THD PhC	35.705	3.8834
Imbalance values	0.42138	4.449

(a)

PQ Parameters from 3-Level NPC VFD-ESP system model

	Voltages	Currents
RMS PhA	3985.8	141.86
RMS PhB	3967.8	142.91
RMS PhC	3972.2	142.09
Peak PhA	5636.8	NaN
Peak PhB	5611.3	NaN
Peak PhC	5617.5	NaN
THD PhA	27.158	3.724
THD PhB	27.535	3.609
THD PhC	27.207	3.724
Imbalance values	2.2618	3.5017

(b)

PQ Parameters from 7-Level CHB VFD-ESP system model

	Voltages	Currents
RMS PhA	4036.4	130.61
RMS PhB	4033.8	131.62
RMS PhC	4037.9	131.3
Peak PhA	5708.4	NaN
Peak PhB	5704.6	NaN
Peak PhC	5710.4	NaN
THD PhA	22.938	2.4899
THD PhB	22.463	2.1696
THD PhC	22.507	2.4899
Imbalance values	0.61799	6.9439

(c)

Figure 2. 24: Measured PQ parameters obtained from each simulated ESP system model at $f_c = 1kHz$; $f_0 = 50Hz$: (a) Two-level VFD-ESP model, (b) Three-level NPC VFD-ESP model, (c) Seven-level CHB VFD-ESP model.

2.10 Hybrid experimental-numerical validations

2.10.1 Hybrid real-time validation procedure

The robustness of the proposed model (Figure 2.25) is evaluated through hybrid real-time simulations. In this validation, the proposed model is divided into (real/analogical) and numerical/digital parts, coupled together and executed in real-time. The idea is to assess the proposed model's suitability for operational testing using inverter field measurement. The VFD switching function model is replaced in the hybrid real-time simulation with the measured voltage collected from the actual VFD power topology illustrated in Figure 2.25. The inverter measured voltages were collected from a downscale lab prototype equipped with a 3-level neutral-point-clamped (NPC) VFD inverter based on the Semikron full power module FS3L3R07W2h3f_B11. The prototype also features a set of nine power modules (each H-bridge module is based on a Semikron SK10GD12T4ET package) connected in series to create a 7-level cascaded H-bridge inverter system.

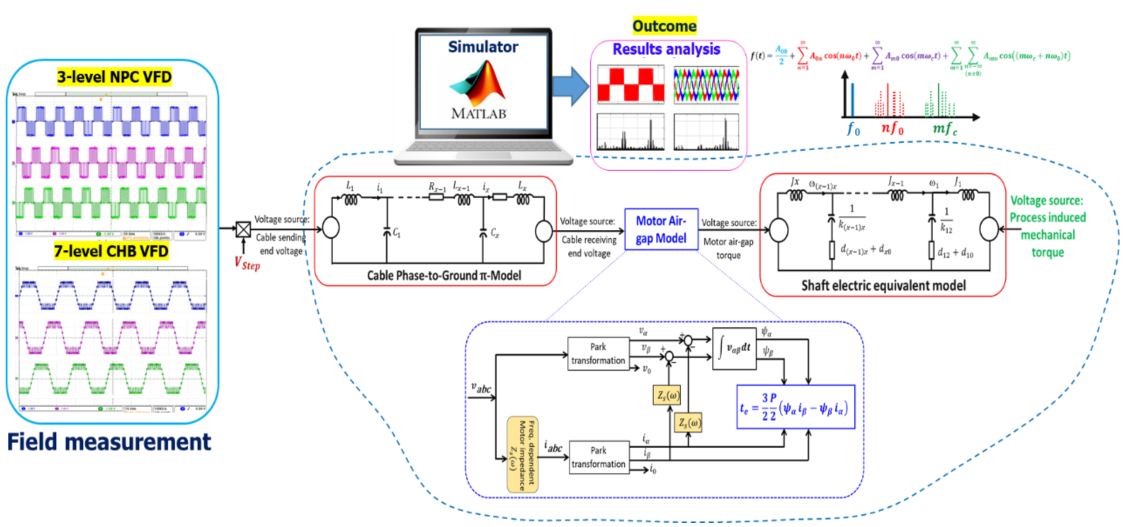

Figure 2. 25: Validation principle of Hybrid real-time simulation results

The control hardware is based on Simulink real-time Windows target equipped with a data acquisition board NI-PCI 6229. The measured three-phase inverter output voltages are acquired to the Simulink environment through analog-to-digital (ADC) converter blocks. The following two field scenarios are considered and discussed:

- ✓ NPC VFD power topology operating at the carrier frequency $f_c = 1000Hz$ and fundamental frequency $f_0 = 50Hz$
- ✓ CHB VFD power topology operating at the carrier frequency $f_c = 1500Hz$ and fundamental frequency $f_0 = 50Hz$.

At a given operating point, hybrid real-time simulations are run, then the voltages, currents, and air-gap electromagnetic torque waveforms are recorded at 50 μs sampling rate for the time and frequency domain analyses. Frequency domain results are obtained by applying a Fast Fourier Transformation with a 1 Hz resolution and an even window length to the recorded time-domain results.

2.10.2 Sample hybrid real-time simulation results and discussions

Figures. 2.26 and 2.27 show selected hybrid simulation results for the 3-level NPC and 7-level CHB VFD-ESP system models. Each ESP system model is simulated with a short electric cable (20ft) for worst-case harmonic impact at the motor voltage, current and electromagnetic waveforms. The frequencies of each harmonic component in each harmonic family are highlighted, and their magnitudes are magnified to illustrate the precise location of each relevant harmonic component. The impacts of the non-ideal inverter voltage characteristics caused by the ripples in the DC bus voltage are depicted

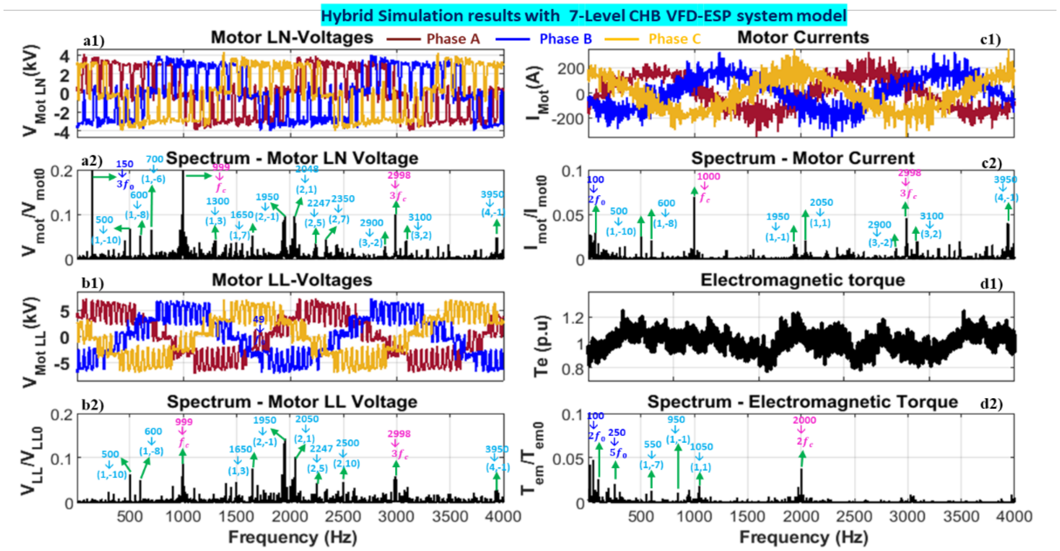

Figure 2. 26: Hybrid simulation results of three-level NPC VFD ESP system model with $f_c = 1.5kHz$ **;** $f_0 = 50Hz$ **: (a1) motor LN-voltages, (a2) spectrum of motor LN-voltage, (b1) motor LL-voltages, (b2) spectrum of motor LN-voltage, (c1) motor currents, (c2) spectrum of motor current, (d1) motor electromagnetic torque, (d2) spectrum of motor electromagnetic.**

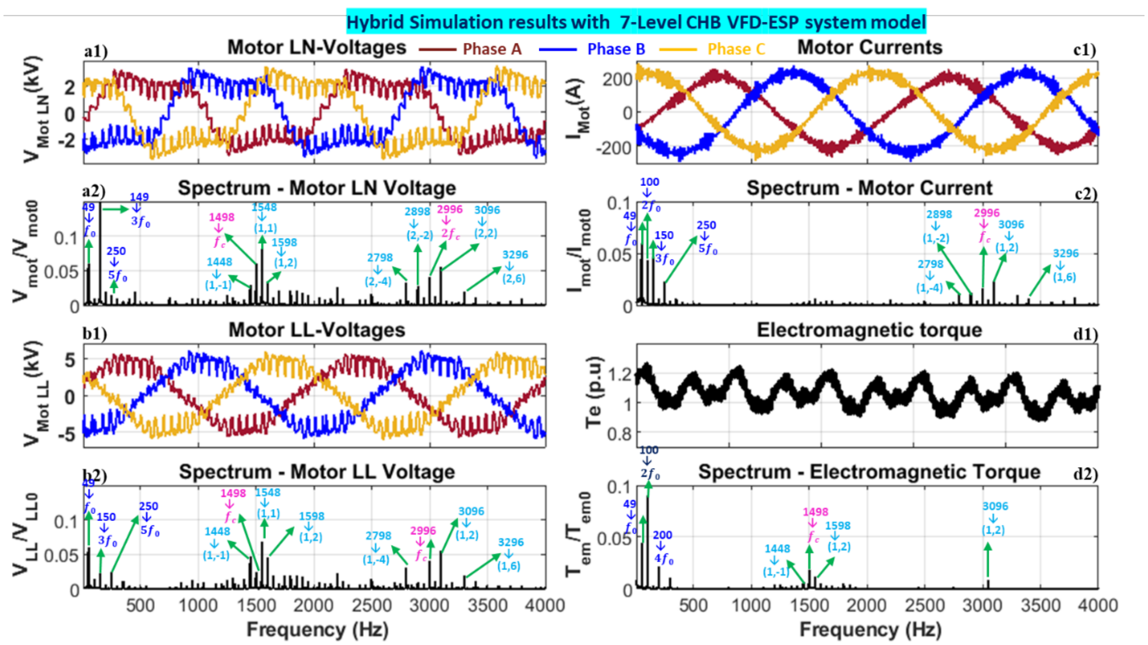

Figure 2. 27: Hybrid simulation results of seven-level CHB VFD ESP system model with $f_c = 1.5kHz$ **;** $f_0 = 50Hz$ **(a1) motor LN-voltages, (a2) spectrum of motor LN-voltage, (b1) motor LL-voltages, (b2) spectrum of motor LN-voltage, (c1) motor currents, (c2) spectrum of motor current, (d1) motor electromagnetic torque, (d2) spectrum of motor electromagnetic.**

in Figures 2.26(a1) and 2.27(a1). Figures 2.26(b2) and 2.26(b2) show the impact of the odd/even harmonic in the DC bus voltage on the harmonic distribution of the motor LN-voltages. For instance, by analyzing the results from the 7-level CHB VFD-ESP system model in Figure 2.27(b1), the odd sideband harmonic components in the first carrier group f_c and the even sideband harmonic components in the second carrier group are given as follows :

- ✓ Odd sideband voltage harmonics around $1\times$ the PWM frequency f_c (1500 Hz) are : $1448 \approx |1\times1500-1\times50|$ Hz ; $1548 \approx |1\times1500+1\times50|$ Hz ;

Similar harmonics analyses are performed for the results of the hybrid simulation of the 3-level NPC system model in Figure 2.26(b1). In both cases, the locations of relevant harmonics in motor current are consistent with those in motor voltages. Only their magnitudes are adjusted due to the cable impedance effects. The first and second carrier groups present the even and odd-order sideband current harmonics. Voltage common-mode components (triplen baseband and carrier band harmonics) are canceled through the differentiation of the line-to-line voltages, but their magnitudes have been significantly reduced. Therefore, the families of electromagnetic torque harmonics produced by each VF-ESP system model are not provided based on the analytical expression of the frequencies derived in Subsection 3.3.3, where the inverter is assumed to operate with a pure DC component in the DC-bus voltage. In ideal conditions, each electromagnetic harmonic is created by two current harmonic components. However, from Figures 2.26(d2) and 2.27(d2), new harmonic components are present in the electromagnetic torque spectrum due to the interaction between the DC bus voltage harmonics and the inverter PWM voltage harmonics. Overall, hybrid simulation results are also crucial to carefully evaluate how harmonics from inverter field voltage measurements propagate through the transmission cable so that their effects on the quality of the power being supplied to the ESP motor can be assessed prior to installation of the entire system.

2.11 Conclusion article 1

This chapter proposes a unified approach to understanding how variable frequency drives impact the power quality of an Electric Submersible Pump supplied through a transmission cable. It also explains how VFDs might excite mechanical-shaft torsional modes in such applications. The chapter outlines easy-to-follow procedures for system integration analyses of such configurations, including torsion vibration analysis. Time-domain and frequency-domain switching function models of two-level, three-level neutral-point-clamped, and cascaded H-bridge multilevel VFD inverter topologies are proposed for this purpose. Simulating VFD-ESP systems is time-consuming and requires complex skill sets to design, model, and implement in simulation software. Therefore, a simplified time-domain model is proposed to reproduce the steady-state behavior of low- and medium-voltage ESP systems supplied by PWM-VFD topologies at various operating points in normal and failure modes. The investigated failure mode in this research is when an ESP system is powered by a CHB-VFD topology operating with one or more damaged and bypassed power modules. Under a failure mode, the neutral-shift PWM technique is applied by modifying the PWM reference voltage angles. The neutral-shift strategy produces balanced inverter output line voltages and currents even if its phase voltages are unbalanced due to the failed cells. Offline and hybrid real-time simulation results at different operating points support the accuracy of the proposed simplified VFD-ESP system model. Results are generated in time and frequency domains, as well as main power quality parameters, such as RMS and Peak voltages, voltage and current THDs, maximum dv/dt, voltage, and current imbalances. In all simulated cases studied, voltage, current, and motor air-gap torque harmonic components induced by the three investigated VFD topologies are derived and correlated to the theoretical predictions. In addition, the effects of the electrical and mechanical spectrum modification using a neutral-shift control strategy under failed cells are highlighted and discussed. Overall, simulation results match the theoretical calculation with acceptable accuracy, regardless of the selected operating points or carrier frequencies.

CHAPTER 3 : GRAPHICAL ANALYSIS AND CONTROL OF CASCADED H-BRIDGE MULTILEVEL INVERTER USING CLARKE TRANSFORMATION WITH NEUTRAL-SHIFT STRATEGY UNDER NON-IDEAL CONDITIONS

3.1 Introduction article 2

The cascaded H-bridge multilevel converter topology is the ultimate solution for energy conversion in various industrial applications due to its exceptional features, such as high modularity and fault-tolerant capability. However, two circumstances can lead to unbalanced operation of the inverter, potentially causing a decrease in its reliability and survivability : unequal DC voltage sources or faulty cells. In the past decades, scientists and engineers have conducted intensive research and meaningful studies to propose control solutions capables of maintaining the stable and continuous operation of the inverter under these operational concerns. Typically, each of these challenges is addressed separately using a distinct compensation control scheme in the existing literature. This chapter surveys the existing and most popular compensation control schemes suitable for CHBMI operation under unequal DC-voltage sources and failed cells, focusing on those that modified the inverter modulation stage. The theoretical foundations of each control scheme are presented and discussed, including their operating principle and implementation procedure, advantages, and disadvantages.

In the last decades, the cascaded H-bridge multilevel inverter topology has become a solution for energy conversion in different industries [1], [2]. Its advantages, such as high efficiency, low harmonic distortion, modularity, and scalability, make it one of a promising technological power conversion in various high-power applications like renewable energy systems, electric vehicles, motor drives, and grid-connected systems [3-6], as illustrated in Fig. 1. Each H-bridge cell in a CHB inverter typically has its own isolated DC source (e.g., batteries, solar panels, supper-capacitor, or wind). However, the main challenge when using a three-phase CHB inverter is that it may exhibit unbalanced operation due to non-ideal conditions. The non-ideal conditions primarily refer to the scenario of unequal DC voltage inputs, where the connected DC sources exhibit different voltage levels across the H-bridge cells, leading to inverter output voltage waveforms.

In grid-connected photovoltaic (PV) inverter applications, the non-ideal condition results from inconsistent power generation among the power modules due to varying environmental factors, such as fluctuating solar irradiance, partial shading, temperature inhomogeneity, and inconsistent degradation of some solar cells [7], [8]. In Electric vehicle (EV) and hybrid EV traction systems, battery degradation or unequal charging can cause imbalances in the DC-link voltage across H-bridge cells [9], [10], leading to unbalanced motor drive operation. Voltage imbalance at motor terminals can cause a current imbalance up to 6-10 times larger, leading to issues such as torque pulsation, vibrations, mechanical stress, lower efficiency, and motor overheating [11], [12].

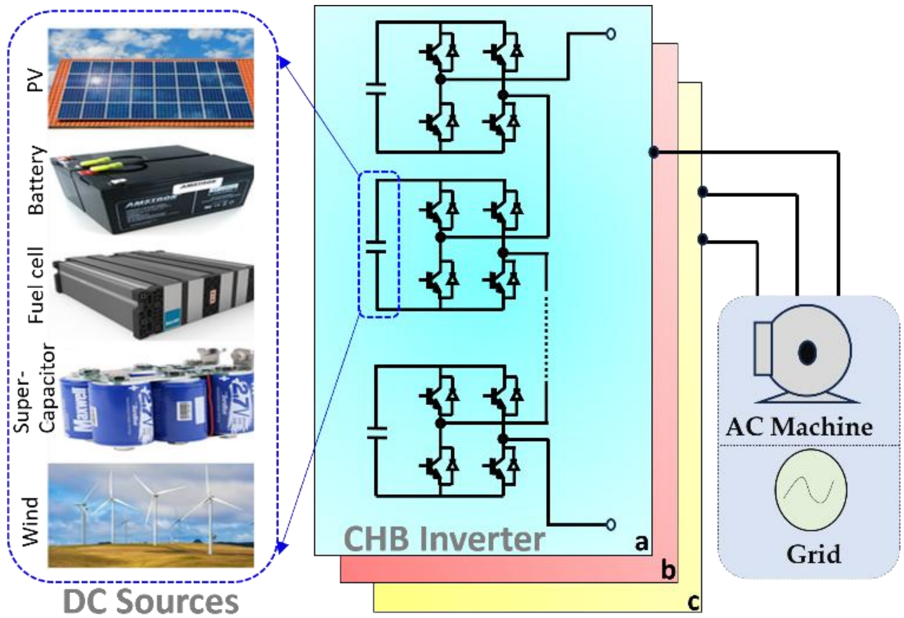

Figure 3. 1: The CHB inverter topology and its applications

Non-ideal conditions also occur when power electronic switches or associated gate driver boards in the power stage fail, leading to failure and bypass of H-bridge cells [13], [14]. When the H-bridge cell fails and is bypassed, it cannot contribute to the inverter output voltage, resulting in an unbalanced system operation.

Numerous studies have been conducted to develop effective control and modulation techniques suitable for CHB under non-ideal conditions (unequal DC source voltages and failed cells). Table 1 summarizes the most popular existing control strategies, highlighting their advantages and drawbacks. In [15], a neutral voltage modulation (NVM) strategy was proposed to address DC-link voltage inequality in CHBs. The conventional NVM method uses simple calculations to find the neutral voltage reference, incorporating zero-sequence voltage to compensate for output voltage imbalances and an offset voltage to extend the linear modulation range. However, the constraints on the neutral voltage are unclear, and in some cases, the maximum linear modulation index cannot be reached [16]. To address these limitations, an improved NVM method was introduced in [17], aimed at achieving a balanced three-phase output voltage in CHB inverters, even in the maximum modulation region, while minimizing overmodulation [18].

Zero-sequence voltage injection (ZSI) methods have proven effective for power control purposes under unequal DC voltage distribution conditions [8], [19], [20]. They maintain balanced three-phase currents under non-ideal conditions. However, the optimal zero-sequence injection method is considered the most advanced ZSI method, and it can only handle up to 20% of potential cell DC voltage inequality.

Table 3. 1 : Advantages and disadvantages of existing control scheme for CHB inverter under non-ideal conditions

CHB inverter with unequal DC-voltage sources	
Neutral Voltage Modulation (NVM) methods [15], [17], [18]	✓ Line-to-line voltage balancing capability. ✓ Simple implementation
	x Unsuitable for power balancing x Unsuitable under failed cell conditions
Zero-sequence Injection (ZSI) methods [8], [19], [20]	✓ Power balancing capability. ✓ Capable to operate in overmodulation Range
	x Unsuitable for line-to-line voltage balancing x Complex implementation ✓ Unsuitable under failed cell conditions
CHB inverter with failed cells	
Conventional Neutral-shift method [24]	✓ Line-to-line voltage balancing capability. ✓ Maxime the output voltage under faulty cells
	x Unsuitable under non-integer or dynamically changing DC voltage values x Unsuitable under severe failed cell conditions
Peak-reduction method [25]	✓ Line-to-line voltage balancing capability. ✓ Suitable under severe faulty cell conditions
	x Unsuitable under non-integer or dynamically changing DC voltage values

	x May cause overmodulation.

Several other studies have also proposed fault-tolerant control strategies for CHB inverter operation with faulty cells [21], [22]. These strategies can maintain balanced inverter output line voltages despite unbalanced phase voltages caused by failed cells [23], [24]. The two most commonly used techniques are the conventional neutral-shift and peak-reduction methods. Under the traditional neutral-shift methods, the inverter's neutral point is moved by adjusting the reference phase voltage angles [25]. In peak-reduction techniques, the neutral point is moved by adjusting the reference phase voltage magnitudes [26].

According to Table. 3.1, each investigated non-ideal condition has been addressed separately in the literature, utilizing an independent compensation control strategy. NVM and ZSI methods were developed for CHB systems under unequal DC voltage conditions and are inefficient for CHB systems with failed cells. Conversely, the conventional neutral-shift and peak-reduction methods are unsuitable for CHB inverters with DC voltage inequality, especially under non-integer or dynamically changing DC voltage levels. There is a gap in the literature regarding analysis and control methods that simultaneously address unequal DC voltage sources and failed cells in CHB topologies.

This study proposes a unified approach utilizing graphical analysis to address the challenges posed by unequal DC voltage distribution and failed cells in CHB systems without differentiation. The proposed graphical analysis examines the unbalanced operation of the CHB inverter caused by non-integer DC voltage inputs, leading to a space vector diagram with non-integer entries. This novel graphical approach introduces a generalized control strategy based on the neutral-shift technique, which mitigates the effects of unequal DC voltage sources while simultaneously addressing cell failures. The proposed study applies to CHB-based power conversion inverter systems with DC source topologies, such as batteries, solar panels, supercapacitors, or wind energy systems, where maintaining equal DC voltage inputs is seldom feasible. Additionally, this method enhances the system's robustness and reliability, particularly in high-power variable frequency drive applications with multiple series-connected power cells, where some may fail and require bypassing.

3.2 A Space Vector Analysis of CHB Operation under Ideal Conditions

3.2.1 Analysis of inverter voltage states under ideal conditions

Let's assume the CHB topology (Fig. 1) that uses a k-series connected single-phase inverters (power cells), each supplied by an isolated DC voltage source noted $v_{dc,ij}$, where $i \in \mathbb{P} = \{a, b, c\}, j \in \mathbb{L} = \{1,2, \dots, k\}$, Under ideal operating conditions of the inverter, it is assumed that all DC voltage sources have equal values on all phase, $V_{dc,ij} = 1 \text{ p.u}$, such that:

- The output voltage of each H-bridge cell j on a given phase i is : $u_{ij} \in \mathbb{K} = \{-1, 0, 1\} \text{ p.u}$
- The number of voltage levels per phase is: $n = 2k + 1, n \in \mathbb{N}^*$ (an integer)
- The phase leg voltage amplitude is: $v_i = \sum_{j=1}^{k} u_{ij}, V_i \in \mathbb{N}^*$

Under these conditions, the three-phase CHB inverter produces a set of balanced three-phase line-to-neutral voltages It is a common accepted practice to convert the three-phase quantities of the inverter into its space-vector diagram to enable a more intuitive representation of the voltage states, making designing and optimizing its performance easier [27]. The analysis of the inverter output voltage phasor is performed in the stationary and orthogonal reference frame $\alpha\beta 0$ using the Clarke transformation as given in Eq (1).

- $v_i = [v_a\ v_b\ v_c]^T; v_{\alpha\beta 0} = \left[v_\alpha\ v_\beta\ v_0\right]^T$ (1a)

$$v_{\alpha\beta 0} = M * v_i \quad (1b)$$

$$M = \sqrt{\frac{2}{3}}\begin{bmatrix} 1 & -1/2 & -1/2 \\ 0 & \sqrt{3}/2 & -\sqrt{3}/2 \\ 1/\sqrt{2} & 1/\sqrt{2} & 1/\sqrt{2} \end{bmatrix} \quad (1c)$$

Where, v_{abc} represents the line-to-neutral (LN) output voltage in abc the reference frame, while $v_{\alpha\beta 0}$ is the LN-voltage given the stationary orthogonal (complex) reference frame $\alpha\beta$.

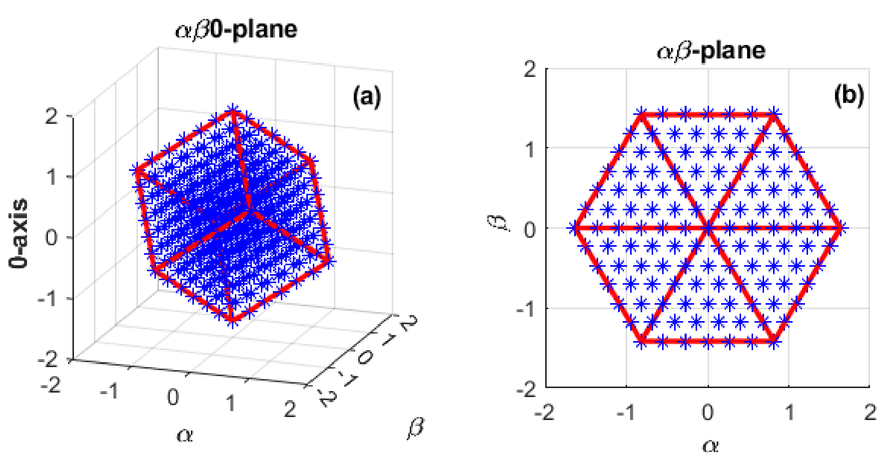

Figure 3. 2: Space vector representation of a balanced 7-level inverter output voltage states. 3D view and its projection in the $\alpha\beta -$ plane.

For a balanced operation of a n-level inverter, the total number of output voltage states is given by n^3, which forms a cube surface in the $\alpha\beta0$-space. In the case of two-level inverters, there is only $2^3 = 8$ output voltage states exist, which correspond to the eight corners of the basic cube. The balanced operation of CHB multilevel inverter introduces additional intermediate states that are typically uniformly distributed between the limits of the basic cube. When applying the transformation described in Eq (1b) to a 7-level inverter with $k = 3,$ the total number of inverter states is $7^3 = 343$, resulting in a regular cube surface as shown in Fig. 2(a). Fig. 2(b) illustrates the well-known space-vector hexagon associated with the 7-level inverter operation [27]. The solid lines in each sub-figure represent the theoretical limit of the inverter output voltage that can be produced under ideal operating conditions.

3.2.2 Analysis of CHB reference voltages under ideal conditions

In balanced operation, the PWM reference voltage signals can be expressed as:

$$v_i^{N*}(t) = m \cdot V_{\mathrm{dc}}\, sin\big(\omega_0 t - \theta_{o,i}\big) \qquad (2)$$

with $\theta_{o,i} = (i-1)\frac{2\pi}{3}$ and $i \in \mathbb{K} = \{a = 1, b = 2, c = 3\}$

Where ω_0, m, and V_{dc} are the fundamental frequency, the modulation index, and the total inverter phase leg voltage, respectively. $\boldsymbol{N}$: represents the normal (balanced) operation under ideal conditions, specifically when the three-phase inverter has equal DC voltage sources with the same magnitude. A common-mode voltage is usually added to the PWM reference voltages to improve the utilization of the DC-source voltage. The modified PWM reference with the common-mode component injection is given by:

$$v_{0i}^{N*}(t) = v_i^{N*}(t) + v_0^*(t) \qquad (3)$$

The injected common-mode voltage $v_0^*(t)$ can be the min-max voltage component (4) or the third harmonic component (5) where, V_0.is the magnitude of the fundament component of the LN voltage reference.

$$v_{0\mathrm{MM}}^*(t) = \frac{\min_{i \in \boldsymbol{P}} v_{r,i}^*(t) + \max_{i \in \boldsymbol{P}} v_{r,i}^*(t)}{2} \qquad (4)$$

$$v_{0THI}^*(t) = \frac{V_0}{6} \sin\ (\omega_0 t) \qquad (5)$$

The inverter PWM reference signal v_i^* is also Clarke transformed to $\alpha\beta 0$ reference frame as given in (6).

$$v_{i,\alpha\beta 0}^{N*} = M * [v_a^*\ v_b^*, v_0^*]^T \qquad (6)$$

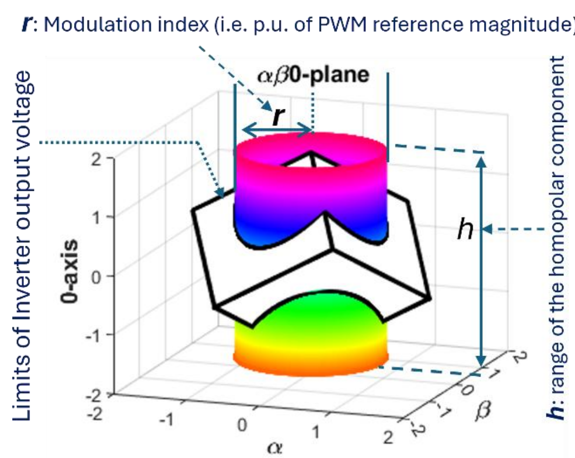

Figure 3. 3: Reference voltage cylinder and inverter output voltage cube surfaces.

The space vector representation of the PWM voltage reference vector in $\alpha\beta 0$-space when applied Eq (6) is shown in Fig. 3. This figure illustrates the coupled effects between inverter output voltage states and its PWM reference voltages. As shown in Fig. 3, the PWM reference voltage vector forms a cylindric shape in the $\alpha\beta 0$-space. Because the homopolar component moves along the *0*-axis, the family of all possible common-mode values corresponds to the cylinder height, which is centered and imbricated to the inverter voltage state cube surface. The inverter output-voltage cube is superposed to the reference-voltage cylinder within a maximum limit of $h \in [-\sqrt{3}, \sqrt{3}]$. The radius of the cylinder corresponds to the PWM modulation index.

For a balanced operation of the inverter, the PWM reference voltage must be maintained in its linear region. Subsequently, the reference-voltage cylinder surface should not exceed the limits of the inverter voltage cube surface as illustrated in Fig. 4(a). The edges of the intersected cylinder surface correspond to minimum (h_{min}) and maximum (h_{max}) values to be attained by all possible homopolar voltage components that can be added for an operation in the inverter linear region. The limits of the cylinder height under inverter linear region can be determined as follows :

$$h' = 2\sqrt{3} - \sqrt{2}\left(\max v_{r,i}^{\mathrm{N}*}(t) - \min v_{r,i}^{\mathrm{N}*}(t)\right) \qquad (7)$$

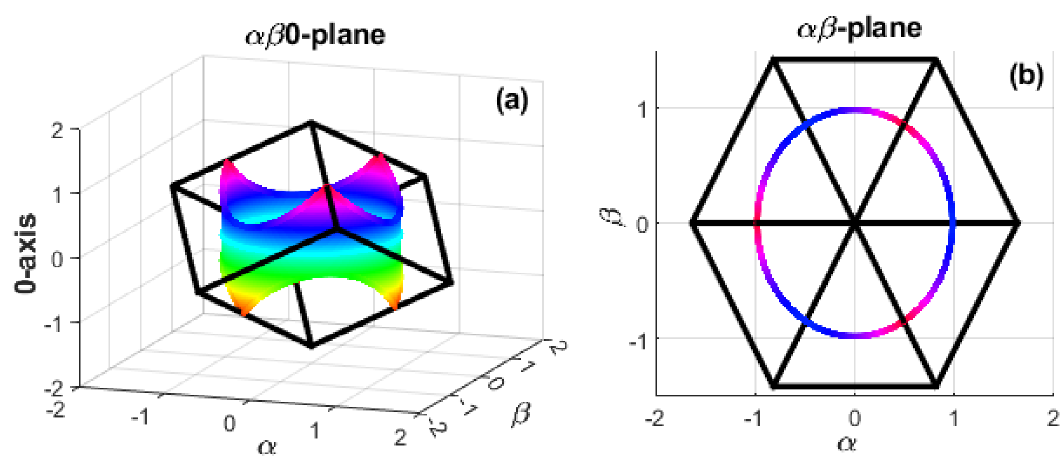

Figure 3. 4: Practical limits of the trajectory drawn by the PWM reference voltage vector for balanced and linear operation region.

From the $\alpha\beta$-plane shown in Fig. 4(b), the range of the PWM reference voltages corresponds to the area limited by circle shape. The radius of the largest circle inscribed on the regular hexagon gives the maximum output line-to-line achievable by the inverter. The reference voltage cylinder surface in Fig. 4(a) can be flattened into a two-dimensional graph as shown in Fig. 5, highlighting the possible common-mode paths at different modulation indexes.

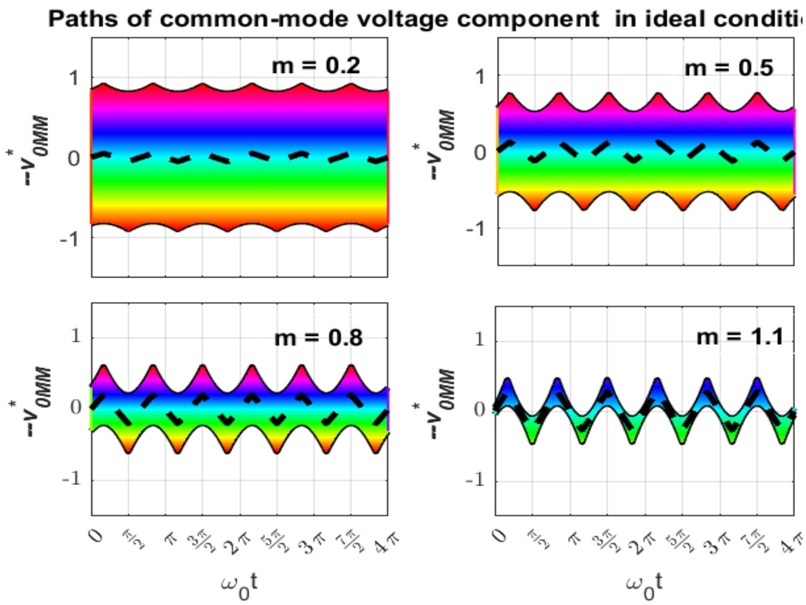

Figure 3. 5: Boundaries of common-mode voltage components for a CHB with $k = 3$ cells per-phase at different modulation indexes under ideal conditions.

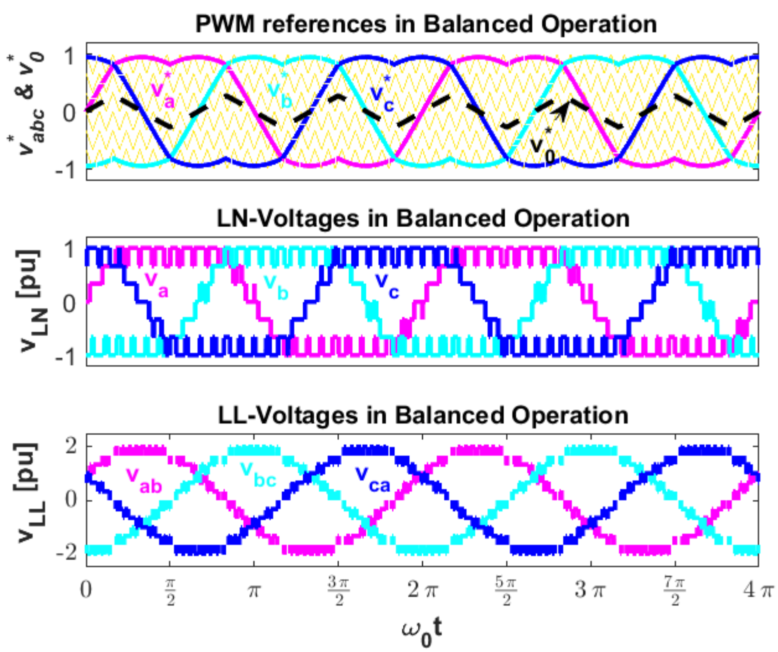

Figure 3. 6: Balanced operation of a 7-level CHB, $f_c/f_0 =$ 25; $m = 1.1$.

It is observed that the boundaries of the common-mode voltage components tend to reduce when the modulation index is increased. Fig. 6 shows a balanced operation of a 7-level inverter controlled by PWM method with a min-max voltage component injection at a modulation index of 1.1.

3.3. A Space Vector Analysis of CHB Operation under Ideal Conditions

3.3.1 Analysis of inverter voltage states under non-ideal conditions

Non-ideal operating condition of CHB refers to the scenario of unequal DC voltage condition [$0 < v_{dc,ij}(\mathrm{p.u.}) < 1$] or the presence of one or more failed and bypassed cells [$v_{dc,ij}(\mathrm{p.u.}) = 0$]. Under any of these operating conditions, the total phase leg voltage on the affected inverter phase reduces its nominal value. Fig.7 shows the space vector diagrams of inverter voltage states under selected unbalanced conditions summarized in Table 2. In this figure, the inverter output voltage states generated under balanced operation ($v_{dc,ij} = 1$) are shown with circles, whereas the actual voltage states under unbalanced conditions are shown in solid red dots for the failed power cells ($v_{dc,ij} = 0$), and in solid yellow dots for an operation with unequal DC voltage sources ($0<v_{dc,ij}<1$). By carefully analyzing Fig. 7, it can be observed that:

- The amplitude of the inverter phase leg voltage $v_i = \sum_{j=1}^{k} v_{dc,ij}$ is a decimal number for unequal DC voltage source conditions, and the inverter voltage states won't vanish. They slightly move at all inside the boundaries of the box, as seen in Fig. 7(b).

- However, when there are failed power cells (i.e., when $v_i = \sum_{j=1}^{k} v_{dc,ij} \in N^*$,,$v_i$ is an integer), some voltage states are lost [Fig. 7(e) and (f)]. A similar behavior can be observed when the inverter is operating with significantly unequal DC-voltage source conditions [Fig. 7(b) and (c)].

Fig. 8 shows the space vector representation of inverter voltage states under non-ideal conditions, defined for $k = 3$ H-bridge cells per phase and voltage vectors supplied such that : $v_{dc,a} = [1\ \ 1\ 1]$, $v_{dc,b} = [0\ 0.2\ 1]$, and $v_{dc,c} = [0.7\ \ 1\ \ 0.3]$. As it can be seen, the inverter cannot produce all the possible voltage states under abnormal operating conditions, which affects the achievable limits of the inverter common-mode voltage quantities during the operation, as discussed in the next subsection.

Table 3. 2 : Operation of a CHB with sample abnormal conditions.

	Cases	$v_{dc,a}$(p.u.)	$v_{dc,b}$(p.u.)	$v_{dc,c}$(p.u.)
Balanced condition	(a)	[1 1 1];	[1 1 1]	[1 1 1]
Operation with faulty cells	(b)	[1 1 1]	[1 1 0]	[1 1 1]
	(c)	[1 1 1]	[0 1 1]	[1 0 1]
Operation with unequal DC sources	(d)	[0.5 1 1]	[1 1 1]	[1 1 1]
	(e)	[1 1 1]	[0.8 1 0.2]	[1 1 1]
	(f)	[1 1 1]	[0.4 0.6 1]	[0.7 1 0]

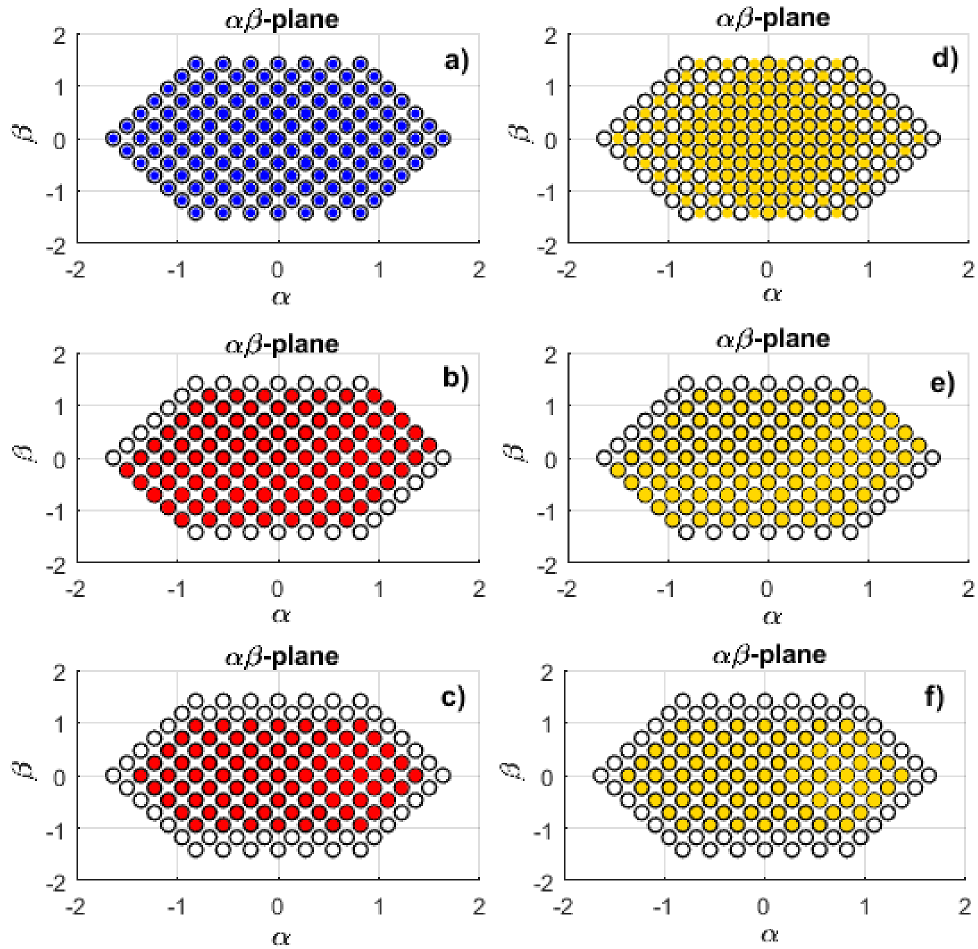

Figure 3. 7: Example of CHB space vector diagrams for different abnormal conditions.

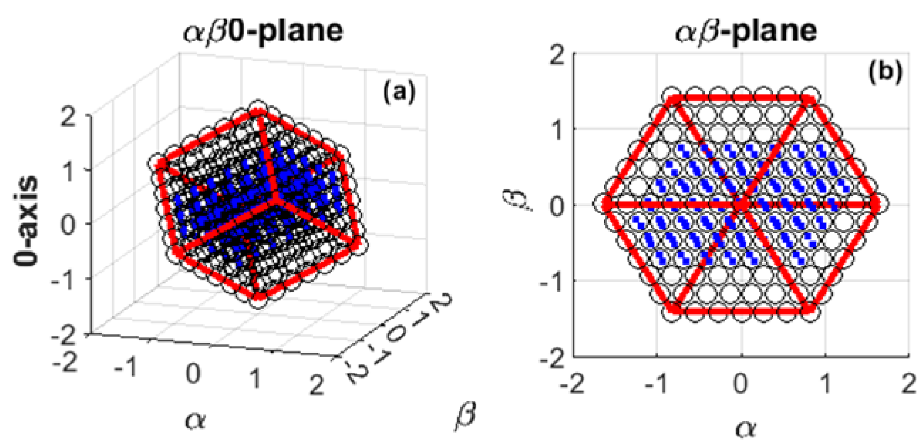

Figure 3. 8: Space vector representation of a CHB with *k*=3 cells under an unbalanced condition : $v_{dc,a} = [1\ 1\ 1]$; $v_{dc,b} = [1\ 0\ 0.2]$; $v_{dc,c} = [1\ 0.3\ 0.7]$.

3.3.2 Analysis of PWM voltages under non-ideal conditions

The analytical expression of the PWM reference voltage when the Clarke transformation is applied is given by :

$$\begin{bmatrix} v_\alpha^{\mathrm{F}*}(t) \\ v_\beta^{\mathrm{F}*}(t) \end{bmatrix} = \begin{bmatrix} \mathrm{A}_\alpha^F cos\omega_0 t + \mathrm{B}_\alpha^F cos\omega_0 t \\ \mathrm{A}_\beta^F cos\omega_0 t + \mathrm{B}_\beta^F cos\omega_0 t \end{bmatrix} \quad (8)$$

where $(\mathrm{A}_\alpha^N, \mathrm{B}_\alpha^N)$, $\left(\mathrm{A}_\beta^N, \mathrm{B}_\beta^N\right)$ are coefficients which depend on the available inverter phase leg voltage magnitude $V_{dc,\mathrm{i}}.i \in \mathbb{P}$. They can be computed as shown in Eq (9):

$$\mathrm{A}_\alpha^F = \frac{1}{3}\left(2V_{dc,\,a} + \frac{1}{2}V_{dc,\,b} + \frac{1}{2}V_{dc,c}\right) \quad (9a)$$
$$\mathrm{B}_\alpha^F = -\frac{1}{2\sqrt{3}}\left(V_{dc,\,b} - V_{dc,c}\right) \quad (9b)$$
$$\mathrm{A}_\beta^F = -\frac{1}{2\sqrt{3}}\left(V_{dc,\,b} - V_{dc,c}\right) \quad (9c)$$
$$\mathrm{B}_\beta^F = \frac{1}{2}\left(V_{dc,\,b} + V_{dc,c}\right) \quad (9d)$$

In balanced operating conditions, $V_{DC,a} = V_{DC,b} = V_{DC,c} = V_{dc} = \sum_{j=1}^{k} V_{dc,ij}$. This is not true under unbalanced operation condition, where $V_{DC,a} \neq V_{DC,b} \neq V_{DC,c}$. In this case, the trajectory of the PWM reference vector describes an elliptic path in the $\alpha\beta$ −plane. Table 3 presents sample unbalanced cases for a 7-level CHB under failed cells and unequal DC sources to analyze the behavior of its reference voltage phasor as discussed in Fig. 9. The red and blue lines represent the trajectory of the reference voltage vector under balanced and unbalanced conditions, respectively. It is observed that, under certain unbalanced conditions, the inverter reference voltage vector forms an ellipse path that may have horizontal [Fig. 9(a)] or vertical [Fig. 9(b)] orientations. The trajectory of the inverter reference voltage phasor can also draw an ellipse with a different inclination angle in other unbalanced conditions as illustrated in [Fig. 9(c)-(d)]. Once this mechanism is understood, it can be predicted that the inverter loses rotational symmetry under unbalanced conditions, resulting in unbalanced output voltages and currents if its PWM reference voltage signals are not appropriately adjusted.

Fig. 10 presents a space vector representation of the output voltage states and PWM reference voltages for an inverter with $k = 3$ cells per phase operating under a specific unbalanced condition ($v_{dc,a} = [1\ 1\ 1]$; $v_{dc,b} = [1\ 0\ 0.2]$; $v_{dc,c} = [1\ 0.3\ 0.7]$). The boundaries of all possible common-mode voltage components in function of the achievable limits of the inverter output voltages are highlighted.

Table 3. 3 Example of non-ideal conditions of a 7-level CHBI with $k = 3$ cells

Cases	$v_{dc,a}$(p.u.)	$v_{dc,b}$(p.u.)	$v_{dc,c}$(p.u.)
(a)	[1 1 0.8]	[0.6 1 0.5]	[0.6 1 0.5]
(b)	[0.4 0 1]	[1 1 0.7]	[1 1 0.7]
(c)	[1 1 1]	[1 1 1]	[0.5 0.4 1]
(d)	[1 0.5 1]	[0.5 0.5 0.3]	[0.5 1 1]

It is shown that, the inverter-output voltage limits have been decreased from their nominal values under this abnormal condition. The unbalanced operation of the inverter can be easily perceived from the elliptical shape of its voltage phasor in the $\alpha\beta$-plane as shown in [Fig. 10(b)]. The altered PWM reference voltage cylinder surface vector in Fig. 10(a) can be flattened to a two-dimensional graph, and the new limits of all the common-mode voltage components are shown in Fig. 11. It is shown that the possibility of injecting an appropriate homopolar voltage component to adjust the behavior of the inverter's differential-mode quantities.

Adding an appropriate common-mode voltage to the inverter reference voltages influences the current flow into the inverter's phase, maintaining balanced three-phase inverter output currents under unbalanced conditions [20], [28], but the zero-sequence injection-based control methods may not be sufficient to provide proper compensation in terms of maintaining balanced line-to-line voltages to the load. Fig. 12 shows the LN-voltage and LL-voltage waveforms for a CHB with $k = 3$ cells per phase operating under an abnormal condition ($v_{dc,a} = [1\ 1\ 1]$; $v_{dc,b} = [1\ 0\ 0.2]$; $v_{dc,c} = [1\ 0.3\ 0.7]$). As can be seen, the inverter phase and line voltages remain unbalanced because no compensation control technique has been applied during the operation process. The following section suggests a compensation control method for CHB operation under non-ideal conditions. The proposed control method involves moving the inverter floating neutral point by adjusting the inverter phase voltage angles to balance output currents and maximize the utilization of remaining operative HB cells under a given non-ideal condition.

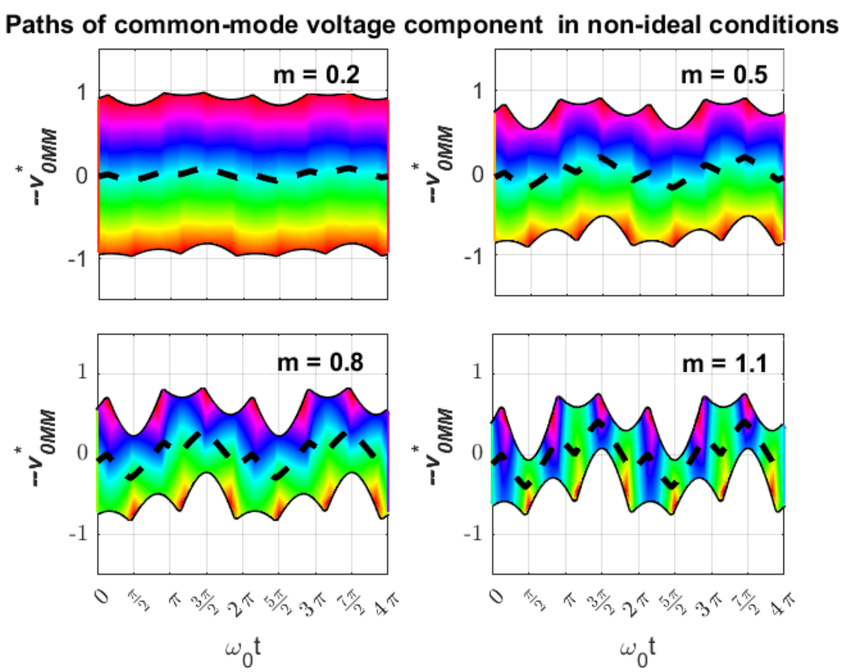

Figure 3. 9: Boundaries of common-mode voltage components for a CHB with $k = 3$ cells at different modulation indexes under a non-ideal condition.

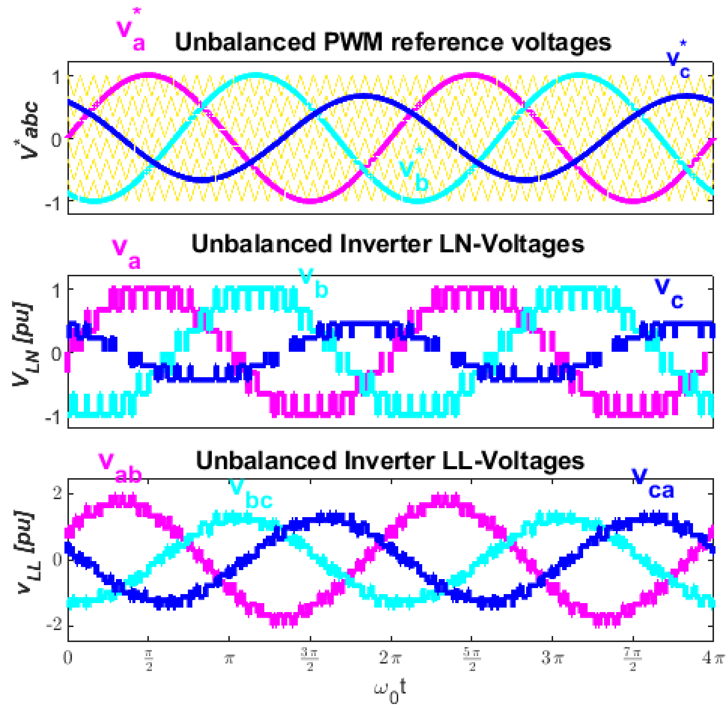

Figure 3. 10: An Operation of a CHB with $k = 3$ cells per phase under a non-ideal condition ($v_{dc,a} = [1\ 1\ 1]$; $v_{dc,b} = [1\ 0\ 0.2]$; $v_{dc,c} = [1\ 0.3\ 0.7]$).

3.4. A Generalized Neutral-shift Strategy suitable for CHB Operation under Non-Ideal Conditions

The proposed generalized neutral-shift method assumed that the phase angles between a and b or c are no longer $2\pi/3$, and the inverter reference voltages can be expressed as given in Eq. (10):

$$\begin{cases} v_a^*(t) = V_{dc,a}\cos(\omega_0 t) \\ v_b^*(t) = V_{dc,b}\cos(\omega_0 t - \theta_{ab}) \\ v_c^*(t) = V_{dc,c}\cos(\omega_0 t - \theta_{ca}) \end{cases} \quad (10)$$

The analytical expression of the corrected PWM reference voltage when applied the Clarke transformation is given in Eq. (11). The parameters $A_\alpha^C, B_\alpha^C, A_\beta^C, B_\beta^C, A_0^C,$ and B_0^C of the PWM reference voltage phasor under these circumstances can be determined by:

$$\begin{bmatrix} v_\alpha^{C*}(t) \\ v_\beta^{C*}(t) \\ v_0^{C*}(t) \end{bmatrix} = \begin{bmatrix} A_\alpha^C cos\omega_0 t + B_\alpha^C cos\omega_0 t \\ A_\beta^C cos\omega_0 t + B_\beta^C cos\omega_0 t \\ A_0^C cos\omega_0 t + B_0^C cos\omega_0 t \end{bmatrix} \quad (11)$$

$$A_\alpha^C = \frac{1}{3}\left(2V_{dc,a} - \frac{1}{2}V_{dc,b}\cos\theta_{ab} - \frac{1}{2}V_{dc,c}\cos\theta_{ca}\right) \quad (12a)$$

$B_\alpha^C = -\frac{1}{3}\left(V_{dc,b}\sin\theta_{ab} - V_{dc,c}\sin\theta_{ca}\right)$ (12b)

$A_\beta^C = -\frac{\sqrt{3}}{3}\left(V_{dc,b}\cos\theta_{ab} - V_{dc,c}\cos\theta_{ca}\right)$ (12c)

$B_\beta^C = \frac{1}{2}\left(V_{dc,b}\sin\theta_{ab} + V_{dc,c}\sin\theta_{ca}\right)$ (12d)

The parametric ellipse equation in the $\alpha\beta$-plan defined by the PWM reference voltage vector under unbalanced conditions can be expressed as shown in Eq. (13).

$$Px^2 + Qxy + Sy^2 + T = 0 \quad (13)$$

$$P = \left(A_\beta^C\right)^2 + \left(B_\beta^C\right)^2;\ Q = -2\left(A_\alpha^C A_\beta^C + B_\alpha^C B_\beta^C\right) \quad (14)$$

$$S = (A_\alpha^C)^2 + (B_\alpha^C)^2;\ T = -\left(A_\alpha^C B_\beta^C - A_\beta^C B_\alpha^C\right)^2 \quad (15)$$

If $Q \neq 0$, the general ellipse equation can be written as follows.

$$\frac{\left[(x-C_x)\cos\theta+(y-C_y)\sin\theta\right]^2}{R_x^2} + \frac{\left[(x-C_x)\sin\theta+(y-C_y)\cos\theta\right]^2}{R_y^2} \quad (16)$$

Where R_x, R_y, and θ stand for the major-axis, minor-axis, and the tilt angle of the ellipse (blue line) respectively, and they are highlighted in Fig. 13. The coordinates (C_x, C_y) is the center of the ellipse, and its tilt angle θ can be determined by the following relationship:

$$tan\,\theta = \frac{2Q}{P-S} \quad (17)$$

The fundamental the proposed neutral-shift control relies on finding the new achievable circle from the ellipse equation generated by the inverter PWM reference voltages in the $\alpha\beta$ $-$plane under unbalanced conditions. This is achieved by establishing appropriate criteria that transforms the ellipse equation into a circle equation. The new circle equation (18b) of the corrected PWM reference voltage can be obtained by fulfilling the condition given in Eq. (18a). Fig.13 illustrates how an inverter PWM reference ellipse shape is transformed into a circle shape (green line) when applying the proposed neutral-shift strategy.

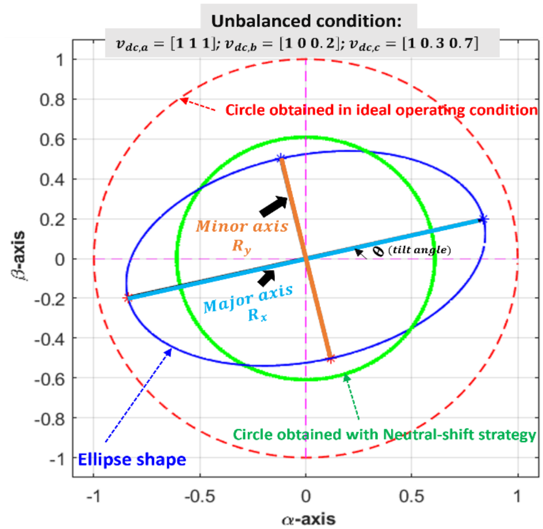

Figure 3. 11: Transformation of an inverter PWM reference ellipse shape into a circle shape using the proposed neutral-shift strategy.

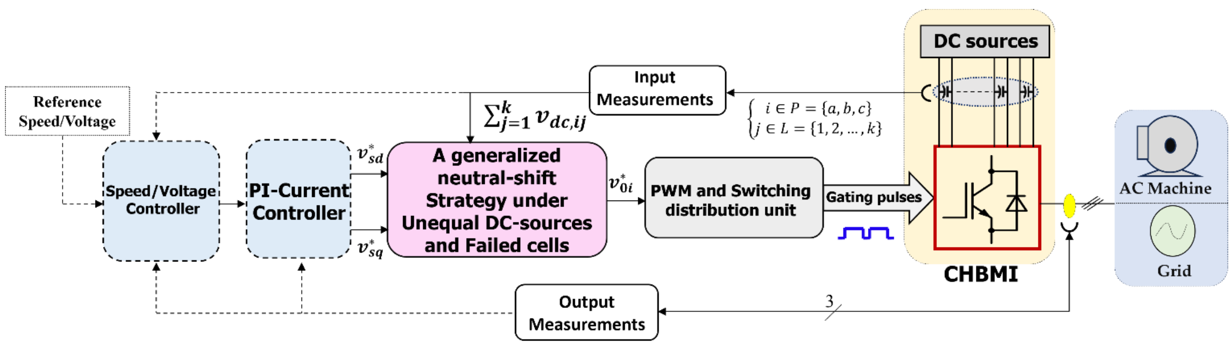

Figure 3. 12 : The block diagram of the feedback control scheme with the suggested generalized neutral-shift strategy

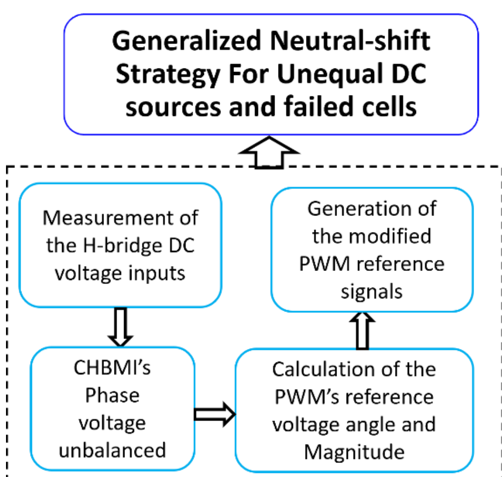

Figure 3. 13 : Implementation steps of the suggested neutral-shift strategy.

$$\begin{cases} Q = 0 \\ S = P \end{cases} \tag{18a}$$

$$\frac{S}{T}x^2 + \frac{P}{T}y^2 = 1 \tag{18b}$$

The corrected PWM reference voltages are designed to neutralize the effects of unbalanced LN voltages, making it possible to achieve balanced output LL voltages at any non-ideal conditions.

Fig.14 shows the block diagram of the overall feedback control scheme with the suggested generalized neutral strategy. The first stage of this scheme is the outer control loop, which varies based on the application. For instance, in motor drive applications, it regulates the speed/torque of the electrical machine. In PV-based or battery-based energy conversion systems, it regulates the sum of the DC-link voltages to determine the overall active power P required to control the system. The outer voltage controller loop indirectly gives the active power reference in the form of d-axis current reference. The q-axis current reference is chosen depending on the system requirements, typically set to zero to inject the energy into the grid with a unity power factor. dq-currents are also regulated by a proportional-integral (PI) controller, which delivers the inverter reference voltage in the synchronous frame, which are transformed back to the three-phase coordinates in stage 3, where the suggested neutral-shift strategy (Fig. 15) under non-ideal conditions is applied. In Stage 3, inverter voltage reference angles and magnitudes are adequately adjusted using g the neutral shift strategy under unequal DC voltages or failed cells. Finally, a PD-PWM method in stage 4 is used to generate gating signals to control the power switches.

Fig. 16 depicts inverter voltage waveforms of an inverter with $k = 3$ cells per-phase ($v_{dc,a} = [1\ 1\ 1]$; $v_{dc,b} = [1\ 1\ 1]$; $v_{dc,c} = [1\ 0.4\ 0.6]$) and controlled by the suggested neutral-shift method. It is clearly observed that, the inverter phase voltages are remained unbalanced, however the inverter line voltages have been successfully rebalanced by properly adjusting its PWM reference phase voltages using the neutral-shift strategy. The min-max voltage component is injected to extend the inverter modulator linear region under unbalanced conditions.

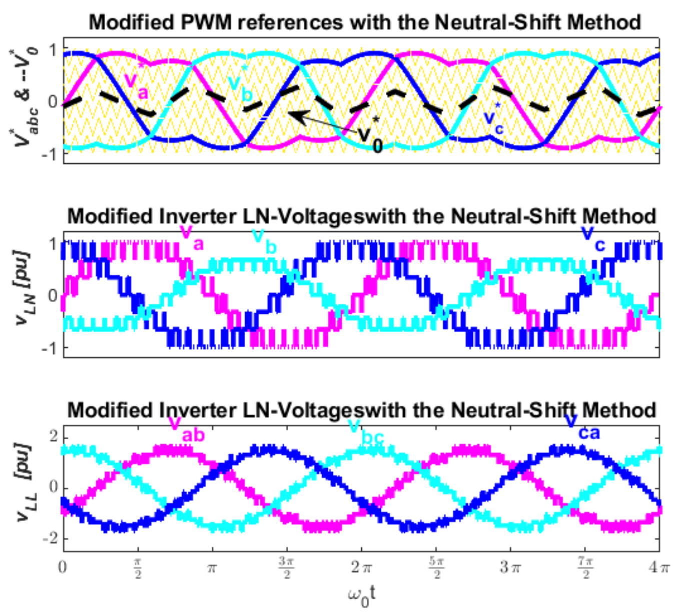

Figure 3. 14 Voltage waveforms for a CHB with $k = 3$ cells per phase operating under corrected mode using the neutral-shift control strategy.

3.5. Experimental Validation and Test results

3.5.1 Experimental Setup description

This section discusses steady-state experimental results obtained from a scaled-down laboratory test bench equipped with $k = 3$ AC-DC-AC Semikron SK 10GD12T4ET power modules. The three-phase 7-level inverter is connected to a Y-connected R-L load, switching each phase leg at 1 kHz. The 15-ohm resistance balances the lab's system setup performance and experimental constraints, such as the inverter's power source's voltage and current ratings. This value was selected to ensure the safe operation and repeatability of the experiments at lower current ratings under various DC voltage conditions and cell failures. The proposed compensation neutral-shift control strategy is implemented and executed on Simulink real-time target PC using a NI-PCI 6229 board to redirect the appropriate PWM command signals to the inverter gate drives. The unequal DC-voltage conditions for the inverter were performed by feeding each inverter H-bridge cell through a DC-power supply, model NES-1000-80 (0 to 80 V). A bypassed contactor is connected at the output of an individual H-bridge cell and is used to emulate the system operation with one or more faulty cells. The overall experimental system picture is depicted in Fig. 17, and its key parameters are summarized in Table 4. Several abnormal operating conditions were tested to emulate the inverter's unbalanced operation with unequal DC-voltage and fail cell conditions. The following selected abnormal conditions summarized in Table 5 are presented and discussed for simplicity.

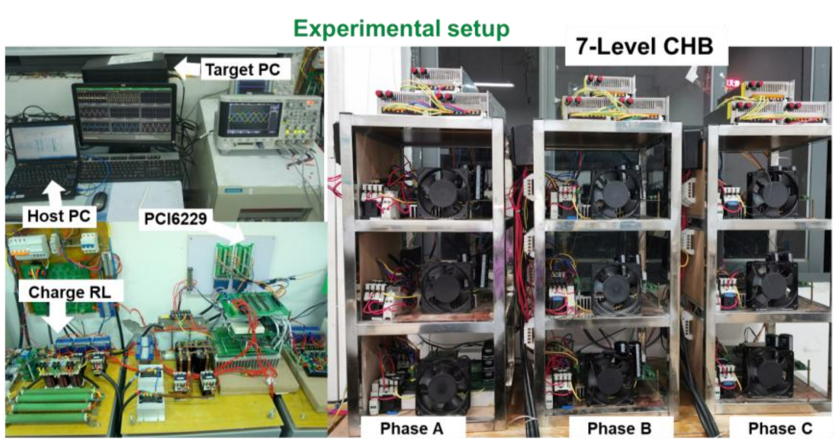

Figure 3. 15 Picture of the scaled-down laboratory prototype

Table 3. 4 : Key parameters of the experimental system.

No	Devices	Characteristics
1	IGBT	Semikron SK 10GD12T4ET 1200 V/15 A
2	DC Link capacitors	Photo Flash 3600μF, 450V/360w
3	DC-power supply	NES-1000-80 rated at 80 V, 12.5 A.
4	Gate drives	Semikron SKHI 61. R
5	Voltage sensors	model CHV-100/800.
6	Current sensors	TKC50BR 4.0V/50A
8	Resistive load	15 Ω
9	Line reactor	TLDKQ 8A/30mH
10	Data acquisition board	Dual NI-DAQ PCI 6229
11	Oscilloscope	Tektronix MD04104C

Table 3. 5 : Selected tested abnormal operating conditions.

Cases	$v_{dc,a}$(V)	$v_{dc,b}$(V)	$v_{dc,c}$(V)
(1)	$50 * [0\ 1\ 1]$	$50 * [1\ 1\ 1]$	$50 * [1\ 1\ 1]$
(2)	$50 * [0.6\ 1\ 0.4]$	$50 * [1\ 1\ 1]$	$50 * [1\ 1\ 0]$
(3)	$50 * [1\ 1\ 1]$	$50 * [1\ 1\ 1]$	$50 * [0.8\ 0\ 0.2]$

3.5.2 Test results and Discussion.

3.5.2.1 Steady-state time-domain experimental results

Figs 18-20 show the corresponding experimental results of each unbalanced operating condition in Table 5. In each figure, both inverter voltage and current waveforms obtained under abnormal [Figs 18(a)-20(a)] and corrected [Figs 18(b)-20(b)] modes waveform. In **Fig. 18 (case 1)**, the three-phase system imbalance is only caused by a bypassed cell (cell#1) in phase *A*. **Fig. 19 (case 2) shows,** a bypassed cell in phase *A*, while all the H-bridge cells in phase *C* are fed with different DC-voltage values. Finally, **in Fig. 20 (Case 4),** the imbalance of the three-phase system results from two scenarios : a bypass cell in inverter phase *C* and its remaining operational H-bridge cells are supplied by different DC-voltage magnitudes. Figs 18(a)-20(a) indicate the unbalanced state of the inverter output voltage and current waveforms when no compensation control method applied during abnormal conditions. However, in corrected inverter operation mode, the proposed neutral-shift compensation control technique, which has modified the inverter PWM reference voltage amplitudes and angles, is used to keep the balanced inverter LL-voltages, even if the inverter LN-voltage remains unbalanced, as shown in Figs 18(b)-20(b) The three-phase inverter output currents for each abnormal case have been successfully re-balanced in corrected mode.

3.5.3 Analysis of experimental data using Clarke Transformation

This section discusses the space vector diagrams of voltage and current and the associated spectra of experimental data to validate the correctness of the proposed analysis approach using the Clarke transformation. The experimental waveforms (Fig. 18) were saved as text files and later imported into MATLAB for further analysis. We then applied the Clark transformation to the data in both the time and frequency domains. Figs. 22 and 23 displays the results of the transformation both before and after processing. Before, Fig. 21 shows the inverter phase voltage, current space vector diagrams, and their respective spectra in $\alpha\beta$-plane under ideal conditions ($v_{dc,a} = [50\ 50\ 50]$ V; $v_{dc,b} = [50\ 50\ 50]$V ; $v_{dc,c} = [50\ 50\ 50]$ V). It can be observed that the inverter current Clark's vector pattern for balanced operation is a perfect circle. From the harmonic point of view, the inverter voltage and current spectra do not contain carrier band and triple baseband harmonics in the $\alpha\beta$-plane. They are canceled by differentiating inverter phase voltage/current using the Clarke transformation. This is not valid under an unbalanced operation caused by non-ideal conditions, as shown in Fig. 22.

The experimental case studied in Fig. 22 is similar to the one discussed in Fig. 18 ($v_{dc,a} = [0\ 50\ 50]$ V; $v_{dc,b} = [50\ 50\ 50]$ V; $v_{dc,c} = [50\ 50\ 50]$ V). As can be observed, the output current phasor has an elliptical shape, indicating the inverter's unbalanced operation, which leads to more harmonic distortions than under ideal operation. The spectrum of the inverter voltage phasor in Fig. 22 contains two relevant harmonic components with high magnitude. The first is a triplen baseband harmonic component at the frequency of 150Hz ($3 \cdot f_0$), while the second is a carrier-band harmonic component at the frequency of 1000Hz (f_c). It is evident that compared to ideal operation (Fig. 19), these unwanted components are no longer common-mode harmonics in a faulty condition. Therefore, they weren't canceled out through the differentiation of the inverter phase voltage using the Clarke transformation in $\alpha\beta$-plane.

Fig. 23 depicts the voltage and current phasor as well as their spectra under the unbalanced operation of the inverter when controlled by the proposed neutral-shift method. The voltage phasor for unbalanced operation without the neutral-shift method (Fig. 22) differs from the one when using the neutral shift, as shown in Fig. 23

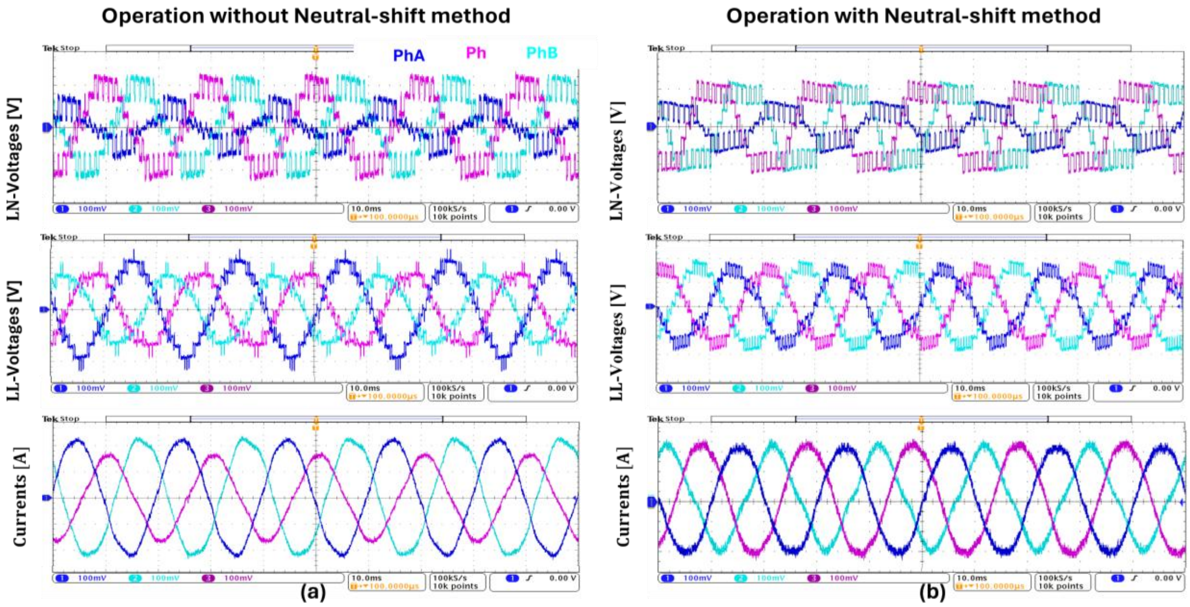

Figure 3. 16 Voltage and current test results for a CHB with $k = 3$ cells per phase under operating condition case 1: $v_{dc,a} = [0\ 50\ 50]$ V; $v_{dc,b} = [50\ 50\ 50]$ V; $v_{dc,c} = [50\ 50\ 50]$ V: (a) Operation without the proposed neutral-shift method; (b) Operation with the proposed neutral-shift method.

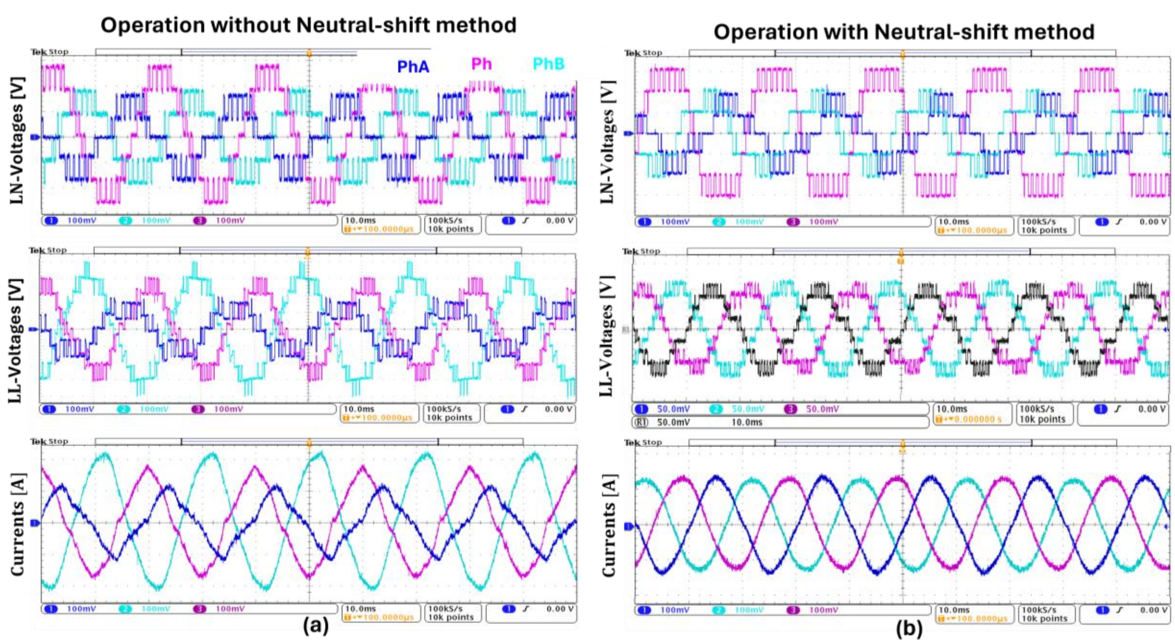

Figure 3. 17 Voltage and current test results for a CHB with $k = 3$ cells per phase under operating condition case 2: $v_{dc,a} = [\ 20\ 50\ 30]$V; $v_{dc,b} = [50\ 50\ 50]$V; $v_{dc,c} = [50\ 50\ 0]$V: (a) Operation without the proposed neutral-shift method; (b) Operation with the proposed neutral-shift method.

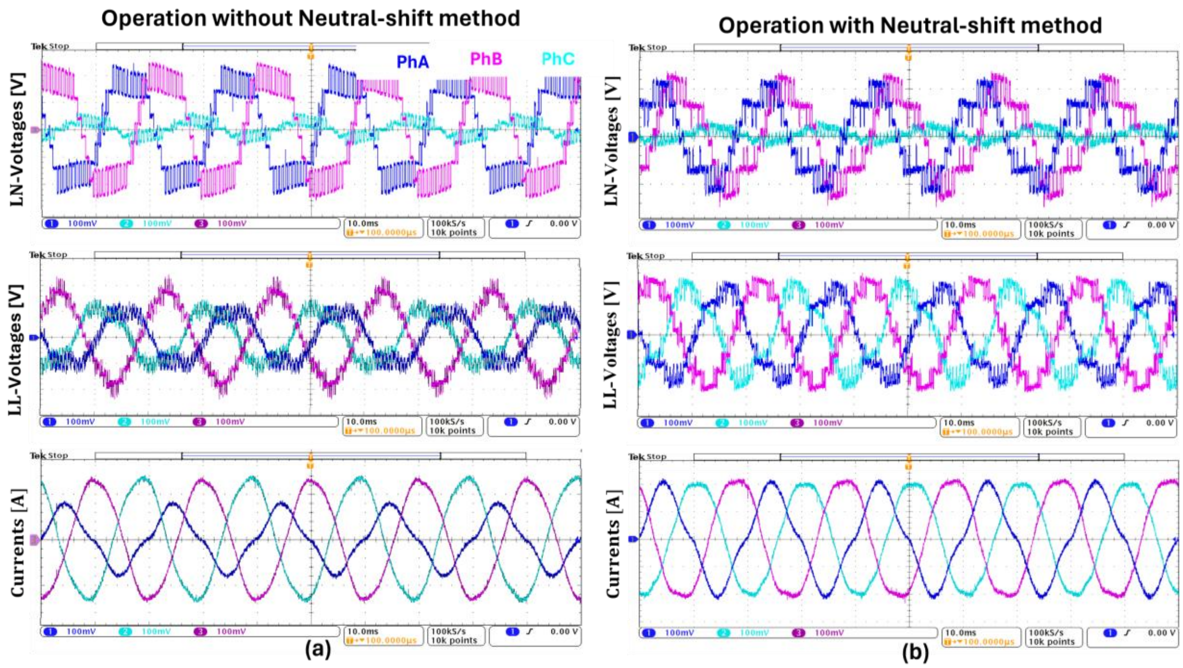

Figure 3. 18 Voltage and current test results for a CHB with $k = 3$ cells per phase under operating condition case 3: $v_{dc,a} = [50\ 50\ 50]\mathrm{V}$; $v_{dc,b} = [50\ 50\ 50]\mathrm{V}$; $v_{dc,c} = [40\ 0\ 10]\mathrm{V}$: (a) Operation without the proposed neutral-shift method; (b) Operation with the proposed neutral-shift method

This adjustment successfully rebalanced inverter line voltages and currents and modified the inverter phasor shapes in the $\alpha\beta$-plane. As a result, the rebalanced three-phase inverter output forms a circular shape in the ab-plane even if its phase voltage remains unbalanced. However, from the harmonic analysis point of view, the suggested neutral-shift method hasn't eliminated some undesirable harmonic content, such as triple baseband harmonic component at the frequency of 150Hz ($3 \cdot f_0$).

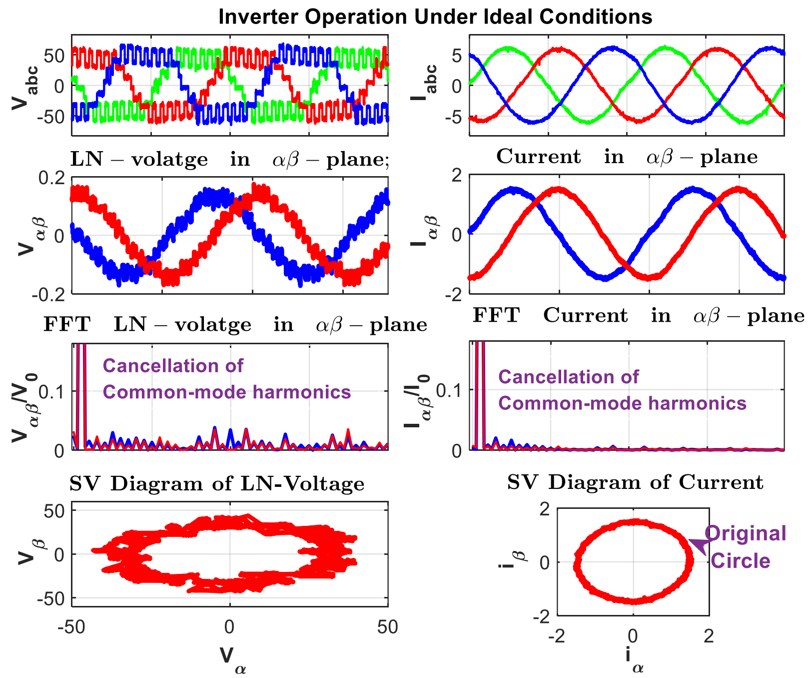

Figure 3. 19 : Inverter voltage and current phasor and their spectra under a balanced operation : ($v_{dc,a} = [50\ 50\ 50]$; $v_{dc,b} = [50\ 50\ 50]$; $v_{dc,c} = [50\ 50\ 50]$).

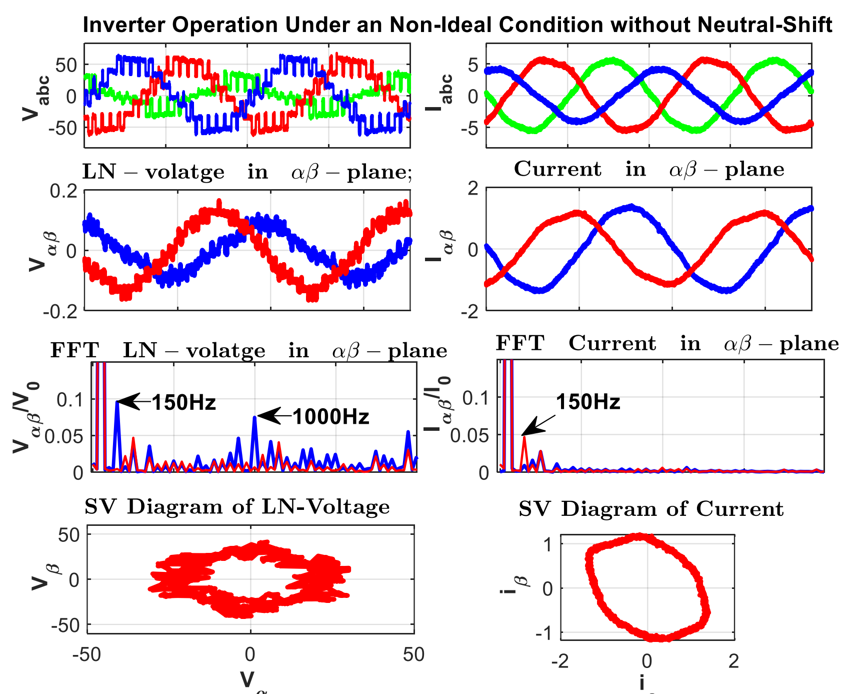

Figure 3. 20 Inverter voltage and current phasor and their spectra under an unbalanced operation ($v_{dc,a} = [0\ 50\ 50]$; $v_{dc,b} = [50\ 50\ 50]$; $v_{dc,c} = [50\ 50\ 50]$) without the neutral-shift method.

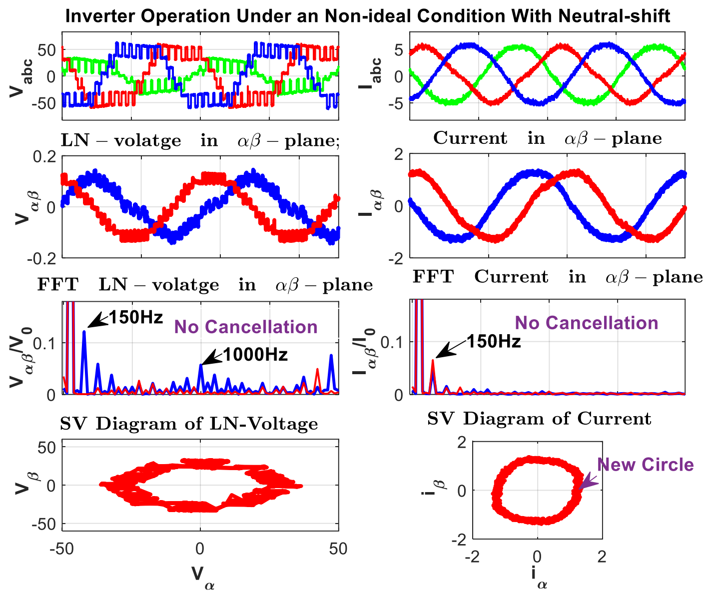

Figure 3. 21 : Inverter voltage and current phasor and their spectra under an unbalanced operation ($v_{dc,a} = [0\ 50\ 50]\mathrm{V};\ v_{dc,b} = [50\ 50\ 50]\ \mathrm{V};\ v_{dc,c} = [50\ 50\ 50]\mathrm{V}$) with the neutral-shift method.

This limitation can be addressed by optimizing the switching strategy of the proposed neutral-shift strategy to mitigate some classes of harmonics during the compensation control process of the inverter's unbalanced operation, as discussed in [11].

3.6 Conclusion article 2

This chapter has proposed a graphical analysis of the interaction between cascaded H-bridge inverter output voltage states and its PWM reference voltage using Clarke transformation under non-ideal conditions, such as faulty cells, DC-source failure, and unequal DC voltages. The Clarke transform matrix was used to convert the inverter's three-phase quantities to differential-mode and common-mode quantities to better understand its output voltage and current phasor shapes under non-ideal operating conditions. The proposed study is also crucial in identifying the linear region boundaries of all potential common-mode voltage components that can be injected under non-ideal conditions. Understanding this mechanism makes finding an appropriate homopolar component to maintain balanced inverter output currents under non-ideal conditions more straightforward. A generalized neutral-shift strategy was also proposed to produce balanced inverter line voltages and currents under non-ideal conditions. The effectiveness of the suggested control strategy was proven through experiments conducted on a laboratory prototype based on a 3-cell per-phase cascaded H-bridge inverter. Finally, an analysis of the experimental inverter output voltage and current data and their respective spectra in $\alpha\beta$-plane was conducted to validate the relevance of the suggested study. The readjusting of the inverter voltage reference phase voltage angles and amplitudes through the suggested control scheme redistributes the ON and OFF times, directly impacting the inverter's switching and conduction losses. Future work will investigate these aspects in detail, assessing how the proposed method influences the energy distribution among modules and quantifying its effects on the inverter power losses and efficiency.

CHAPTER 4 - VARIABLE FREQUENCY DRIVES-INDUCED TORSIONAL STRESSES IN PUMPED HYDROPOWER STORAGE APPLICATIONS

4.1 Introduction article 3

Despite consistent maintenance and monitoring equipment installed in pumped storage hydropower (PSH) facilities, many shafts and electrical component failures are reported, possibly resulting from undetected sources. These sources include undetectable vibrations or, in certain conditions, high-frequency mechanical or electrical harmonics. This chapter presents a direct method for plotting Campbell diagrams of large motors supplied by variable frequency drives (VFDs) for torsional analysis purposes in PSH systems. These diagrams display the precise locations where torsional stress components induced by VFDs can interfere with shaft resonance modes. The method simplifies the determination of the magnitude of stimulus forces in the motor airgap that may threaten the shaft. The method has been successfully applied to two-level, three-level neutral-point clamped, and seven-level cascaded H-bridge multilevel inverters, which are commonly used industrially available VFD topologies for pumped PSH plants. The chapter also discusses the theoretical motor-pump voltage, current, and torque spectra when driven by a cascaded H-bridge multilevel converter operating with bypassed and faulty cells. The accuracy of the theoretical developments is supported by selected simulations results at different operating points and different fault conditions. Hybrid experimental-numerical VFD-induced harmonic stress analysis is also performed to demonstrate the relevance of the proposed study.

4.2 Background

Hydropower plants and pumped storage hydropower (PSH) facilities can offer significant services to the grid. With their ability to offer bulk energy storage and balance the grid, these facilities play a vital role in ensuring a reliable electricity supply [168]. They can enable frequency control with large inertia and power reserves to improve grid flexibility and resilience. An example of a single-line diagram of a reversible hydropower storage plant is shown in Figure 4.1. In one operation mode the electricity is utilized to move pump water from a lower reservoir to an upper reservoir when all the energy produced cannot be consumed [117], [118].

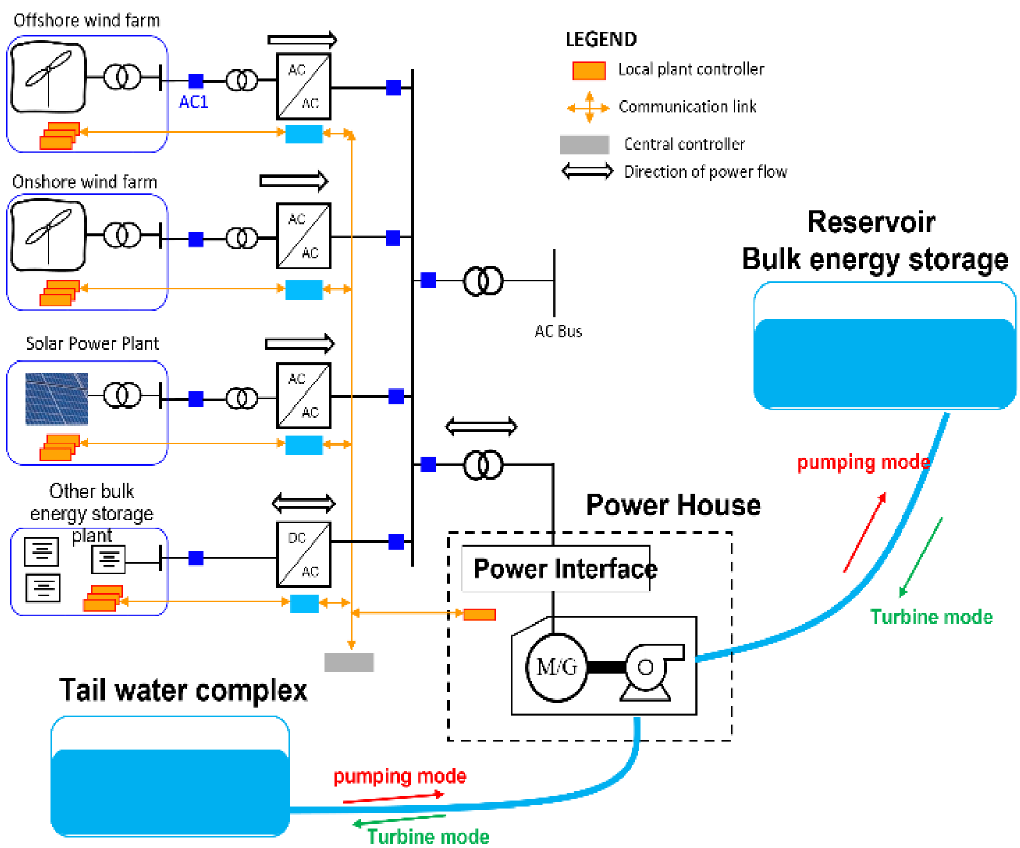

Figure 4. 1 : A single-line diagram of a pumped storage hydropower plant.

In such system configuration, the motor-pump controls the water flow. When needed, the stored potential energy of water is converted into a kinetic energy to drive the hydro-turbine which generates the electricity to be injected to the grid [117]. Despite monitoring equipment and regular maintenance, shaft element failures in pumped storage hydropower systems are still being reported in the literature. These failures are often caused by undetected sources, which can significantly impact the overall system performances [119]-[122]. The sources include undetectable vibrations, mechanical or electrical harmonics. They may induce premature material fatigue and ageing, leading to accelerated wear, tear, and premature system failure [123], [124]. When a variable frequency drive (VFD) is used, risks of low-order vibrations increase. The VFD-induced vibrations may interfere with the natural frequencies of subsystems, leading to an increase in drivetrain torsional strain [125]-[127]. The Campbell diagram is a commonly used tool to show the interference points between the machine's airgap torque and shaft's natural frequencies [128]. These locations are those where torsional stresses may increase to threaten the shaft components. These Campbell diagrams depend on the VFD topology [1129], [130]. The industry does not have a clear method explaining how to plot Campbell diagrams resulting from VFDs. This chapter covers this gap in the practicing engineering community for VFD topologies commercially available and commonly used in PSH applications.

Engineers in charge of designing powered dams and PSH facilities must have a tool for performing accurate torsional analysis and stress evaluation of the rotating shafts. International standards require such analysis to ensure the integrity of the rotating shaft in its entire operating range [131-133]. Also, operational engineers developing predictive maintenance tools to the extend lifetime of these plants need an instrument that can provide vital information on critical shaft elements [134]. They also need a tool for conducting accurate root cause failure analysis shall a shaft element fail [135]. Finally, research and development engineers conducting the development of digital tools for replicating static and dynamic behaviors of PSH plants, such as digital twins, may need to include in their models the dynamics of the shaft, the generator, the VFD, and its controls, as well as the transformer and the transmission line [136]. Such tools may need to include the reversible energy flow from renewable sources to grid-scale storage and the impact of both grid contingencies and water-induced fluctuation on their models [137], [138].

This chapter focuses on developing time-domain models of torsional stresses subjected to shaft elements, as illustrated in Figure 4.2. First, the critical shaft components should be identified, such as bearings, rings, gear, turbine blades, and generators. Then design data and operational parameters are required. They include the type of AC machine, the type of VFD and its modulation parameters (carrier and operating frequencies), shaft materials and their strength, and transmission line and transformer impedance. They can be gathered from different sources, including PSH operators, equipment manufacturers, and open sources. The chapter provides both time- and frequency-domain analytical expressions of torsional stresses generated by the VFDs. It also considers other sources of torsional stresses, such as water flow and internally generated mechanical-induced stresses possibly resulting from the failure of the shaft's elements. The results can be utilized to evaluate component degradation models. They can also be integrated into existing or digital twins under development, clearly predicting equipment lifetime [139]. Furthermore, tools such as electronic vibration suppression systems can utilize the results of this investigation to reduce the torsional stresses of the shaft's elements.

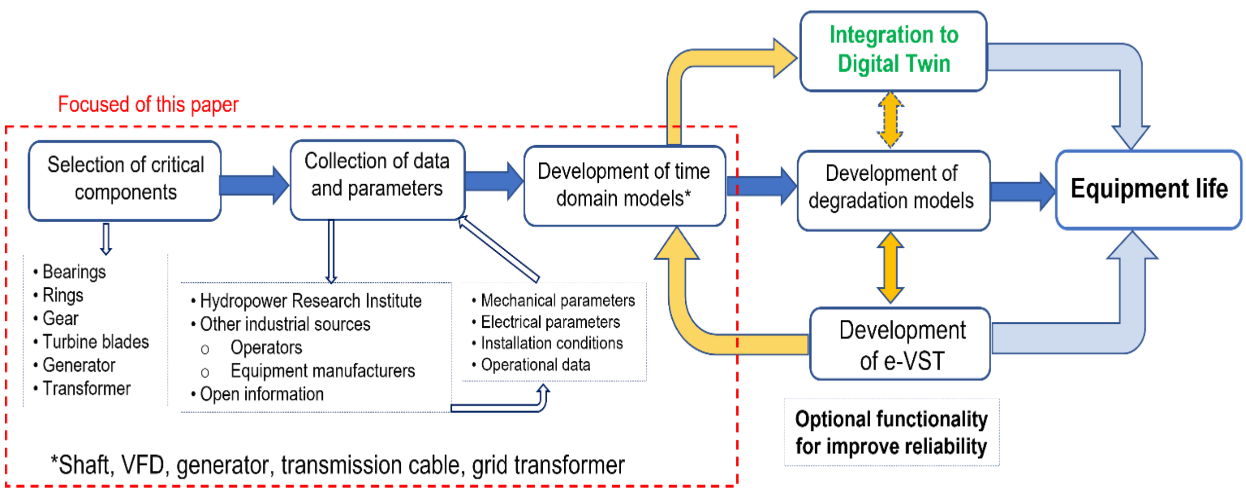

Figure 4. 2 : Flowchart to develop equipment life estimation of PSH mechanical components.

4.3 Torque components on a psh shaft system

4.3.1 Ageing elements from torsional stress

An element aging is an occurrence of irreversible changes in its material, affecting its ability to perform the required service [140]. Causes of aging are factors imposed by operation, environment, technology, or test that influence the performance of the component subjected to stresses [141]. The dependence of aging A on the property p can be written as :

$$A = F(p) \tag{4.1}$$

Where $p = P/P_0$ is the observed property P with respect to the unaged property P_0 Aging A is a dimensionless quantity. Failure occurs when p reaches a limit value p_L . The process of fatigue failure is divided into two parts : the formation of the fatigue fissure itself and the growth of the fissure. It is understood that at the start of the process, $A = 0$ (no crack), and at the end, when the crack appears, $A = 1$ (apparition of irreversible change) [142], [143]. The aging rate is :

$$R = \frac{dA}{dt} \tag{4.2}$$

R is assumed to depend only on stresses applied to the element, and not on time t, which is the monotonic time variation of P Also, the machine element is subjected to a stress of magnitude $S_j (j = 1....N)$ a certain number of times per unit of operation. The unit of operation can be chosen as a revolution per second. It is possible to predict how long an element, subjected to a cyclic stress can operate before a crack occurs. Usually, the *S-N* curves or the Woehler curves" are used for this purpose. The cyclic stress level against the number of cycles to material failure [144]. A failure can occur even if the stress is less than the yield strength (endurance limit) of the material. The effective stress applied to an element is usually a combination of both a mean stress and an oscillating component with a constant magnitude. The mean shear stress does not influence the fatigue life of a ductile structural component subjected to a cyclic load [145], [146]. In real life, the frequency of the stress cycles can become a factor if it is near the natural frequency of the shaft. In that case, its magnitude increases proportionally to time until it reaches a final value that depends on the damping coefficients.

4.3.2 Possible sources of vibration in PSH shafts

There are three possible sources of vibrations in PSH shafts that are discussed in this section : hydraulic-induced, mechanical-induced, and electrical-induced vibrations [147].

4.3.2.1. Hydraulic-induced vibrations

From the electrical machine point of view, these vibrations may be seen as process or load-induced vibration components. They may result from the hydro-dynamic of the high-pressure water propagating through the upper or lower penstock pipes and water moved by the turbine blades [148].

4.3.2.2. Mechanical-induced vibrations

Mechanical vibrations are those resulting from the mechanical elements of the shaft. They may be generated from structural irregularities, inadequate lubrication, destruction of turbine or pump blades, and destruction of gear teeth [149]. They may also result from physical installation conditions of the system, such as frame vibration resulting from poor mechanical connections of the machine frame, physical vibrations of the casing where the machine is tightened to the building (e.g., micro-seismic vibrations resulting from other equipment) [150], [151].

a) Electrical-induced vibrations

When an AC motor is introduced in a rotating shaft system, new stimulus forces are created in the form of electromagnetic airgap torque [152]. Furthermore, when the motor is supplied by a VFD for an adjustable speed operation, the airgap torque is theoretically having an infinite number of periodic components, due to distorted voltages and currents [152]. The torque components are oscillatory with dynamic frequencies and magnitudes. The machine' design also produces oscillating torque (cogging, commutation, and reluctant) [153].

4.3.3 Formulation of non-electrical-induced torque

The shaft stress formulated in the form of electromagnetic torque, $t_e(t)$ generated in the machine's airgap can be grouped into two main categories as mathematically formulated in (4.3) :

i. Non-electrical-induced components, $t_{NE}(t)$, which result both from mechanical and hydraulic vibrations.

ii. Electrical-induced components, $t_E(t)$, which are generated from the voltage supply (e.g., VFD).

$$t_e(t) = t_{NE}(t) + t_E(t) \tag{4.3}$$

All *k*-hydraulic and mechanical induced torque are converted to a set of average components, (4.4a), superposed to periodic components with different magnitudes and frequencies (4.4b). The frequencies that are multiples of their original frequency ω_{NE_k}. All *q*-mechanical components (4.3c) have their frequencies proportional to the rotational speed ω_0 of a *p*-pole motor.

$$t_{NE}(t) = \sum_{i=1}^{\infty} T_{NE_{DC},\mathrm{i}} \tag{4.4a}$$

$$+\sum_{k=1}^{\infty}\sum_{j=1}^{\infty} T_{NE,\mathrm{k},\mathrm{j}} \cos\left(k.\omega_{NE_{k,j}} t + \theta_{NE_k}\right) \tag{4.4b}$$

$$+\sum_{q=1}^{\infty} T_{mec,q} \cos\left(q.P.\omega_0.t + \theta_{mec,q}\right) \tag{4.4c}$$

4.3.4 Formulation of electrical-induced torque

As expressed in (4.5), there are two sets of electrical-induced torque components, $t_e(t)$ in the machine's airgap : construction-induced, $t_{eCons}(t)$ and power supply-induced, $t_{eVFD}(t)$:

$$t_e(t) = t_{eCons}(t) + t_{eVFD}(t) \tag{4.5}$$

a) Construction-induced torque components

They result from the imperfection of the machine design and construction (airgap eccentricity, slots of the stator and rotor, manufacturing, and assembly tolerances, etc.). They include cogging, reluctance, and commutation torques, and are proportional to the rotational speed of the machine [154]. They are lumped in (3c) and shown in (4.6).

$$t_{eCons}(t) = \sum_{q=1}^{\infty} T_{mec,q} \cos\left(q.P.\omega_0 t + \theta_{mec,q}\right) \tag{4.6}$$

b) Power supply induced torque components

These are torque components created in the machine's airgap because of the electric power supplying the machine and they are discussed in Section IV.

4.4 Integrated system model for torque analysis

4.4.1 Transmission line and transformer models

The transmission line is modeled as a multiple pi-section system. It can also be modeled as a two-terminal system with passive components with distributed parameters,

R_c, L_c and C_c, [155]. In that case, the cable sending- and receiving-end voltages and currents are related according to (4.7).

$$\begin{bmatrix} v_{SE} \\ i_{SE} \end{bmatrix} = \begin{bmatrix} \cosh(\lambda d) & -z_w \sinh(\lambda d) \\ Y_w \sinh(\lambda d) & -\cosh(\lambda d) \end{bmatrix} \cdot \begin{bmatrix} v_{RE} \\ i_{RE} \end{bmatrix} \tag{4.7}$$

Where the propagation constant of the transmission line over a distance d is given by (4.8a), the cable impedance Z_c, is given by (4.8b); the respective inductive reactance, and capacitive admittance of the cable are (4.8c) and (4.8d):

$$\lambda = \sqrt{L_c C_c} \tag{4.8a}$$

$$Z_c = R_C + jX_c \tag{4.8b}$$

$$Y_c = j\omega C_c \tag{4.8c}$$

$$Z_w = \sqrt{Z_c / Y_c}; \;\; Y_w = 1/Z_w \tag{4.8d}$$

Frequency-dependent resistances r_c, of the cable to replicate the skin effect can be inserted in the capacitor branches. The grid side and the VFD side transformers are modeled as a resistance series connected to an inductance, and they are lumped with the cable impedance, but they can be neglected due to the length of the transmission cable.

4.4.2 Shaft model

A dynamic shaft model can be established using the lumped parameters of the elements, such as their mass moments of inertia, damping coefficients, and stiffness constants derived from Newton's second law shown in (4.9) [156], [157].

$$j\frac{d\theta^2}{dt^2} + D\frac{d\theta}{dt} + K\theta = T_{ext} \tag{4.9}$$

Where *J, D*, and *K* are, respectively, the matrixes of moments of inertia, damping coefficients, and stiffness constants. The dynamic equation (4.9) should be solved with the forced excitations given in the matrix of externally applied forces shown in (4.10). It contains the airgap electromagnetic torque stresses, and the water-flow torque stress. All other components are zeros when there is no failure on the shaft and non-zero when a failure occurs at the j^{th} node :

$$T_{ext} = [T_1, 0, ..., T_1, 0, ..., T_M]^T \tag{4.10}$$

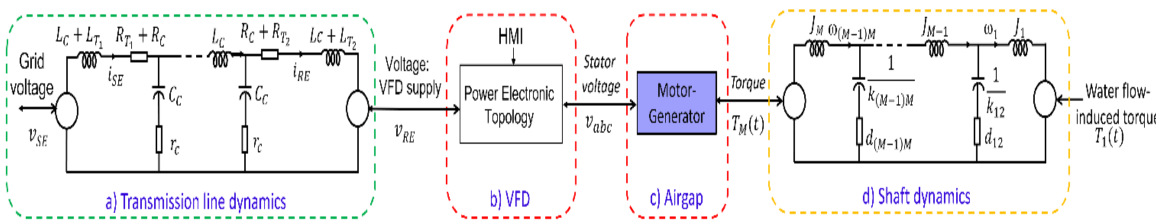

Figure 4. 3 An integrated electromechanical model of a PSH plant

4.4.3 VFD switching model

The cable receiving-end voltage usually supplies the VFD input rectifier, generating a DC-link voltage with an average value of $V_{DC} = 1.35V_{SE}$. For the sake of simplicity, it is assumed that the DC-link capacitor is large enough to decouple the dynamics of the grid and motor sides. The VFD model is modeled by its PWM generation unit. The PWM modulation unit generates a switching function that is multiplied by the DC-link voltage [158]. Regardless of the operation mode of the machine, voltage, and current quantities can be written in a generic form in a steady state, as shown in (4.11) and (4.12) [159] :

$$v_a(t) = \sum_{m_v=0}^{\infty} \sum_{n_v=0}^{\infty} V_{m_v,n_v} \cos\left(m_v\omega_k t \pm n_v\omega_0 t + \theta^v_{m_v,n_v}\right) \tag{4.11}$$

$$i_a(t) = \sum_{m_i=0}^{\infty} \sum_{n_i=0}^{\infty} I_{m_i,n_i} \cos\left(m_i\omega_k t \pm n_i\omega_0 t + \theta^i_{m_i,n_i}\right) \tag{4.12}$$

Where ω_k is an arbitrary frequency (for example the PWM carrier frequency) and ω_0 the fundamental frequency ; (m_v, n_v) and (m_i, n_i) are arbitrary integer sets ; $V_{m_v n_v}$ and $I_{m_i n_i}$ are the magnitudes of voltage and current. For a three-phase voltage system, $v_a(t)$ is the reference phase voltage. Therefore, voltages and currents on the two other phases are respectively phase shifted by $n_v = {}^{2\pi}\!/_{3}$ and $n_v = {}^{4\pi}\!/_{3}$

The arbitrary integer sets (m_v, n_v) and (m_i, n_i) depend on the inverter topology and its modulation strategy.

4.4.4 Motor airgap model

The motor airgap creates the power supply-induced torque components from the voltage supplied to the machine and the current requested by the machine to generate the needed torque in motoring mode. And they result from a combination of the back-electromagnetic forces (generator mode) created by the machine and the current flowing to its electrical load. The torque is calculated by (4.13). The principle of transforming the machine's voltages (4.11) and currents (4.12) is described in [159]. The integrated model of the PSH shaft system for the evaluation of torsional stresses is shown in Figure 4.3. The interaction of voltage and current components in the motor's airgap creates infinite electromagnetic torque harmonic components. The machine instantaneous airgap torque induced by the power supply is analyzed in the stationary and orthogonal $\alpha\beta$-coordinates for harmonic evaluation. It offers the advantage of analyzing the torque waveform as a complex quantity without cumbersome mathematical developments, while accurately tracking all relevant harmonics. The rotating dq-coordinates would require an infinite synchronization to all harmonic frequencies as well as complicated reverse transformations of the results back to the frequency domain. By replacing (4.11) and (4.12) in (4.13), the theoretical lines of the Campbell diagram are given in (4.14). The torque magnitudes and phase are given in (4.15) and (4.16). The torque equations are given in (4.17). Where ε_{n_v} and ε_{n_i} are $\in(-1,1)$. Only a few of the components in (4.17) are pertinent for a torsional analysis. In PWM VSI systems, the arbitrary frequency is the carrier frequency : $\omega_k=\omega_c$ which is usually in the range of 1.0 kHz or more. Certain combinations of (m_v,n_v) induce cancellation of voltage harmonics.

$$t_{eVFD}(t)=\frac{3}{2}\frac{P}{2}\left(\psi_\alpha(t).i_\beta(t)-\psi_\beta(t).i_\alpha(t)\right) \tag{4.13}$$

$$\omega_h=\left(m_i-\frac{\varepsilon_{n_i}}{\varepsilon_{n_v}}m_v\right)\omega_k\pm\left(n_i-\frac{\varepsilon_{n_i}}{\varepsilon_{n_v}}n_v\right)\omega_0 \tag{4.14}$$

$$T_{eh}=\varepsilon_{n_v}.\frac{3}{2}\frac{P}{2}\frac{V_{m_v,n_v}}{m_v\omega_k\pm n_v\omega_0}I_{m_i,n_i} \tag{4.15}$$

$$\theta_h=\theta^i_{m_i,n_i}\pm\frac{\varepsilon_{ni}}{\varepsilon_{nv}}\theta^v_{m_v,n_v} \tag{4.16}$$

Furthermore, depending on the VFD topology and its modulation strategies, certain combinations of (m_v,n_v) lead to the cancellation of certain voltage and current harmonics. The modulation strategy is therefore critical in ensuring that unwanted torque harmonics are cancelled, or their magnitudes are substantially low to threaten the endurance limits of shaft elements. The following section discusses the VFD topologies, and their modulation strategies utilized in PSH applications aiming to evaluate the torque stress they produce.

4.5 VFD topologies for PSH plants

4.5.1 General arrangements

The three types of system arrangements utilized in PSH applications are summarized in figure 4 with their respective ranges [160]-[161]. Layout 1, Figure 4.4(a), is used when plant capacity is below 25 MW. Layout 2, Figure 4.4(b) is for PSH plants below 100 MW. These two topologies use synchronous machines, whereas Layout 3, Figure 4.4(c), uses a doubly-fed induction machine. In such a system configuration, about 30% of the total power flows through the rotor, which enables a very high-output power production for the plant, usually 100–250 MW [162]. This chapter is limited to VFD topologies suitable for Layout 2 only, as they are the ones suitable for US applications [163].

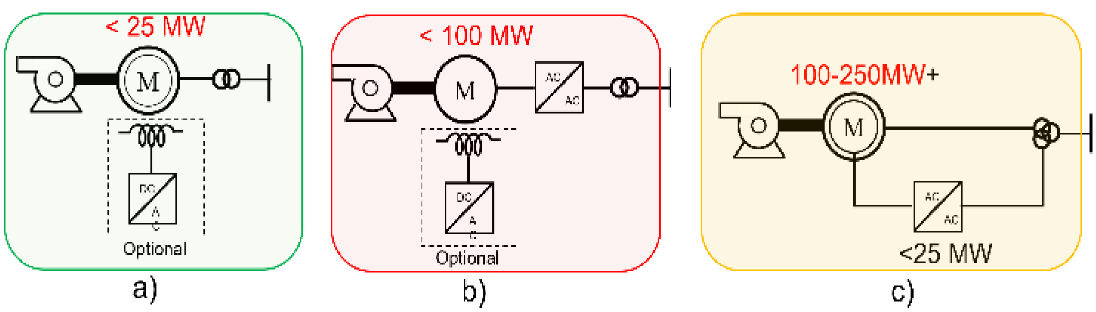

Figure 4. 4 : High-level Power system arrangements of PSH plant [3].

$$t_{eVFD}(t) = \sum_{m_v=0}^{\infty}\sum_{n_v=0}^{\infty}\sum_{m_i=0}^{\infty}\sum_{n_i=0}^{\infty}\left[\varepsilon_{n_v} * \frac{3}{2}\frac{P}{2}\frac{V_{m_v,n_v} I_{m_v,n_v}}{m_v\omega_k + n_v\omega_0}\right]\cos\left(\left(\left(m_i - \frac{\varepsilon_{n_i}}{\varepsilon_{n_v}}m_v\right)\omega_k \pm \left(n_i - \frac{\varepsilon_{n_i}}{\varepsilon_{n_v}}n_v\right)\omega_0\right)t + \left(\theta^{i}_{m_i,n_i} - \frac{\varepsilon_{n_i}}{\varepsilon_{n_v}}\theta^{v}_{m_v,n_v}\right)\right) \quad (17)$$

4.5.2 Investigated VFD topologies

There are numerous VFD topologies that can be utilized for Layout 2. Figure 4.5 shows two main high-level configurations with their respective power ranges. A three-phase machine supplied by a set of parallel connected identical power converters coupled through coupling inductances [Figure 4.5(a)]. And a multi-stator winding machine ; in this case, it is a twelve-phase synchronous machine supplied by identical power converters [Figure 4.5(b)]. In this case, the airgap torque is the sum of all individual torque generated by the converter supplying each three-phase stator windings [164]. The investigated families of back-to-back power converter topologies are shown in Figure 4.6. They include : 1) A two-level VSI topology, suitable for PSH applications up to 25MW) ; 2) A three-level NPC VSI suitable for power exceeding 30 MW, and the cascaded H-bridge multilevel VSI, for power exceeding 60 MW [165]-[166].

4.5.3 Effect of interleaving PWM Commands

Parallel connection of VFD uses coupling inductors, which convert VFD voltages to currents, which are added at the coupling point before flowing to the motor stator. The PWM commands can be synchronized or interleaved [167], [168]. Synchronized commands enable the system to behave like a large single VFD. Interleaved commands are phase-shifted by a pre-calculated angle. Let us assume there are k paralleled VSIs. Each converter $j \in \{1, 2, ...k\}$ generates a phase voltage $v_{a,j}(t)$. A regular asymmetric sampling PWM is utilized. The voltages are generated by comparing a sinewave with a frequency ω_0 to a triangle signal with a frequency ω_c. The triangle signal is phase shifted by $\theta_{c,j}$ with respect to the phase a reference sinewave.

$$\theta_{c,j} = (j-1)\frac{\pi}{k} \tag{4.18}$$

Each voltage harmonic of the j^{th} converter for a set of (m_v, n_v) has a magnitude $V_{m_v,n_v,j}$.

Thus, $v_{a,j}(t)$ is given in (4.19) :

$$v_{a,j}(t) = \sum_{m_v=0}^{\infty}\sum_{n_v=0}^{\infty} V_{m_v,n_v,j}\cos\left(x_{m_v,n_v,j}(t) + m_v\theta_{c,j}\right) \tag{4.19a}$$

$$x_{m_v,n_v,j}(t) = m_v\omega_k t \pm n_v\omega_0 t + \theta^{v}_{m_v,n_v} + \delta_{m_v,n_v} \tag{4.19b}$$

All components at $k\left(2m_i\right)\pm 1$ for all applicable n_i are canceled. All other harmonic components are reduced. Consequently, the resulting torsional stress will see a cancellation or drastic reduction on its corresponding harmonics [168]. Let's assume the coupling inductors have the same impedance. All DC-link voltages are equal. When paralleled, the only dominant current harmonics produced by the VFDs are the baseband and common-mode components with a rank multiple of $k(2m_i)$.

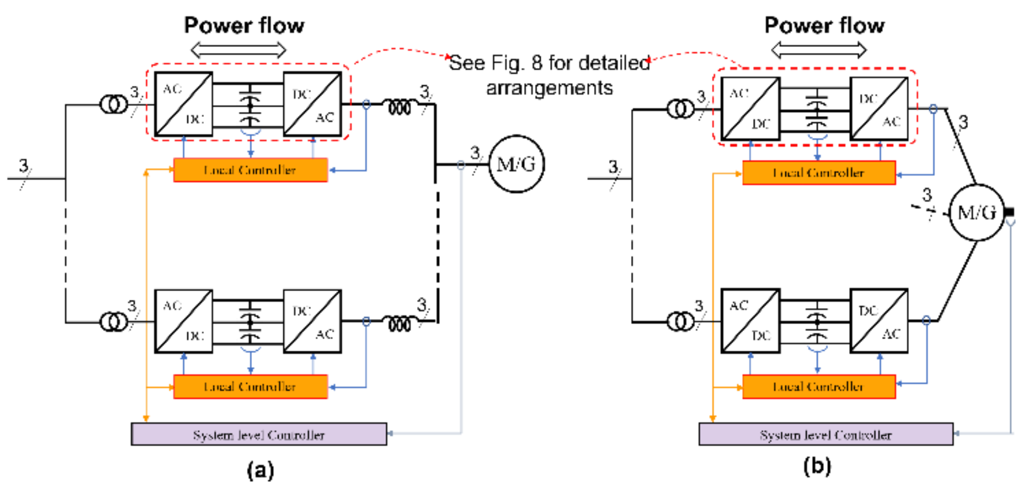

Figure 4. 5 : High-level system configurations of VFDs for PSH applications.

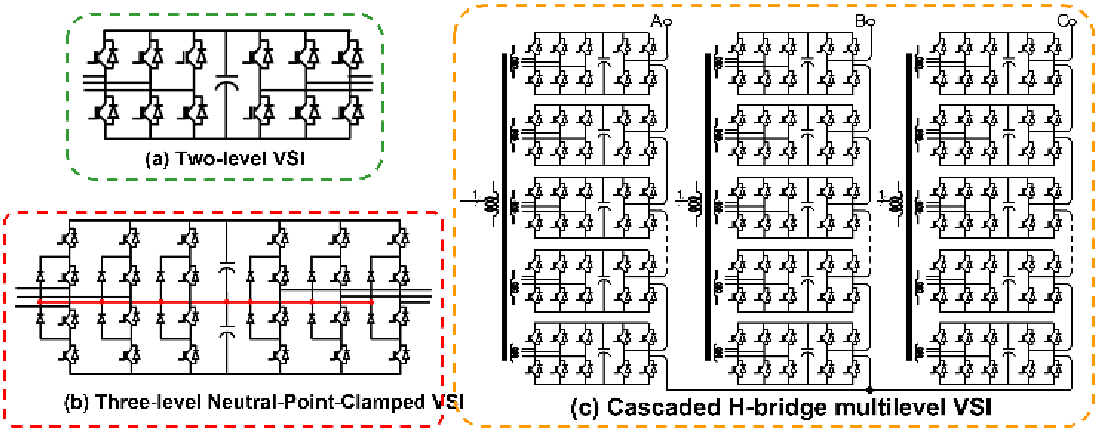

Figure 4. 6 : Detailed arrangements of VFDs for PSH applications up to 100 MW.

4.5.4 Effects of PWM commands to a multi-phase machine

Let us assume the AC machine has k sets of three-phase windings supplied by k PWM-VSIs, each converter $j \in \{1, 2, ...k\}$ generates a phase voltage $v_{a,j}(t)$. The electrical phase-shift angle between consecutive winding sets is (4.20a), [170]. The flux formed in the airgap is equivalent to the one produced by the k sets of voltages, with a phase shift shown in (20b). In that case, the voltage harmonic families are given in (4.21).

$$\theta_{e,j} = \frac{\pi}{3k}, \tag{4.21a}$$

$$\theta_{0,j} = (j-1)\frac{\pi}{3k} \tag{4.21b}$$

$$v_{a,j}(t) = \sum_{m_v=0}^{\infty} \sum_{n_v=0}^{\infty} V_{m_v,n_v,j} \cos\left(y_{m_v,n_v,j}(t) + n_v\theta_{0,j}\right) \tag{4.21c}$$

$$y_{m_v,n_v,j}(t) = m_v\omega_k t \pm n_v\omega_0 t + \theta^{v}_{m_v,n_v} + \delta_{m_v,n_v} \tag{4.21d}$$

The sum of the voltages induces a cancellation of all harmonic components formed when n_v is an odd multiple of 3k.

$$n_v = 3k(2l+1); \quad l \in \mathbb{N} \tag{4.22}$$

Moreover, only components with frequencies even multiple of 3k will have their magnitude multiplied by 3k.

$$n_v = 3k(2l); \quad l \in \mathbb{N}^* \tag{4.23}$$

All other harmonics will have magnitude smaller than *k*-times their individual harmonics, which reduce the torsional stresses.

4.6 PSH systems operation with failed cells power modules

4.6.1 Robustness and failed mode reconfigurations

4.6.1.1 System configuration with failed two-level or three-level NPC converters

So far, the analysis assumes all power modules are operating in normal mode. However, in case of failure, the location of torsional stresses in the frequency domain can significantly change, depending on how faults are handled. For example, if *k*-power modules are parallel connected, then a failure of ε-power modules which are subsequently disconnected from the operating system, will induce a shift of harmonics to be identical to the one from a $(k-\varepsilon)$-power module system. To interleave the PWM commands, the phase-shift-angle given in (18) shall be adjusted to $\theta_{c_{new},j}$:

$$\theta_{cnew,j} = (j-1)\frac{\pi}{k-\varepsilon}, \quad j \in \{1,\ldots,k-\in\}; \;\; \varepsilon \prec k \tag{4.24}$$

Figure 4.7 shows a system configuration with a failed and disconnected power module (for two-level and three-level NPC converters). The system level controller is responsible for the power part reconfiguration (i.e., order disconnection of failed the power module), adjustment of power module control parameters (e.g., reduced power generation), and calculation of new PWM phase-shift angles to interleave the PWM commands. Theoretically, for a given PWM strategy, all PWM-VSIs generate voltage harmonics located at identical frequencies ; only their magnitudes differ from one VSI topology to another, particularly when PWM commands are synchronized. Therefore, if a power module fails and is disconnected from the operating system, only the magnitude of the torsional stress will slightly increase. These statements are only valid for the two-level and the three-level NPC regenerative inverters.

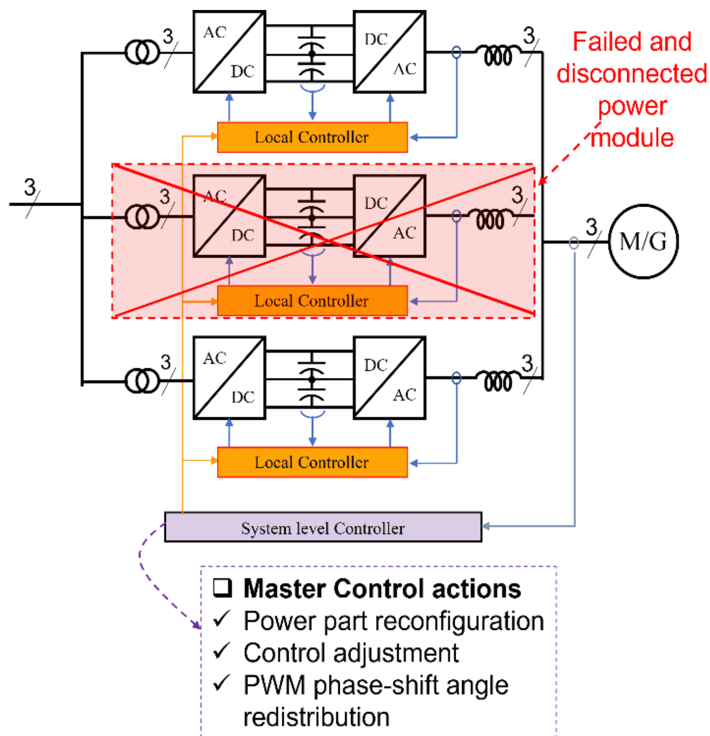

Figure 4. 7: System configuration with failed power module.

4.6.1.2. System configuration based on CHB-VSI with failed cells

The fault management of the cascaded H-bridge regenerative converter topology enables higher system availability than the other system architectures. Because of an increased number of power cells (H-bridges), there is no need to disconnect a complete power module in case of abnormal operation. The system can operate with failed H-bridge cells, where the PWM commands of a given three-phase system are adjusted through a neutral-shift method such that the VFD produces unbalanced line-to-neutral voltages. In contrast, the line-to-line voltages remain balanced, [171]-[172]. Figure 8 shows the system configuration with partially failed power modules but with completely bypassed H-bridge cells. The local controllers order any failed cell to be ignored by closing the output circuit breaker and disconnecting it from the system by opening the module input circuit breaker. Circuit breakers are not shown for the sake of simplicity. Once the power stage is reconfigured, the phase voltage imbalance is calculated, new voltage phase-shift angles are determined, the new homopolar component is computed. and the new PWM references are generated to ensure that balanced line-to-line voltages are generated at the output of the unhealthy power module [172]-[177].

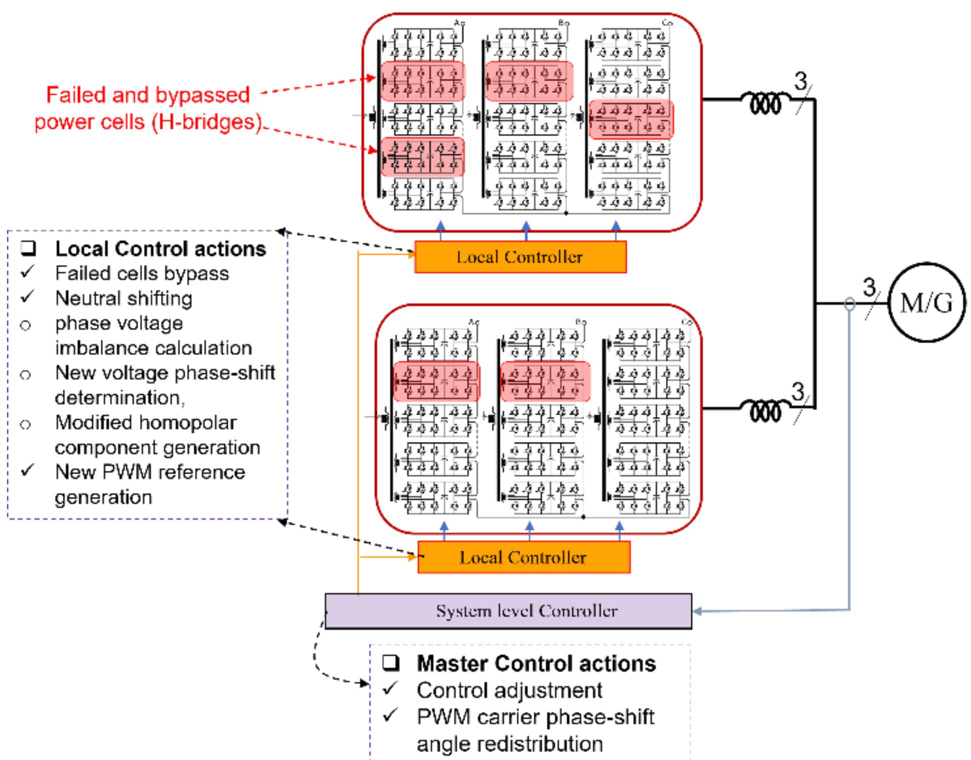

Figure 4. 8: System configuration with partially failed power modules but with failed and bypassed H-bridge cells.

Finally, the master controller adjusts the current references that each power module should generate and calculates the new carrier phase-shift angles for each power module if needed

4.6.2 Harmonic analysis in CHB-VSI system with faulty cells

Let's consider a CHB PWM-VSI system with k_i-series connected H-bridge power cells in the phase i of a three-phase system. Each cell is supplied by a dc voltage $v_{dc,ij} = v_{dc}$ such that $v_{dc} = 1.pu$ for healthy cells and $v_{dc} = 0.pu$ for failed cells. In balanced conditions, the phase-shift between phase voltages is : $\theta_{0,i} = (i-1)\frac{2\pi}{3}$, $i \in \{a=1, b=2, c=3\}$. In that case, the total perceived DC-link voltage per phase is given by :

$$V_{dc,i} = k_i v_{dc} \tag{3.25}$$

Consequently, in normal mode operation when all k_i-power modules are operational on phase i the reference voltage with a frequency fundamental ω_0 can be written as :

$$v^*_{r,i}(t) = m_i V_{dc} \sin\left(\omega_0 t - \theta_{0,i}\right) \tag{3.26}$$

Where $m_i \in [0,1]$ is the PWM modulation index applied to phase i. The maximum achievable phase voltage resulting from the modulator in normal mode is given by :

$$\max_{i \in P}\left(v_i(t)\right) = v_i(x^*) = V_{\max,i}, \quad \forall x^* \in \arg\max\left(\underset{i \in \mathrm{P}}{v_i(t)}\right) \tag{4.27a}$$

$$V_{\max,i} = \frac{\sqrt{3}}{2} V_{dc,i} \tag{4.27b}$$

Let's assume there are ε_i-failed H-bridge cells on phase i, such that $\varepsilon_i < k_i$. In that case, the perceived maximum voltage in the affected inverter phase is given in (4.28).

$$V_{\max,i}^{F} = \left(k_i - \in_i\right)\frac{\sqrt{3}}{2}v_{dc} \tag{4.28}$$

When voltages at the motor terminals are unbalanced, it leads to unequal power distribution across the motor phases. This imbalance causes higher current flow in the phase with higher voltage, resulting in several issues, such as high current imbalance, pulsating torque, and mechanical Stresses. As a result, evaluating VFD-induced torsional stresses under unbalanced conditions (without and with the neutral-shift approach) is critical for the completeness of the design because the locations of harmonics are unknown.

4.6.2.1. Harmonic analysis in normal mode

In normal (ideal) operating mode for both linear and overmodulation regions, the analytical expression of the CHB-VSI LN-voltage $v_i^N(t)$ can be written as follows :

$$v_i^N(t) = k * V_{0,1}\cos\left[\omega_0 t - \left(i-1\right)\frac{2\pi}{3}\right] \tag{4.29a}$$

$$+k\sum_{n_v=2}^{\infty} V_{0,2n_v-1}\cos\left[\left(2n_v-1\right)\left(\omega_0 t - \left(i-1\right)\frac{2\pi}{3}\right)\right] \tag{4.29b}$$

$$+k\sum_{m_v=1}^{\infty} V_{(2m_v-1),0}\cos\left[\left(2m_v-1\right)\left(\omega_c t - \theta_c\right)\right] \tag{4.29c}$$

$$+\sum_{m_v=1}^{\infty}\sum_{\substack{n_v=-\infty \\ n_v\neq 0}}^{\infty} V_{(2m_v-1),2n_v}\cos\left[\begin{array}{c}\left(2m_v-1\right)\left(\omega_c t - \theta_c\right) + \\ 2n_v\left(\omega_0 t - \left(i-1\right)\frac{2\pi}{3}\right)\end{array}\right] \tag{4.29d}$$

$$+\sum_{m_v=1}^{\infty}\sum_{n_v=-\infty}^{\infty} V_{2m_v,2n_v+1}\cos\left[\begin{array}{c}2m_v\left(\omega_c t - \theta_c\right) + \\ \left(2n_v+1\right)\left(\omega_0 t - \left(i-1\right)\frac{2\pi}{3}\right)\end{array}\right] \tag{4.29e}$$

$$\begin{bmatrix} u_{ab} \\ u_{bc} \\ u_{ca} \end{bmatrix} = \begin{bmatrix} 1 & -1 & 0 \\ 0 & 1 & -1 \\ -1 & 0 & 1 \end{bmatrix} . \begin{bmatrix} v_a^N \\ v_b^N \\ v_c^N \end{bmatrix} \tag{4.30a}$$

$$v_a^N = v_1^N \ ; \ v_b^N = v_2^N \ ; \ v_c^N = v_3^N \tag{4.30b}$$

The analytical expression of the LL-Voltage $u_{ab}^N(t)$, $u_{bc}^N(t)$ and $u_{ca}^N(t)$ are given in (4.31), (4.30), and (4.31), respectively.

$$v_{ab}^N(t) = k\sqrt{3} * V_{0,1} \cos\left[\omega_0 t - \frac{\pi}{6}\right] \tag{4.31a}$$

$$+k\sqrt{3}\sum_{n_v=2}^{\infty} V_{0,2n_v-1} \cos\left[(2n_v - 1)\left(\omega_0 t - \frac{\pi}{6}\right)\right] \tag{4.31b}$$

$$+\sqrt{3}\sum_{m_v=1}^{\infty}\sum_{\substack{n_v=-\infty \\ n_v\neq 0}}^{\infty} V_{(2m_v-1),2n_v} \cos\left[\begin{matrix}(2m_v-1)(\omega_c t - \theta_c) + \\ 2n_v\left(\omega_0 t - \frac{\pi}{6}\right)\end{matrix}\right] \tag{4.31c}$$

$$+\sqrt{3}\sum_{m_v=1}^{\infty}\sum_{n_v=-\infty}^{\infty} V_{2m_v,2n_v+1} \cos\left[\begin{matrix}2m_v(\omega_c t - \theta_c) + \\ (2n_v+1)\left(\omega_0 t - \frac{\pi}{6}\right)\end{matrix}\right] \tag{4.31d}$$

$$v_{bc}^N(t) = k\sqrt{3} * V_{0,1} \cos\left[\omega_0 t - \frac{\pi}{2}\right] \tag{4.32a}$$

$$+k\sqrt{3}\sum_{n_v=2}^{\infty} V_{0,2n_v-1} \cos\left[(2n_v - 1)\left(\omega_0 t - \frac{\pi}{2}\right)\right] \tag{4.32b}$$

$$+\sqrt{3}\sum_{m_v=1}^{\infty}\sum_{\substack{n_v=-\infty \\ n_v\neq 0}}^{\infty} V_{(2m_v-1),2n_v} \cos\left[\begin{matrix}(2m_v-1)(\omega_c t - \theta_c) + \\ 2n_v\left(\omega_0 t - \frac{\pi}{2}\right)\end{matrix}\right] \tag{4.32c}$$

$$+\sqrt{3}\sum_{m_v=1}^{\infty}\sum_{n_v=-\infty}^{\infty} V_{2m_v,2n_v+1} \cos\left[\begin{matrix}2m_v(\omega_c t - \theta_c) + \\ (2n_v+1)\left(\omega_0 t - \frac{\pi}{2}\right)\end{matrix}\right] \tag{4.32d}$$

$$v_{ca}^N(t) = k\sqrt{3} * V_{0,1} \cos\left[\omega_0 t + \frac{5\pi}{6}\right] \tag{4.33a}$$

$$+k\sqrt{3}\sum_{n_v=2}^{\infty} V_{0,2n_v-1} \cos\left[(2n_v - 1)\left(\omega_0 t + \frac{5\pi}{6}\right)\right] \tag{4.33b}$$

$$+\sqrt{3}\sum_{m_v=1}^{\infty}\sum_{\substack{n_v=-\infty \\ n_v\neq 0}}^{\infty} V_{(2m_v-1),2n_v}\cos\begin{bmatrix}(2m_v-1)(\omega_c t-\theta_c)+ \\ 2n_v\left(\omega_0 t+\dfrac{5\pi}{6}\right)\end{bmatrix} \tag{4.33c}$$

$$+\sqrt{3}\sum_{m_v=1}^{\infty}\sum_{n_v=-\infty}^{\infty} V_{2m_v,2n_v+1}\cos\begin{bmatrix}2m_v(\omega_c t-\theta_c)+ \\ (2n_v+1)\left(\omega_0 t+\dfrac{5\pi}{6}\right)\end{bmatrix} \tag{4.33d}$$

Figures 4.9(a) and 4.9(b), respectively illustrates the LN- and LL-voltage harmonic spectrum produced while the converter is in normal (ideal) mode. Since identical components can be found in phase *B*, only voltage harmonics from phase *A* are shown in Figure 4.10. Three types of harmonics are depicted in Figure 10(a) : (i) Baseband components (peru and blue lines) that are proportional to fundamental frequency f_0, (ii) Carrierband components (red lines) that are proportional to the PWM frequency f_c, and (iii) Sideband components (nevy, green and pink lines) that are centered on the carrier frequency are examples of these components. The carrier band harmonics given in (3.30c) are not present in the line-to-line voltages since these components are identical across all phases as shown in figure 10b. In addition, triplen baseband and sideband harmonics are cancelled between the phase leg, as shown in Figure 4.10(b). This conclusion is invalid when a CHB-VSI is under failure mode, i.e., when operating with failed H-bridge cells as discussed in the next sequel.

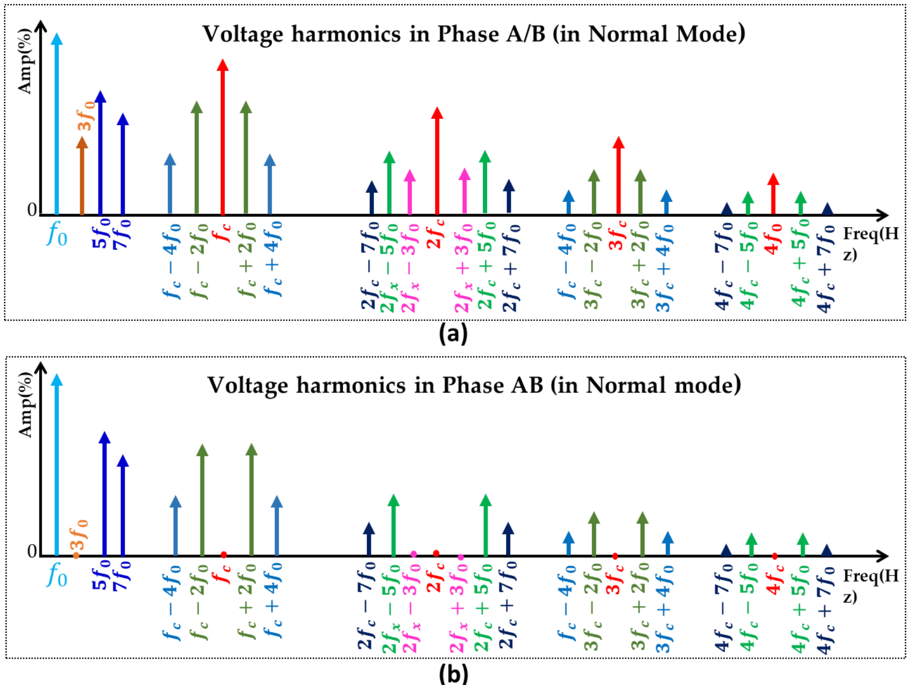

Figure 4. 9 : Harmonic analylis in Balanced conditions : Voltage harmonic in phase A ; (b) : Voltage harmonic in phase AB.

4.6.2.2. Harmonic analysis in failure mode

With the three PWM reference voltages shifted by 120°, an analytical CHB-VSI LN-voltage harmonic expressions in failure mode are given by :

$$v_i^F(t) = k * V_{0,1}(M_i)\cos\left[\omega_0 t - (i-1)\frac{2\pi}{3}\right] \tag{4.34a}$$

$$+K_i \sum_{n_v=2}^{\infty} V_{0,2n_v-1}(M_i)\cos\left[(2n_v-1)\left(\omega_0 t - (i-1)\frac{2\pi}{3}\right)\right] \tag{4.34b}$$

$$+K_i \sum_{m_v=1}^{\infty} V_{(2m_v-1),0}(M_i)\cos\left[(2m_v-1)(\omega_c t - \theta_c)\right] \tag{4.34c}$$

$$+\sum_{m_v=1}^{\infty} \sum_{\substack{n_v=-\infty \\ n_v \neq 0}}^{\infty} V_{(2m_v-1),2n_v}(K_i, M_i)\cos\left[\begin{array}{c}(2m_v-1)(\omega_c t - \theta_c) + \\ 2n_v\left(\omega_0 t - (i-1)\dfrac{2\pi}{3}\right)\end{array}\right] \tag{4.34d}$$

$$+\sum_{m_v=1}^{\infty} \sum_{n_v=-\infty}^{\infty} V_{2m_v,2n_v+1}(K_i, M_i)\cos\left[\begin{array}{c}2m_v(\omega_c t - \theta_c) + \\ (2n_v+1)\left(\omega_0 t - (i-1)\dfrac{2\pi}{3}\right)\end{array}\right] \tag{4.34e}$$

$$K_i = \left(k_i - \in_i\right) \tag{4.35}$$

k_i is the total number of H-bridge cells per-phase in the normal (balanced) mode, K_i : is the total number of healthy cells still present in each phase under failure mode, and ε_i : is the total number of failed and bypass cells per-phase. The frequency of the harmonic components in failure mode is solely dependent on the constant integers m_v and n_v, just like in normal mode. However, the magnitudes of these harmonics are dependent on the constant k_i, with respect of modulation index M_i applied in each PWM reference voltage. A harmonic analysis of a CHB-VSI operation with failed cells is discussed in Figure 4.10, where it is assumed that the inverter is operating with ε_i -failed cells in phase *B* and there is no failure in phases *A* and *C*. In this case, the spectrum of line voltage V_{AC} will remain unchanged and be similar to that under normal (balanced) conditions as shown in Figure 4.9b. Only the line voltages V_{AB} and V_{BC} spectra are impacted, and they theoretically have the same harmonic distribution. In both failure and normal modes, the CHB-VSI theoretically produces per-phase voltage harmonics at the same frequencies, while their amplitudes may vary, as can be shown in Figure 4.10(a). For instance, the magnitudes of the carrier-band harmonics are not the same all the phases. Their magnitude in phases *A* and *B* are given by the expressions $k_i * V_{0,2n_v-1}$ and $k_i * V_{(2m_v-1),0}(M_i)$, respectively, following (4.30c) and (4.35c). As a result, carrierband harmonics in failure mode cannot be eliminated by differentiating the LL voltages, as illustrated in Figure 4.10b. Similarly, it can be also observed that in LL voltage spectrum, the triplen baseband (e.g., $3f_0$) and sideband (e.g., $2f_c \pm 3f_0$) are not eliminated either. A failure of H-bridge cell introduces more voltage harmonic distortion, increasing current ripple and pulsating torque components, which in turn may raise torsional vibration and mechanical stresses.

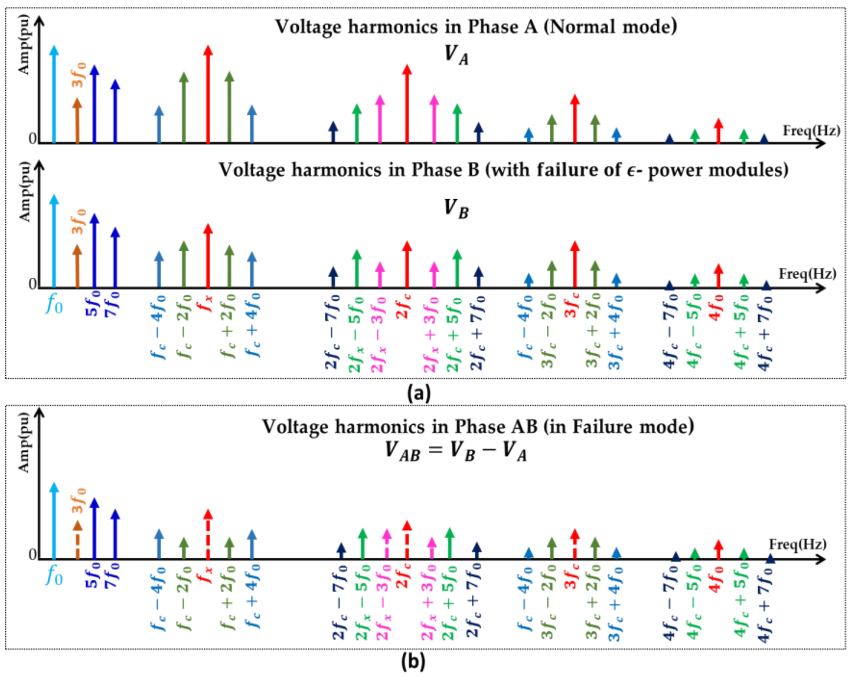

Figure 4. 10 : An harmonic analysis under unbalanced conditions. (a) : Voltage harmonic in phase A ; (b) : Voltage harmonic in phase AB.

4.6.2.3. A limitation of the existing fault-tolerant control methods for CHB-VSI operation with failed cells

It is feasible to balance line voltages even in situations where the phase voltage remains unbalanced, through the use of appropriate fault-tolerant control methods. This can be achieved by modifying the inverter reference voltage phase angles. Such an approach offers a reliable and effective means of achieving optimal voltage balance. However, the CHB-VSI output voltage and current spectra still need to be improved even by adequately adjusting the inverter reference voltage phase angles. For instance, it has been demonstrated in the previous subsection that all carrier band, triple baseband, and sideband harmonics in failure mode do not cancel between the phase legs as in normal mode, resulting in a poorer LL-voltage harmonic spectrum. The motor impedance converts these undesirables' voltage harmonics to current harmonics. And when combined, generated voltage and current harmonics will produce undesirable torque components that may result in harmonic pollution and even harmonic resonance. Evaluation, then cancellation of these undesired harmonic components, is essential to reduce torsional stresses and maintain a safe and stable system operation of a PSH plant.

4.7 Torsional Stresses Induced By Investigated Vfds

The shaft connected to the electrical machine in all VFD configurations is the same for all investigated cases. This assumption will provide an identical basis for comparison of torsional stresses generated by all investigated VFDs. In that case, torsional stress components are identical to the torque components relative to their magnitudes.

4.7.1. Electrical harmonic and their induced torsional stresses

4.7.1.1 Basic considerations

The generic torque equations provided from (4.9) to (4.15) are used to evaluate frequencies and magnitudes of torsional stress components for a given VFD. Equation (4.14) shows all families of harmonic frequencies which might have relevant magnitudes. They solely depend on the integers m_v and n_v. The combination of these integers depends on the VFD topology, the type of PWM strategy, and the selected sampling method [178]. The most crucial step for practicing engineers is to determine the appropriate mix of

(m_v, n_v) for each VFD topology and the corresponding PWM strategies based on the final combination of the drive system. For example, developments for a parallel connection of VFDs with synchronized or interleaved PWM signals are provided, as well as multi-three-phase machines, as discussed in the earlier section.

4.7.1.2. Torsional stresses induced by electrical harmonics.

The following torsional stresses (4.37)-(4.39) and their sources of electrical (voltage and current) harmonic families are found in all investigated VFDs. The asymmetrical regular sampled PWM method, with double-edge triangular carriers, is analyzed because this method produces superior harmonic quality and is the most used in high-power VFDs, and carriers are in phase for multilevel inverters [176].

a. Torsional stresses from electrical fundamental and baseband harmonics :

$$t_{e_{0,6n}}(t) = T_{eDC} + \sum_{n=0}^{\infty} T_{e_{0,6n}} \cos\left(6n\omega_0 t\right) \tag{4.36}$$

a. Torsional stresses from sidebands around even multiple of carrier frequency of electrical harmonics :

$$t_{e_{2m,\pm 6n}}(t) = \sum_{m=1}^{\infty}\sum_{n=0}^{\infty} T_{e_{2m,6n}} \cos\left(2m\omega_c t \pm 6n\omega_0 t\right) \tag{4.37}$$

b. Torsional stresses from sidebands around odd multiple of carrier frequency of electrical harmonics :

$$t_{e_{2m,\pm 2n}}(t) = \sum_{m=1}^{\infty}\sum_{\substack{n=-\infty \\ (n\neq 0)}}^{\infty} T_{e_{2m,2n-1}} \cos\left[\left(2m-1\right)\omega_c t \pm \left(2n-1\right)\omega_0 t\right] \tag{4.38}$$

Table 4. 1 Families of VFD-induced torque harmonics.

Fundamental and baseband harmonics				
$(\mathbf{m}, n)$	**Voltage/ Current**	**Torque**	**2x Interleaved**	**2x three-phase systems**
$(0,1)$	ω_0	0	0	0
$(0,5)$	$5\omega_0$	$6\omega_0$	$6\omega_0$	Cancelled
$(0,7)$	$7\omega_0$			
$(0,11)$	$11\omega_0$	$12\omega_0$	$12\omega_0$	$12\omega_0$
$(0,13)$	$13\omega_0$			
Carrier band and sideband harmonics around odd multiple of carrier frequency				
$(1,0)$	ω_c	None	None	
$(1,2)$	$\omega_c \pm 2\omega_0$	$\omega_c \pm 3\omega_0$	$\omega_c \pm 3\omega_0$	$\omega_c \pm 3\omega_0$
$(1,4)$	$\omega_c \pm 4\omega_0$			
$(1,6)$	$\omega_c \pm 6\omega_0$	None	None	None
$(1,8)$	$\omega_c \pm 8\omega_0$	$\omega_c \pm 9\omega_0$	$\omega_c \pm 3\omega_0$	$\omega_c \pm 3\omega_0$
$(1,10)$	$\omega_c \pm 10\omega_0$			
Carrier band and sideband harmonics around even multiple of carrier frequency				
$(2,0)$	None	None	None	
$(2,1)$	$2\omega_c \pm \omega_0$	$2\omega_c$	Cancelled	$2\omega_c$
$(2,3)$	$2\omega_c \pm 3\omega_0$	None	None	
$(2,5)$	$2\omega_c \pm 5\omega_0$	$2\omega_c \pm 6\omega_0$	Cancelled	Cancelled
$(2,7)$	$2\omega_c \pm 7\omega_0$			
$(2,9)$	$2\omega_c \pm 9\omega_0$	None		
$(2,11)$	$2\omega_c \pm 11\omega_0$	$2\omega_c \pm 12$	Cancelled	$2\omega_c \pm 12$
$(2,13)$	$2\omega_c \pm 13\omega_0$			

4.8. Validations by numerical simulations

4.8.1. System setup and validation

A three-level two-level, three-level NPC and seven-level CHB VSI have been simulated by supplying a 30 MVA induction machine. Only the steady state is of interest for harmonic analysis. The asymmetrical regular sampled PWM method has been implemented with two vertically phase-shifted double-edge triangular carriers for the NPC. The two-level inverter has one carrier signal. The carrier frequency is chosen at a relatively low value for validation purposes, $f_c = 1kHz$. For each configuration, two identical VFDs are parallel connected through a set of three-phase coupling inductances of 3 *mH*. The PWM commands of both modules are first synchronized, then interleaved with a phase $\theta_c = \frac{\pi}{2}$ according to (4.18). The system is simulated for fundamental frequencies, f_0, from 10 Hz to the nominal frequency of 65 Hz, with a step of 5 Hz. Then, the machine's voltages, currents, and torque are extracted in the time-domain for analysis. Since the chapter focuses exclusively on analyzing and discussing the steady-state performances of PSH-VSI systems, simulation results are collected to ensure an accurate harmonic analysis in the frequency domain until each system attains its steady state. Also, the effects of system controllers (Such as PI, and PID) are not investigated. They have a minor influence on this type of analysis because they mainly act on system transient dynamics, damping transient oscillation resulting from the system dynamic changes. An analysis of motor voltage, current, and torque harmonics under normal, failure and corrected modes is also conducted for the specific case of CHB-VSI topology. A corrected operating mode of the system is the operation of the CHB-VSI system with failed cells modulated with the neutral-shift-based PWM method developed in [41], [47]-[54]. The results are post-processed by calculating their Fast Fourier Transform (FFT). The harmonic frequencies are extracted, and dominant components are identified and compared to the theoretical predictions. The time domain torsional stress is reconstructed based on dominant components only. The torsional stress is calculated, assuming the shaft has the same mechanical parameters. Finally, the locations of all the simulated torsional stresses of all operating points are laid over to the theoretical lines of their corresponding Campbell diagrams. This interference diagram helps to predict which operating point may induce threatening torsional stress for each system, potentially leading to a reduced lifetime of mechanical components.

4.8.2. Simulation results and Discussions

More than 75 operating points have been simulated. The detailed results of two representative cases, where $f_c = 1kHz$ and $f_0 = 45Hz$ are discussed for three types of converters. The remaining results are summarized in the respective Campbell diagrams. Figure 4.11 shows the motor voltages, currents, and torsional stresses for synchronized [Figure 4.11(a)], interleaved PWM commands of a parallel connection [Figure 4.11(b)], and of the three investigated VSI [Figure 4.11(c)]. In Figures 4.12 and 4.13, both time and frequency domain results are shown for each state variable. Precise locations of their respective torsional stresses are shown in Figure 4.14. The frequencies are consistent with the theoretical results shown in Table 4.1, and in (4.9) and (4.12). The spectra of the torsional stress over the full operating speed range of the investigated VFDs under synchronized and interleaved PWM methods are shown in Figure 4.15 and Figure 4.16, respectively. As indicated in Section IV.C, classes of harmonics that are cancelled are sideband around even multiple of the carrier frequency (2,000 Hz). This is valid for all the investigated converters. The interference diagrams for each of the systems are shown in

Figure 4.17 in the form of Campbell diagrams. The red dots show the location of torque components for synchronized PWM commands, while the greens show the one for the interleave commands. As discussed in Section IV.C, no green dot appears on sideband lines around odd multiple of the carrier frequency.

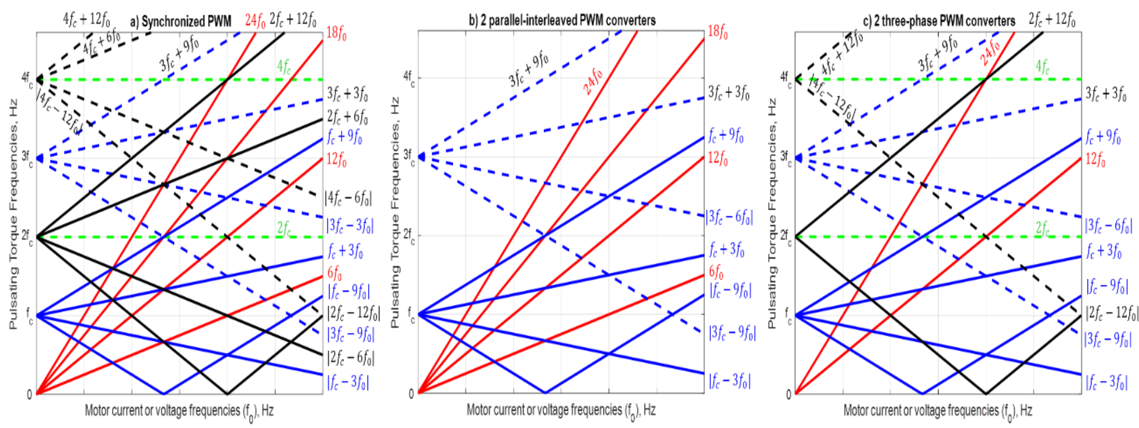

Figure 4. 11 : Campbell diagrams of VFDs with (a) synchronized PWM commands ; (b) parallel-interleaved PWM commands, and (c) two three-phase systems supplied by synchronized PWM commands.

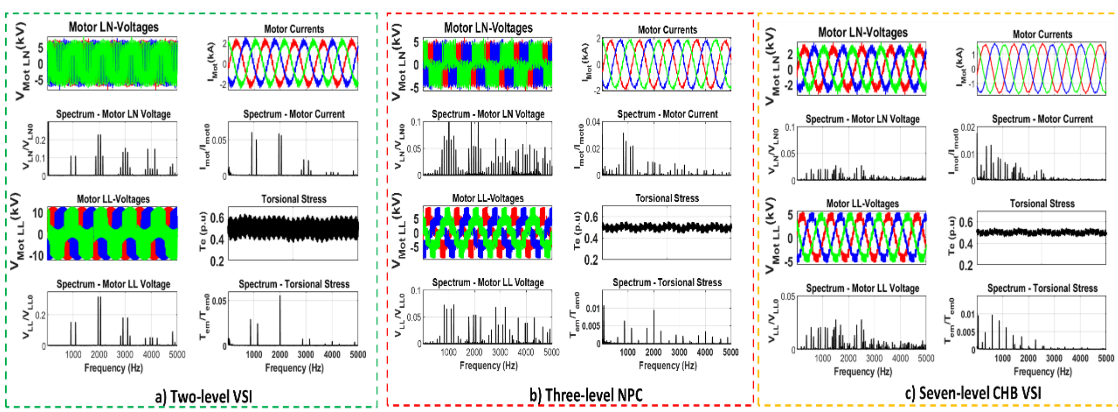

Figure 4. 12 : Simulations result of parallel VSIs with synchronized PWM ; $f_c = 1\text{kHz}$; $f_0 = 45$ Hz.

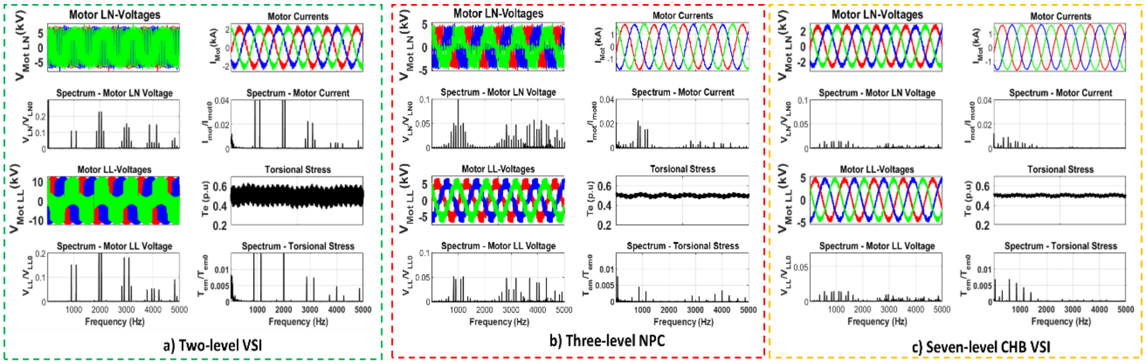

Figure 4. 13 : Simulations result of parallel VSIs with $\theta_c = \pi/2$ interleaved PWM ;$f_c = 1\text{kHz}$; $f_0 = 45$ Hz.

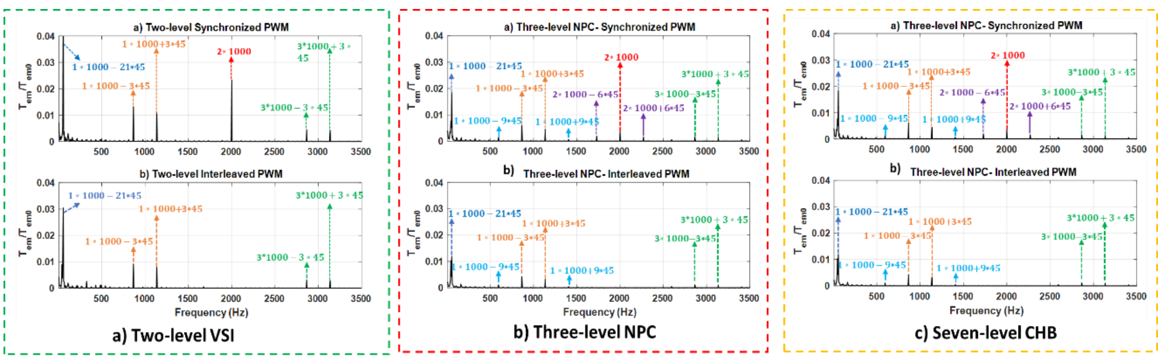

Figure 4. 14 : Precise location of torsional stresses for both synchronized and $\theta_c = \pi/2$ interleaved PWM different VSIs.

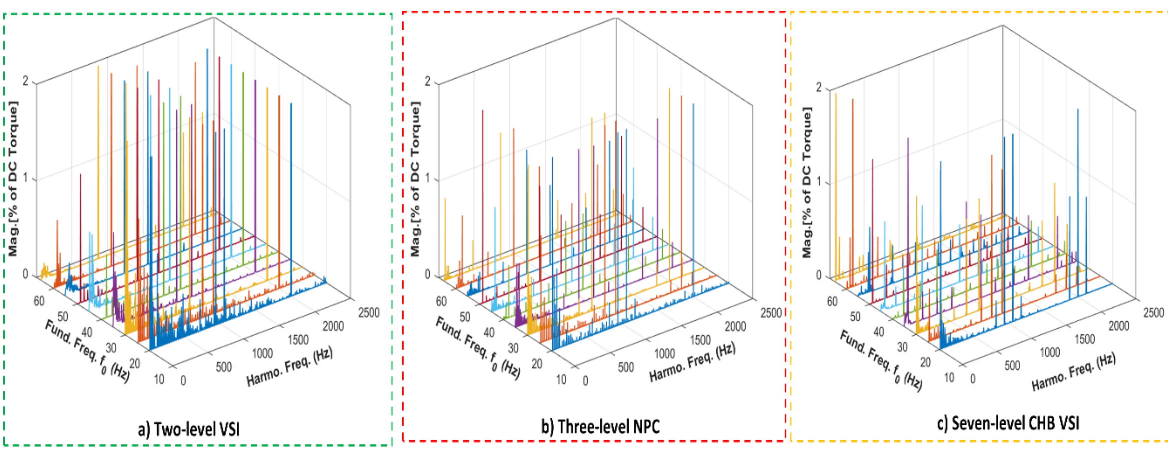

Figure 4. 15 : Simulation results with synchronized PWM ; $f_c = 1kHz$; $f_0 = 45Hz$.

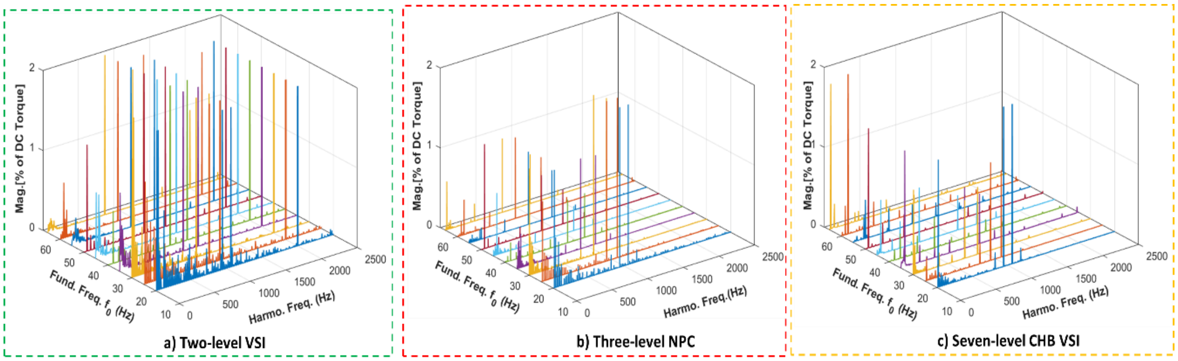

Figure 4. 16 : Simulation results with with $\theta_c = \pi/2$ interleaved PWM ; $f_c = 1kHz$; $f_0 = 45Hz$.

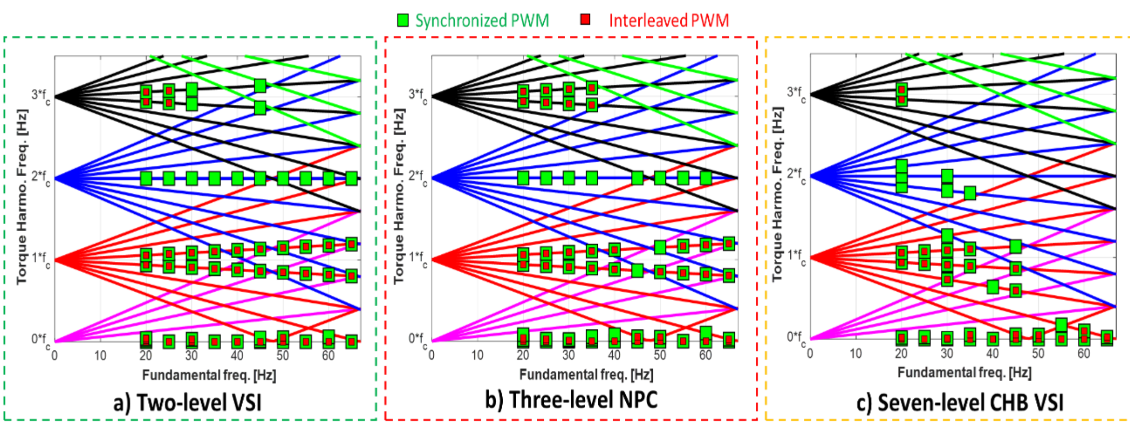

Figure 4. 17 : Generated Campbell diagrams of each investigated VSI topologies.

4.8.3. Simulation results from a CHB-VSI system with failed cells

The simulations were performed on a three-phase, nine-cell CHB-VSI system (three cells in each phase), where two faulty and bypassed power cells were placed at phase A. The gating signals for power switches are produced using the conventional phase disposition (PD-PWM) control method in both the failure operation (without the neutral shift method) and the corrected mode (with the neutral shift method). The selected The results in normal mode are shown in Figure 4.18(a) on the left, the results in failure mode are shown in Figure 4.18(b), and the results in corrected mode are shown in Figure 4.18(c) on the right. In normal mode, balanced voltage and currents are applied at the motor terminal. When two power cells fail, the voltage waveform V_A drops by two levels and unwanted harmonic distortions are introduced in both motor phase and line voltages. The resulting unbalanced and distorted motor currents, as a result, cause torque pulsation, which may increase vibration and mechanical stress. The neutral shift-based control method is introduced in corrected mode to maximize and balance the line voltages. In this condition, the phase angles of the voltages have been adjusted so that inverter phase A is displaced from phase B and from phase C by 140.4°. This adjustment has successfully rebalanced the motor line voltages and improved the current and torque waveforms [Figure 18(c)] compared to the failure mode [Figure 18(b)]. However, it can be observed that the neutral-shift method did not eliminate the undesirable harmonics that the failure introduced. Figure 4.19 shows a zoom on the CHB-VSI-induced torsional stresses in normal mode, failure mode, and corrected mode. It is observed that, the magnitudes of some low-order harmonics in normal mode [Figure 4.19(a)] have been seen to significantly rise in failure mode [Figure 4.19(b)].

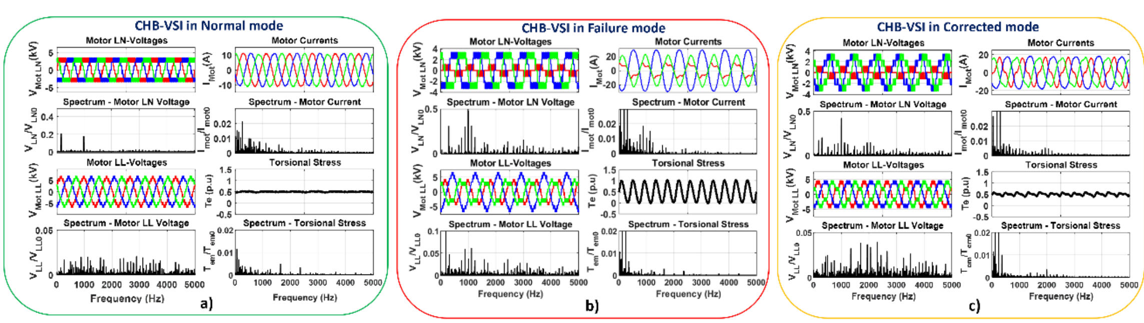

Figure 4. 18 : Simulation results a CHB-VSI at different operating mode with ; $v_a = [0\ 0\ 1]$; $v_b = [1\ 1\ 1]$ and $v_c = [1\ 1\ 1]$. (a): CHB-VSI in normal mode; (b) CHB-VSI in failure mode; (c): CHB-VSI in corrected mode

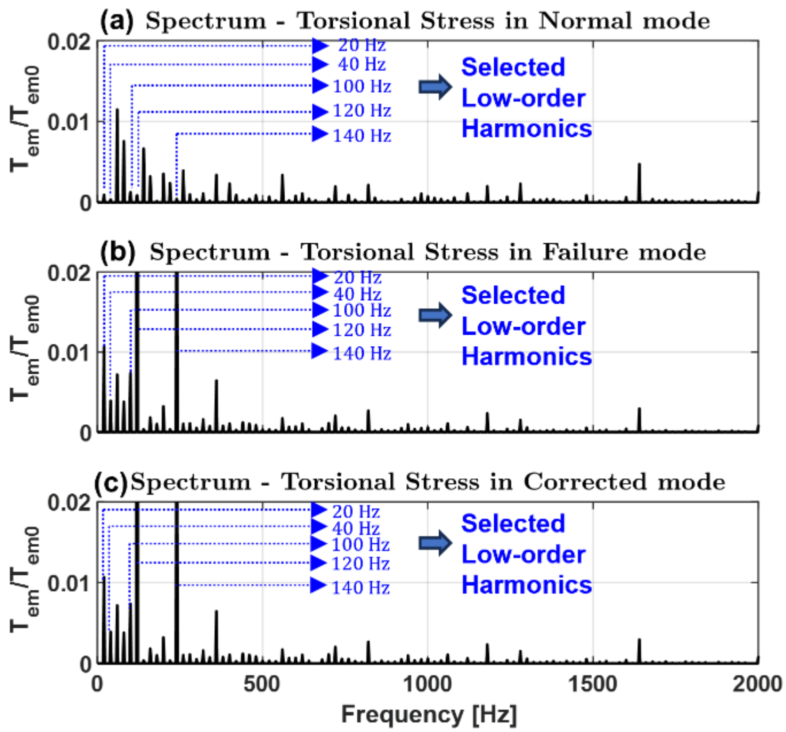

Figure 4. 19 : Zoom in CHB-VSI induced torsional stresses (a) Normal mode ; (b) Failure mode ; (c) Corrected mode.

These unwanted harmonics are also present in corrected mode, as shown in [Figure 4.19(c)], at the same frequency positions. This result shows that, it is crucial for the completeness of the design to evaluate the type of pulsating torque components the CHB-VSI system generates in the motor's airgap under unbalanced conditions, even controlled by a given fault-tolerant control technique. Such an analysis is beneficial to track and quantify the VFD-induced harmonics in order to ensure the integrity of the system over the operational envelopsimulation results are discussed in Figure 4.18.

4.8.4. HYBRID EXPERIMENTAL-NUMERICAL RESULTS AND DISCUSSIONS

Hybrid experimental–numerical real-time simulations are conducted to verify the accuracy and consistency of the suggested theoretical developments. This type of validation involves combining real-time physical experiments with numerical simulation to analyze the behavior of the PSH system model. Voltage measurements from a reduced-scaled lab prototype with a 3-level NPC and 7-level CHB were used to supply a numerical induction motor model. A Simulink real-time target PC equipped with a DAQ board PCI 6229 was used to connect each VFD power stage to the numerical simulation. This enables data exchange between the physical (real/analogical) and numerical/digital system model parts. Examples of experimental synchronized voltage waveforms used for the hybrid experimental–numerical validations are shown in Figures 4.20 and 4.21. Sample hybrid experimental-numerical results are summarized in Figure 4.22a-b, where motor voltage, current, and torque waveforms and their corresponding spectra are provided when supplied by collected 3-level NPC and 7-level CHB voltage measurements.

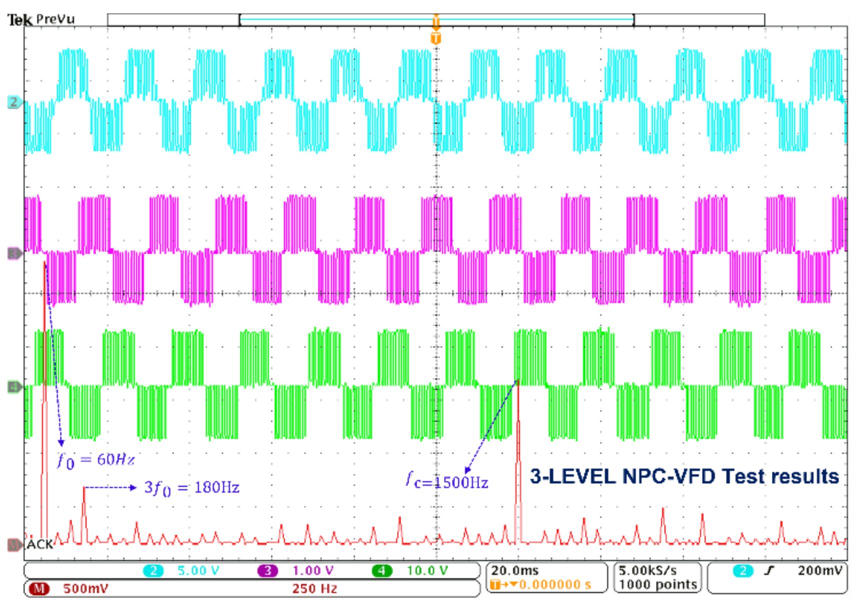

Figure 4. 20 : Synchronized switched waveforms obtained from a single 3-level NPC VFD ; $f_c = 1.5kHz$; $f_0 = 60Hz$.

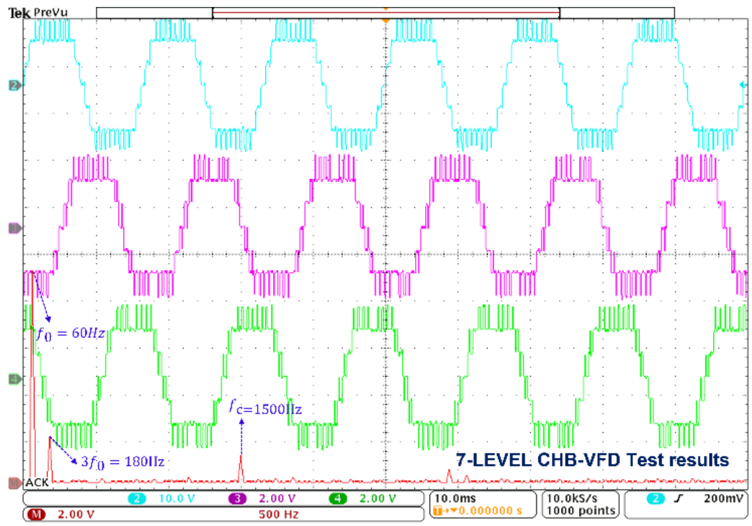

Figure 4. 21 : Synchronized switched waveforms obtained from a single 7-level CHB VFD ; $f_c = 1.5kHz$; $f_0 = 60Hz$.

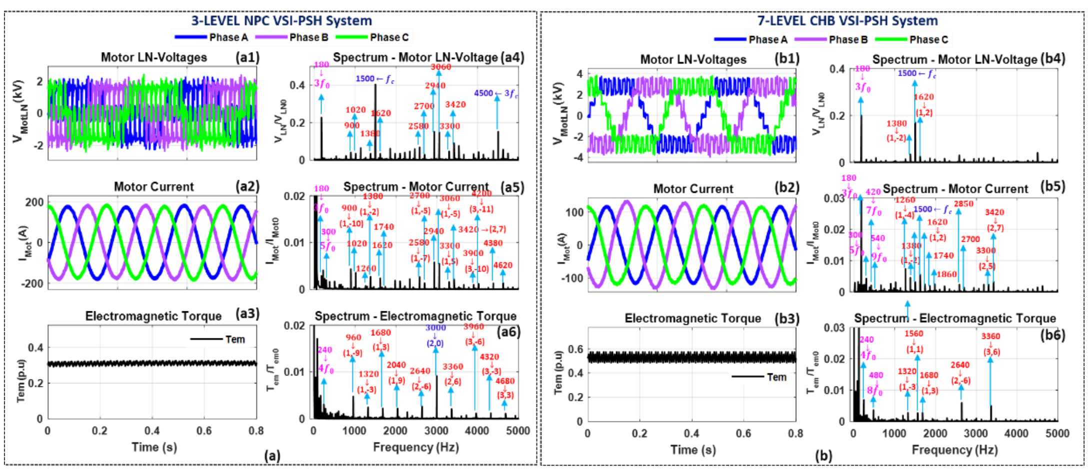

Figure 4. 22 : Sample Hybrid Experimental-Numerical Simulation results. (a) : Results a 3-Level NPC VSI system ; (b) Results a 7-Level CHB VSI

The exact locations of pertinent voltage and current harmonic components induced by each VFD topology are highlighted based on the actual value of the fundamental and carrier frequencies. That helps to show the family type of pulsating torque components they generate in the motor's airgap. It should be noted that the fundamental component has been removed in each motor voltage and current spectrum for a more precise analysis of harmonic locations. Examples of the 3-level NPC VFD-induced torsional stress components extracted from Figure 4.22(a) are summarized in Table 4.2, while those generated by the 7-level CHB VFD [Figure 4.22(b)] are outlined in Table 4.3. In both situations, it can be observed that all the torque harmonics generated are related to the harmonics produced by the VFD-induced currents, which can be expressed in terms of baseband and sideband components. The analysis reveals that two current harmonic components produce each fluctuating torque harmonic component, as predicted by the analytical expression provided in Section IV. A clear understanding of how torque is generated by voltage/current harmonics applied to the motor inputs is crucial in developing a Campbell diagram for a particular VFD topology to identify the operational motor speeds or fundamental frequencies where torsional excitation may occur.

Table 4. 2 : Example of motor air-gap torque harmonic families from a 3-Level NPC VSI system model

3-Level NPC VFD-Induced Torsional Stresses [Figure 22(a4)-(a6)]			
Current harmonics		Induced Torque harmonics	
Fundamental and baseband			
(3,0)	180 Hz = 3×60 Hz	(4,0)	240 Hz = 4×60Hz
(5,0)	300 Hz = 5×60 Hz		
Sideband harmonics around odd multiple of Carrier frequency			
(1, -4)	1260 Hz = $\lvert 1\times1500-4\times60 \rvert$	(1, -3)	1320 Hz= $\lvert 1\times1500-3\times60 \rvert$
(1, -2)	1380 Hz = $\lvert 1\times1500-2\times60 \rvert$		
(1, 2)	1620 Hz = $\lvert 1\times1500+2\times60 \rvert$	(1, 3)	1680 Hz= $\lvert 1\times1500+3\times60 \rvert$
(1, 4)	1740 Hz= $\lvert 1\times1500+4\times60 \rvert$		
Sideband harmonics around even multiple of Carrier frequency			
(2, -7)	2580 Hz = $\lvert 2\times1500-7\times60 \rvert$	(2, -6)	2640 Hz= $\lvert 2\times1500-6\times60 \rvert$
(2, -5)	2700 Hz = $\lvert 2\times1500-5\times60 \rvert$		
(2, 5)	3300 Hz = $\lvert 2\times1500+5\times60 \rvert$	(2, 6)	3360 Hz= $\lvert 2\times1500+6\times60 \rvert$
(2, 7)	3420 Hz = $\lvert 2\times1500+7\times60 \rvert$		

Table 4. 3 : Example of motor air-gap torque harmonic families from a 7-Level CHB VSI system model

<table>
<tr><th colspan="4">7-Level CHB VFD-Induced Torsional Stresses [Figure 22(b4)-(b6)]</th></tr>
<tr><th colspan="2">Current harmonics</th><th colspan="2">Induced Torque harmonics</th></tr>
<tr><td colspan="4">Baseband harmonics</td></tr>
<tr><td>(7,0)</td><td>420 Hz = 7×60 Hz</td><td rowspan="2">(8,0)</td><td rowspan="2">480 Hz = 8×60Hz</td></tr>
<tr><td>(9,0)</td><td>540 Hz = 9×60 Hz</td></tr>
<tr><td colspan="4">Sideband harmonics around odd multiple of Carrier frequency</td></tr>
<tr><td>(1, -4)</td><td>1260 Hz =∣1×1500-4×60∣</td><td rowspan="2">(1, -3)</td><td rowspan="2">1320 Hz=∣1×1500-3×60∣</td></tr>
<tr><td>(1, -2)</td><td>1380 Hz =∣1×1500-2×60∣</td></tr>
<tr><td>(1, 0)</td><td>1500 Hz</td><td rowspan="2">(1, 1)</td><td rowspan="2">1560 Hz=∣1×1500+1×60∣</td></tr>
<tr><td>(1, 2)</td><td>1620 Hz=∣1×1500+2×60∣</td></tr>
<tr><td colspan="4">Sideband harmonics around even multiple of Carrier frequency</td></tr>
<tr><td>(2, 5)</td><td>3300 Hz = ∣2×1500+5×60∣</td><td rowspan="2">(2, 6)</td><td rowspan="2">3360 Hz=∣2×1500+6×60∣</td></tr>
<tr><td>(2, 7)</td><td>3420 Hz = ∣2×1500+7×60∣</td></tr>
</table>

4.9. Conclusion article 3

A simple method to extract relevant electromagnetic torque components in a motor airgap supplied by VFDs has been developed in this chapter. It is based on a torque expression in the stationary and orthogonal reference frame and is suitable for both induction and synchronous motors. The Campbell lines of any inverter can be quickly mapped out when basic parameters such as the PWM carrier frequency and the machines operating range are known. The accuracy of the method has been confirmed on four parallel-connected two-level, NPC, and CHB VFD topologies, where simulation results match theoretical developments. The analysis and evaluation of the effects of VSI-induced harmonics on motor airgap pulsating torques under unbalanced conditions have been also conducted. The theoretical foundations presented in this chapter are intended to improve the understanding of PSH shaft element lifetime. More importantly, they are crucial for practicing engineers involved in the integration of large rotating shaft and performing torsional analysis as required per API 617, 672 and 673 standards for example. Therefore, the results of this investigation can be extended to other applications, such as large compressor drivetrains that are found in the oil and gas industry, or in milk and chapter industry.

The study enables the possibility to accurately predict the accelerated wear, fatigue, and premature failure of shaft mechanical elements. However, the study has some limitations that need further investigation.

1) The proposed study has been limited to conventional voltage source converters (VSCs) such as two-level, three-level neutral-point clamped, and seven-level cascaded H-bridge converters. However, it is essential to investigate the suitability and applicability of the proposed research in other VSCs, such as modular multilevel converters, which offer potential advantages for variable-speed PHSP applications compared to conventional power conversion technologies.
2) There are substantial incentives to decarbonize other industries that may utilize high-power variable speed drive systems (VSDSs) similar to the ones investigated in this chapter. For example, in the oil and gas industry, large steam and gas turbines driving compressors are increasingly being replaced by VFDs and motors. The power can easily reach 100MW. Consequently, the integration of the VSDS system into compressor drivetrains induces the risk to exciting the shaft Eigenmodes. This chapter does not cover learnings from other industrial applications.
3) The analysis in the chapter is limited to the PSH system configuration depicted in Figure 4.6(b), which employs a reversible power converter driving an induction

machine. However, extending this study to the PSH system configuration shown in Figure 4.6(c) is also essential, which involves using a Doubly fed induction machine (DFIM) that requires special attention in actual industrial Pumped Hydropower Storage systems. It is necessary to derive and discuss time-domain analytical expressions for the instantaneous pulsating torque components in a DFIM air gap when supplied by back-to-back VSIs.

CONCLUSION GÉNÉRALE

Discussion générale

Les travaux de cette thèse se sont focalisés sur le développement d'un ensemble d'outils dédiés à l'analyse et au diagnostic de la propagation des harmoniques électriques et électromagnétiques dans les entraînements électriques équipés de convertisseurs multiniveaux de type pont en H. Ces outils sont destinés aux ingénieurs et chercheurs en électronique industrielle, leur offrant la capacité de déterminer les fréquences harmoniques et inter harmoniques des tensions et courants générés par ce convertisseur, tant en conditions de fonctionnement normal qu'en conditions dégradées, ainsi que de prédire les composantes fréquentielles des couples pulsatoires produites dans les machines électriques. Une évaluation détaillée et rigoureuse, tant dans le domaine temporel que fréquentiel, des composantes du couple électromagnétique générées par ce convertisseur au niveau de l'entrefer des machines électriques a été effectuée.

La synthèse des travaux publiés dans le cadre de cette thèse, est résumée comme suit :

- **La première contribution scientifique (Article 1)** porte sur le développement d'une approche simplifiée de modélisation et de simulation pour évaluer la qualité de la puissance dans les pompes submersibles électriques alimentées par des variateurs de vitesse via un long câble de transmission. Les systèmes d'investigation concernent ceux utilisés dans les plateformes pétrolières. L'analyse de la qualité de puissance de ces systèmes en milieu industriel est souvent complexe. Dans cette publication, des étapes simples sont proposées pour réaliser des analyses d'intégration de ces systèmes, y compris l’analyse de la propagation des harmoniques. Un modèle simplifié de la fonction de commutation de l'onduleur multiniveau de type pont en H en cascade, en fonctionnement normal, est développé. Ce modèle ne nécessite pas une connaissance approfondie du fonctionnement de ce convertisseur et peut être facilement implémenté dans des logiciels de simulation courants, réduisant ainsi considérablement les efforts des ingénieurs et chercheurs lors de la phase de diagnostic des défaillances potentielles résultant d’une mauvaise qualité de puissance causée par cet onduleur.

- **La seconde contribution (Article 2)** présente une méthode graphique fondée sur la représentation spatiale 3D du vecteur de tension pour diagnostiquer les déséquilibres dans un onduleur triphasé en ponts en H (CHB) soumis à des conditions non idéales. En régime normal, la transformation de Clarke génère une trajectoire circulaire, signe d’un fonctionnement équilibré. En cas de défauts — tels que des déséquilibres de tensions continues ou des cellules défaillantes — cette trajectoire devient elliptique, traduisant un déséquilibre. Pour y remédier, l’article propose une stratégie de commande reposant sur un décalage généralisé du neutre, capable de compenser simultanément ces défauts sans distinction. Cette approche permet de maintenir des tensions et courants ligne-à-ligne équilibrés, même si les tensions de phase restent affectées. Des résultats de simulation et d’expérimentation sur un onduleur CHB à trois cellules par phase valident son efficacité. L’étude met également en évidence l’impact des conditions non idéales sur les spectres de tension et de courant, ce qui permet d'anticiper les modifications des spectres de couple électromagnétique dans l'entrefer des machines électriques.

- **La troisième contribution (Article 3)** définit un cadre d'étude et d'analyse des résonances de torsion d'excitation électromécanique liées aux convertisseurs statiques dans les stations de transfert d'énergie par pompage (STEP), ou « *pumped storage power plants* » (PSP) en anglais. Une vue d'ensemble des possibilités offertes par les convertisseurs statiques utilisés dans ces applications est présentée, ainsi qu'une estimation des fréquences des couples pulsants générés par chaque topologie de convertisseur et sa stratégie de modulation. Le calcul des fréquences harmoniques des couples pulsants pour les machines électriques alimentées par la topologie de convertisseur multiniveau de type pont en H, en fonctionnement normal et dégradé, est également proposé. De plus, une analyse approfondie de l'interaction électromécanique dans ces types de systèmes, en ce qui concerne les résonances de torsion, est menée.

Perspectives

Les outils d'analyses et les techniques commande suggérés dans cette thèse permettrons d'anticiper, surveiller et réduire leurs effets néfastes des harmoniques dans la phase de conception des convertisseurs actuels et futurs. Bien que ces outils de modélisation, d'analyse et de contrôle aient démontré leur utilité et leur efficacité pour améliorer la fiabilité et la sûreté de fonctionnement des convertisseurs multiniveaux de type pont en H, tant en modes normal que dégradé, certaines limitations subsistent et plusieurs axes de recherche nécessitent une exploration approfondie.

L'étude et les modèles proposés pour l'évaluation des harmoniques électriques et électromagnétiques dans les systèmes présentés dans cette thèse sont exclusivement développés pour l'analyse en régime permanent. En conséquence, les performances transitoires de ces systèmes, telles que les effets dynamiques du contrôleur sur le convertisseur ou les variations de charge, ne peuvent pas être évaluées avec les outils présentés dans cette thèse. Des recherches approfondies devront être menées à l'avenir pour développer de nouveaux modèles permettant d'évaluer et d'analyser la génération des harmoniques électriques et électromagnétiques dans l'interaction entre le convertisseur et la machine électrique durant les régimes transitoires.

De plus, l'analyse et l'évaluation des harmoniques dans le domaine fréquentiel présentées dans cette thèse sont basées sur la Transformée de Fourier Rapide (FFT). Toutefois, cette approche peut présenter des limitations lorsqu'il s'agit d'examiner le contenu fréquentiel d'un signal ou d'une grandeur évoluant au cours du temps. En particulier, l'utilisation de la FFT pour analyser les vibrations torsionnelles dans les machines électriques ne fournit pas toujours des informations complètes sur les causes des vibrations mesurées. Dans les cas où la fréquence des vibrations varie avec le temps, se limiter uniquement à l'analyse par FFT peut poser des problèmes. Par conséquent, il sera nécessaire d'envisager, à l'avenir, des études plus approfondies en utilisant des outils d'analyse plus avancés, tels que le spectrogramme, pour pallier cette limitation dans les applications où la fréquence des vibrations évolue au cours du temps.

L’étude proposée a été limitée aux convertisseurs multiniveaux de type pont en H. Toutefois, il est impératif d'élargir cette investigation pour évaluer la pertinence et l'applicabilité des modèles et outils d’analyse proposés aux convertisseurs multiniveaux modulaires (MMC). Les MMC présentent des avantages significatifs dans des domaines tels que les industries pétrolières et gazières, ainsi que pour les applications de transfert d'énergie par pompage. Par rapport aux convertisseurs en pont en H, les MMC offrent des améliorations notables en termes de qualité de la puissance, de flexibilité opérationnelle, de fiabilité et de performance globale. Il est donc essentiel de mener une analyse approfondie pour déterminer leur adéquation dans les contextes étudiés.

Enfin, des recherches futures sur l’intégration de modèles et d’outils basés sur l’intelligence artificielle (IA) pour l’analyse des effets des harmoniques dans les systèmes d’entraînement électrique à convertisseurs statiques sont envisagées. Ces modèles d’IA représentent une avancée significative pour la gestion et l’optimisation des performances de ces systèmes. Les techniques d’IA, telles que les réseaux de neurones et les algorithmes d’apprentissage automatique, offriront une amélioration substantielle de la précision des prévisions concernant la propagation des harmoniques électriques et mécaniques dans ces systèmes.

REFERENCES

[1] A. Alili, M.B. Camara, B. Dakyo, J. Raharijaona, “Power Electronic Converters Review for Wind Turbine Applications : State of Art, Reliability and Trends”. Paper presented at GREEN 2020 conference, IARIA, pp.12-18, Valencia, 21 – 25 Nov 2020.

[2] F. Blaabjerg and K. Ma, “Future on Power Electronics for Wind Turbine Systems” in IEEE Journal of Emerging and Selected Topics in Power Electronics, vol. 1, no. 3, pp. 139-152, Sept. 2013.

[3] J. Song-Manguelle, ‘’Convertisseurs multiniveaux asymétriques alimentés par transformateurs multi-secondaires basse-fréquence’’ Lausanne : École Polytechnique Fédérale de Lausanne, 2004.

[4] T. A. Meynard and H. Foch, “Multi-level conversion : high voltage choppers and voltage-source inverters,” in PESC ’92 Record. 23rd Annual IEEE Power Electronics Specialists Conference, pp. 397–403 vol.1, June 1992. 1.2.2

[5] L. G. Franquelo, J. Rodriguez, J. I. Leon, S. Kouro, R. Portillo, and M. A. M. Prats, “The age of multilevel converters arrives,” IEEE Industrial Electronics Magazine, vol. 2, pp. 28–39, June 2008. 1.2.2.

[6] J. Rodriguez, J.-S. Lai, and F. Z. Peng, “Multilevel inverters : a survey of topologies, controls, and applications,” IEEE Transactions on Industrial Electronics, vol. 49, pp. 724–738, Aug 2002. 1.2.2, 2.2.4.1.

[7] M. Barnes and A. Beddard, “Voltage Source Converter HVDC Links– The State of the Art and Issues Going Forward,” Energy Procedia, vol. 24, pp. 108– 122, 2012. 1.2.2, 1.2.2.

[8] A. Rufer, M. Veenstra, and K. Gopakumar. Asymmetric multilevel converter for high resolution voltage phasor generation. EPE’99.

[9] B. Ge, F. Z. Peng, and Y. Li, “Multilevel Converter/Inverter Topologies and Applications,” *Power Electronics for Renewable Energy Systems, Transportation and Industrial Applications,* ch14, 2014, pp. 422–462, doi :10.1002/9781118755525.

[10] J.-S Lai, and F.Z. Peng, “Multilevel converters-a new breed of power converters,” *Thirtieth IAS Annual Meeting*, IAS’95, pp. 2348–2356, 1995.

[11] Abuzaid Saeed Gadalla, Xiangwu Yan, Hashim Hasabelrasul, “Performance of the battery energy storage systems based on cascaded H-bridge multilevel converter,” *The Journal of Engineering*, vol.2019, no.16, pp.779-783, 2019.

[12] M. Hagedorn, M. Lorenz, and A. Mertens, “Cascaded H-Bridge Converter Designs for

Future Short-Range All-Electric Aircraft Propulsion," *2022 24th European Conference on Power Electronics and Applications (EPE'22 ECCE Europe)*, pp.1-10, 2022.

[13] J. Ebersberger, M. Hagedorn, M. Lorenz, A. Mertens, "Potentials and Comparison of Inverter Topologies for Future All-Electric Aircraft Propulsion," *IEEE Journal of Emerging and Selected Topics in Power Electronics*, vol.10, no.5, pp.5264-5279, 2022.

[14] G. Frequente, C. Nevoloso, G. Schettino, and M. Caruso, "Power Losses Comparison of Multilevel Asymmetrical and Symmetrical Power Converters for IPMSM Drives," *2024 6th Global Power, Energy and Communication Conference (GPECOM)*, pp.256-262, 2024.

[15] S. Lee, Y. Yang, Y. P. Siwakoti and Reza Barzegarkhoo, "Improved Cascaded H-Bridge Multilevel Inverters with Voltage-Boosting Capability," *Electronics*, 2021, 10(22), 2801

[16] J.-M. De Paris, C. R. D. Osorio, H. Pinheiro, and F. de Morais Carnielutti, "Phase disposition modulation with sorting algorithm for symmetrical cascaded multilevel converters," *IEEE Trans. Ind. Electron*, vol. 55, no. 6, pp. 7527–7536, 2019.

[17] F. Simonetti, A. D'Innocenzo, C. Cecati, "Simple Explicit Solution of Finite Control Set Model Predictive Control for Cascaded H-Bridge Inverters," *IEEE Transactions on Industrial Electronics*, vol.71, no.8, pp.9620-9630, 2024.

[18] T. Sornsadaeng, P. Chanhom, D. Amorndechaphon, S. Sirisukprasert, "A Strategy for Neutral Voltage Modulation Ensuring Fault Tolerance in CHB Multilevel Inverters With Reduced CMV and Unbalanced DC Sources," *IEEE Access*, vol.12, pp.154138-154159, 2024.

[19] Vikas Deep Juyal, Dr. Sudha Arora "Power Quality Improvement of a System using Three Phase Cascaded H-Bridge Multilevel Inverters" *2016 International Conference on Recent Advances and Innovations in Engineering (ICRAIE)*, Jaipur, India, 2016.

[20] A. Yadav and S. Chandra "Cascaded H-Bridge Based Multilevel Inverter for Power Quality Issues, "In : Kumar, J., Jena, P. (eds) Recent Advances in Power Electronics and Drives. Lecture Notes in Electrical Engineering, vol 707. Springer, Singapore. https://doi.org/10.1007/978-981-15-8586-9_10.

[21] M. Salman, A. Basit, M. S. Khalid, A. Qamar, "Reduction in Total Harmonic Distortion of Cascaded H-Bridge Multilevel Inverter with Using Phase Method," *2018 Clemson University Power Systems Conference (PSC)*, pp.1-6, 2018.

[22] T. Hoevenaars, I. Evans, and A. Lawson, "New marine harmonic standards," *IEEE Ind. Appl. Mag.*, vol. 16, no. 1, pp. 16–25, Jan. 2010. doi :10.1109/MIAS.2009.934965.

[23] N. Subramanian, Albert Alexander Stonier, "A Comprehensive Review on Selective Harmonic Elimination Techniques and Its Permissible Standards in Electrical Systems", *IEEE Access*, vol.12, pp.141966-141998, 2024.

[24] Q. Awais, M. Jamil, G. M. Hashmi, Z. A. Syed, "Harmonics in Adjustable Speed Drives : Causes, Effects, and Solutions," In Proceedings of the International Conference on Information and Emerging Technologies, Karachi, Pakistan, 6–7 July 2007

[25] T. Taufik, M. Muscarella, and D. Sawitri, "Power quality analysis of variable frequency drives connected to a reactively compensated mixed load system," *2016 International Seminar on Application for Technology of Information and Communication (ISemantic)*, pp.261-266, 2016.

[26] I. Dewayalage, D. A. Robinson, S. Elphick, and S. Perera, "Measurement of High-Frequency Voltage Harmonics above 2 kHz in High-Voltage Networks," *Energies*, vol.17, no.4, pp.892, 2024.

[27] G. Sinha, C. Hochgraf, R. H. Lasseter, D. M. Divan, and T. A. Lipo, "Fault protection in a multilevel inverter implementation of a static condenser," *IEEE IAS Annual Meeting, Conf.*, pp. 2557-2564, 1995.

[28] S. Wei, B. Wu, F. Li, and X. Sun, "Control method for cascaded H-bridge multilevel inverter with faulty power cells," *in Proc. IEEE Applied Power Electronics Conf.*, Miami, FL, Vol. 1, pp. 261-267, Feb. 2003.

[29] S. Khomfoit, and L. M. Tolbert, "Fault detection and reconfiguration technique for cascaded H-bridge 11-level inverter drives operating under faulty condition," *in Proc. Power Electronics and Drive Systems, PEDS'07*, pp. 1035–1042, Nov. 2007.

[30] T.Z. Wang, J.H. Zhang, H. Wang, and Y. Wang, "A Multi-Mode Fault-Tolerant Control Strategy for Cascaded H-Bridge Multilevel Inverters," *IET Power Electron.* 2020, *13*, 3119–3126.

[31] F. Zhang, et al, "A Fault-Tolerant Control Method Based on Reconfiguration SPWM Signal for Cascaded Multilevel IGBT-Based Propulsion in Electric Ships," *Journal of Marine Science and Engineering*, 10.3390/jmse12030500, 12, 3, (500), (2024).

[32] W. Wang, et al, "A Fast and Generalized Space-Vector Modulation Scheme for Cascaded H-bridge Multilevel Converters Under Faulty Conditions," *2023 11th International Conference on Power Electronics and ECCE Asia (ICPE 2023 - ECCE Asia)*, pp.1066-1071, 2023.

[33] H. Lin, et al, "A Flexible Space Vector Modulation Scheme for Cascaded H-Bridge

Multilevel Inverters Under Failure Conditions," *IEEE Transactions on Industrial Electronics*, vol.69, no.12, pp.11856-11867, 2022.

[34] J. Holtz, "Pulsewidth Modulation—A Survey," IEEE Trans. Ind. Electron., vol. 39, no. 5, pp. 410–420, 1992.

[35] R. Naderi and A. Rahmati, "Phase-shifted carrier PWM technique for general cascaded inverters," *IEEE Trans. Power Electron*., vol. 23, no. 3, pp. 1257–1269, 2008.

[36] P. Omer, J. Kumar, and B. S. Surjan, "Comparison of multicarrier PWM techniques for cascaded H-bridge inverter," *2014 IEEE Students' Conf. Electr. Electron. Comput. Sci. SCEECS* 2014, no. July 2016, 2014.

[37] Nihal C. Khaire, Madhuri A. Chaudhari, Rohit Kumar, "Fault-Tolerant Operation of 3-Phase 7-Level CHBMLI with Modified Neutral Point Shift Method," *2022 Second International Conference on Power, Control and Computing Technologies (ICPC2T)*, pp.1-6, 2022.

[38] S. M. Kim, J. S. Lee and K. B. Lee, "Fault-tolerant strategy using neutral-shift method for cascaded multilevel inverters based on level-shifted PWM," *In Proc. 9th International Conference on Power Electronics and ECCE Asia (ICPE-ECCE Asia)*, Seoul, 2015, pp. 1327-1332.

[39] R. Babaloo, M. Fathi, E. Afjei, and A. Siadatan, ''A new fault tolerant method for cascaded H-bridge inverters based on peak reduction post-fault control method,'' *in Proc. 10th Int. Power Electron., Drive Syst. Technol. Conf. (PEDSTC)*, Shiraz, Iran, Feb. 2019, pp. 671–676, doi : 10.1109/PEDSTC.2019.8697880.

[40] A. Raki, Y. Neyshabouri, H. Iman-Eini, and M. Aslanian, ''Reduction of common-mode voltage in cascaded H-bridge inverter under faulty conditions,'' in Proc. 30th Int. Conf. Electr. Eng. (ICEE), Tehran, Iran, May 2022, pp. 909–914, doi : 10.1109/ICEE55646.2022.9827146.

[41] W. Wang, Y. Zhang, C. Xiao, Y. Li, C. Ma, J. Liu, ''A Fast and Generalized Space-Vector Modulation Scheme for Cascaded H-bridge Multilevel Converters Under Faulty Conditions,'' *2023 11th International Conference on Power Electronics and ECCE Asia (ICPE 2023 - ECCE Asia)*, pp.1066-1071, 2023.

[42] D. Xie, C. Lin, H. Lin, W. Liu, Y. Du, T. Basler, ''OC Switch Fault Diagnosis, Pre- and Postfault DC Voltage Balancing Control for a CHBMC Using SVM Concept,'' *IEEE Transactions on Power Electronics*, vol.39, no.1, pp.677-692, 2024.

[43] M. Alathamneh, H. Ghanayem, E. Muljadi, R. M. Nelms, "A Comparative Study of

Conventional Pumped-Storage Hydropower (C-PSH) and Ternary Pumped-Storage Hydropower (T-PSH) Systems Integrated with Wind Generation," *4th International Conference on High Voltage Engineering and Power Systems (ICHVEPS)*, pp.630-635, 2023.

[44] Ding, L. ; Li, W.Y. ; Zargari, N.R. ; Paes, R, "Sensorless Control of CSC-Fed PMSM Drives with Low Switching Frequency for Electrical Submersible Pump Application," *IEEE Trans. on Ind. Appl.* 2020, *56*, 3799-3808.

[45] Fonsêca, D.A. ; Salazar, A.O. ; Villarreal, E.R. ; Espinoza, G.A., "Downhole Telemetry Systems to Monitor Electric Submersible Pumps Parameters in Oil Well," *IEEE Access* 2021, 9, 12824 - 12839.

[46] Romero, O.J. ; Hupp, A, "Subsea Electrical Submersible 1 Pump Significance in Petroleum 2 3 Offshore Production," *J. Energy Resour. Technol*. 2013, 00, pp.1 - 8.

[47] Cortes, B. ; Araujo, L.R. ; Penido, D.R., "Electrical submersible pump system model to assist oil lifting studies," *J. of Petrol. Sci. and Eng*. 2019, 174, 1279 - 1289.

[48] Smith, J.R. ; Grant, D.M. ; Al-Mashgari, A., "Slater, R.D, "Operation of subsea electrical submersible pumps supplied over extended length cable systems," *IEE Proc. Electr. Power Appl*. 2000, 147, 544 - 552.

[49] Allen-Bradley, "PowerFlex Medium Voltage AC Drives Bulletin Numbers 6000G, 6000T, 7000A, 7000, and 7000L," Rockwell Automation : Canada, 2022.

[50] Liang, X. ; Kar, N.C. ; Liu, J, "Load Filter Design Method for Medium-Voltage Drive Applications in Electrical Submersible Pump Systems," *IEEE Trans. on Ind. Appl*. 2015, 51, 2017-2029.

[51] Liang, X. ; El-Kadri, A, "Operational Parameters Affecting Harmonic Resonance in Electrical Submersible Pump Systems," *in Canadian Journal of Electrical and Computer Engineering*. 2019, 42, 183 - 197.

[52] Gabor, T., "Electrical Submersible Pump Components and Their Operational Features. In Electrical Submersible Pumps," Manual, 2nd ed. ; Gabor, T. ; Elsevier, 2018 ; pp. 55–152.

[53] Pragale, R. ; Shipp, D.D., "Investigation of premature ESP failures and oil field harmonic analysis," *IEEE Trans. Ind. Appl*. 2018, 53, 3175–3181.

[54] Tamer, A. ; Shipp, D. ; Dionise, T., "Reducing Electrical Submersible Pump Downtime by Mitigation of VSD Output Power Quality Problems," *In Proceedings of the IEEE Petroleum and Chemical Industry Committee Conference (PCIC)*, Vancouver, BC, Canada, 09-12 September 2019.

[55] Weixiong, J. ; Honghui, W. ; Guijie, L. ; Yonghong, L. ; Baoping, C. ; Zhixiong, L., "A Novel Method for Mechanical Fault Diagnosis of Underwater Pump Motors Based on Power Flow Theory," *IEEE Trans. Instr*. Meas. 2021, 70, 1 - 17.

[56] Rabbi, S.F. ; Kahnamouei, J.T. ; Liang, X. ; Yang, J., "Shaft Failure Analysis in Soft-Starter Fed Electrical Submersible Pump Systems," *IEEE Open J. Ind. Appl*. 2019, 1, 1 - 10.

[57] Neumann, K.C. ; La, D. ; Yoo, H. ; Burkepile, E., "Programmable Autonomous Water Samplers (PAWS) : An inexpensive, adaptable and robust submersible system for time-integrated water sampling in freshwater and marine ecosystems," *Sciences Direct*. 2022, 13, 1 - 14.

[58] Farbis, M. ; Hoevenaars, A.H., "Greenwald, J.L. Oil field retrofit of ESPs to Meet Harmonic Compliance," *In Proceedings of the IEEE Petroleum and Chemical Industry Technical Conference (PCIC)*, San Francisco, CA, USA, 08-10 September 2014.

[59] Hoevenaars, A.H. ; McGraw, M. ; Alexander, J., "Rightsizing Generators Through Harmonic Mitigation Realizes Energy, Emissions, and Infrastructure Reductions," *IEEE Trans. Ind. Appl*. 2017, 53, 675–683.

[60] Song-Manguelle, J. ; Ekemb, G. ; Mon-Nzongo, D. ; Tao, J. ; Doumbia, M.L., "A Theoretical Analysis of Pulsating Torque Components in AC Machines with Variable Frequency Drives and Dynamic Mechanical Loads," *IEEE Trans. Ind. Electron*. 2018, 65, 9311–9324.

[61] Pindoriya, R.M. ; Thakur, R.K. ; Rajpurohit, B.S. ; Kumar, R., "Numerical and Experimental Analysis of Torsional Vibration and Acoustic Noise of PMSM Coupled with DC Generator," *IEEE Trans. Ind. Electron*. 2022, 69, 3345 - 3356.

[62] Ekemb, G. ; Slaoui-Hasnaoui, F. ; Song-Manguelle, J. ; Lingom, M.P. ; Fofana, I., " Instantaneous electromagnetic torque components in synchronous motor fed by load-commutated inverters," *Energies*. 2021, 14, 1 - 25.

[63] Nassif, A.B., "Assessing the Impact of Harmonics and Interharmonics of Top and Mudpump Variable Frequency Drives in Drilling Rigs," *IEEE Trans. Ind. Appl*. 2019, 55, 5574 - 5583.

[64] API Standard 617, Axial and Centrifugal Compressors and Expander-Compressors, 8th ed. ; API : Englewood, CO, USA, 2016.

[65] API Standard 672, Packaged, Integrally Geared Centrifugal Air Compressors for Petroleum, Chemical, and Gas Industry Services, 5th ed. ; API : Englewood, CO, USA, August 2019.

[66] API. API Standard 673, Centrifugal Fans for Petroleum, Chemical and Gas Industry Services, 3rd ed. ; API : Englewood, CO, USA, December 2014.

[67] API. API Standard 684, Paragraphs Rotodynamic Tutorial : Lateral Critical Speeds, Unbalance Response, Stability, Train Torsional, and Rotor Balancing, 2nd ed. ; API Recommended Practice 684 ; API : Englewood, CO, USA, August 2005.

[68] Xiaodong, L. ; El-Kadri, A., "Operational Parameters Affecting Harmonic Resonance in Electrical Submersible Pump Systems," *Canadian Journal of Electrical and Computer Engineering*. 2019, 42, 183 - 197.

[69] Ong, C.M., "Dynamic Simulation of Electric Machinery Using Matlab/Simulink," *Canadian Journal of Electrical and Computer Engineering* 2019, 42, 183 - 197.

[70] Song-Manguelle, J. ; Sihler, C. ; Nyobe-Yome, J.M., "Modeling of Torsional Resonances for Multi-Megawatt Drives Design," *IEEE Trans. Ind. Electron*. 2018, 65, 9311–9324.

[71] Lingom, P.M. ; Song-Manguelle, J. ; Doumbia, M.L. ; Flesch, R.C. ; Tao, J., "Modeling Electrical Submersible Pumps : A System Modeling Approach for Power Quality Analysis with Variable Frequency Drives," *IEEE Trans. Power. Electron*. 2022, 37, 7039– 7054.

[72] Liang, X., "Linearization approach for modeling power electronics devices in power systems," *IEEE J. Emerg. Sel. Topics Power Electron*. 2014, 2, 1003–1012.

[73] Han, X. ; Palazzolo, A.B., "VFD machinery vibration fatigue life and multi-level inverter effect," *IEEE Trans. Ind. Appl*. 2013, 49, 2562–2575.

[74] Feletto, F. ; Durham, R.A. ; Bortoni, E.C. ; X. ; Costa, J.G., "Improvement of MV Cascaded H-Bridge Inverter (CHBI) VFD Availability for High-Power ESP Oil Wells," *IEEE Trans. Ind. Appl*. 2018, 55, 1006 - 1011.

[75] Busacca, A. ; Di Tommaso, A.O. ; Miceli, R. ; Nevoloso, C. ; Schettino, G. ; Scaglione, G. ; Viola, F. ; Colak, I., "Switching Frequency Effects on the Efficiency and Harmonic Distortion in a Three-Phase Five-Level CHBMI Prototype with Multicarrier PWM Schemes : Experimental Analysis," *Energies*. 2022, 15, 586.

[76] Qin, F. ; Gao, F. ; Tang, Y. ; Wang, J. ; Xu, T., "Comprehensive comparisons between six-arm and nine-arm modular multilevel converter," *CPSS Trans. Power Electron. Appl*. 2020, 5, 135 - 146.

[77] Anderson, J.A. ; Zulauf, G. ; Kolar, J.W. ; Deboy, G., "New Figure-of-Merit Combining Semiconductor and Multi-Level Converter Properties," *IEEE Open J. Power Electron*. 2020, 1, 322 - 338.

[78] Yifei, L. ; Fei, X. ; Wang, B. ; Binli, L., " Failure Analysis of Power Electronic Devices

and Their Applications under Extreme Conditions," *Chinese J. Electrical Engineering*. 2016, 2, 91-100.

[79] Holmes, D.G. ; Lipo, T.A., "PulseWidth Modulation for Power Converters, Principles and Practice," *IEEE Press* : Piscataway, NJ, USA, 2003.

[80] Gary, W.C. ; Shin-Kuan, C., "An Analytical Approach for Characterizing Harmonic and Interharmonic Currents Generated by VSI-Fed Adjustable Speed Drives," *IEEE Trans. Power. Delivery*. 2005, 20, 2585–2593.

[81] Soltani, H. ; Davari, P. ; Zare, F. ; Blaabjerg, F., "Effects of Modulation Techniques on the Input Current Interharmonics of Adjustable Speed Drives," *IEEE Trans. Ind. Electron*. 2018, 65, 165–178.

[82] Hota, A. ; Agarwal, V., "Novel Three-Phase H10 Inverter Topology with Zero or Constant Common-Mode Voltage for Three-Phase Induction Motor Drive Applications," *IEEE Trans. Ind. Electron*. 2022, 69, 7522–7525.

[83] Xiaoling, X. ; Xiongfei, W. ; Dong, L. ; Blaabjerg, F. ; Chengyong, Z., "Common-Mode Insertion Indices Compensation with Capacitor Voltages Feedforward to Suppress Circulating Current of MMCs," *CPSS Trans. Power. Electron. Appl*. 2020, 5, 103–113.

[84] Lipo, T.A., "Introduction to AC Machine Design ; Series on Power Engineering," Wiley-*IEEE Press* : Hoboken, NJ, USA, 2017.

[85] IEEE. Std 1159-2019 IEEE Recommended Practice for Monitoring Electric Power Quality: Piscataway, New York, NY, USA 2019.

[86] NEMA Std and Publication MG-1-2009 Motor and Generators ; National Electrical Manufacturers Association: Rosslyn 2019.

[87] A. Salem, H. V. Khang, K. G. Robbersmyr, M. Norambuena and J. Rodriguez, "Voltage source multilevel inverters with reduced device count: Topological review and novel comparative factors," IEEE Trans. Power Electron. vol. 36, pp. 2720–2747, 2021.

[88] S. Rahman et al, "A Combinational Level-Shifted and Phase-Shifted PWM Technique for Symmetrical Power Distribution in CHB Inverters," IEEE J. Emerg. Sel. Top. Power Electron., vol. 11, no. 1, pp. 932–941, Feb. 2023.

[89] Hussein Mahdi, Bjarte Hoff, Trond strem, "A Review of Power Converters for Ships Electrification," IEEE Trans. Power Electron. vol.38, no.4, pp.4680-4697, 2023.

[90] J. Song-Manguelle, T. Thurnherr, S. Schröder, A. Rufer, and J.-M. Nyobe-Yome, "Re-generative asymmetrical multi-level converter for multimegawatt variable speed drives," in Proc. IEEE Energy Convers. Congr. Expo., 2010, pp. 3683–3690.

[91] J. Tian, et al, “Individual DC voltage balance control for cascaded H-bridge electronic power transformer with separated DC-link topology,” IEEE Access, 2019, 7, 38558–38567.

[92] A. M. Rauf, M. Abdel-Monem, G. O. Hegazy, “A Review on Multilevel Converters for Efficient Integration of Battery Systems in Stationary Applications,” Energies., 2023, vol. 16, no. 10, pp.4133; https://doi.org/10.3390/en16104133.

[93] M. Meraj et al, “Novel Level Shifted PWM Technique for Unequal and Equal Power Sharing in Quasi Z-Source Cascaded Multilevel Inverter for PV Systems,” IEEE J. Emerg. Sel. Top. Power Electron., vol. 11, no. 4, pp. 932–941, Aug. 2023

[94] S. Rivera, S. Kouro, B. Wu, J. Leon, J. Rodriguez, and L. Franquelo, “Cascaded H-bridge multilevel converter multistring topology for large scale photovoltaic system,” in Proc. IEEE Int. Symp. Ind. Electron., Jun. 2011, pp. 1837–1844.

[95] J. Lamb, and B. Mirafzal, “An Adaptive SPWM Technique for Cascaded Multilevel Converters with Time-Variant DC Sources,” IEEE Trans. Ind. Appl., 2016, 52, 4146–4156.

[96] J. Xiong, F. Zhou, Q. Li, “Soft-switching modulation of the multilevel cascaded H-bridge inverter under DC source fault,” IET Gen, Trans & Dist., 2021, https://doi.org/10.1049/gtd2.12105.

[97] P. M. Lingom, et al, “VFD-Induced Torsional Stresses in Pumped Hydropower Storage Applications,” IEEE Access., vol. 12, no. pp. 35984-360012024, 2024.

[98] Submersible Pump Engineering, “Unbalanced currents and submersible motors,” SMENG, 2002, 1–2.

[99] S. P. Gautam, M. Jalhotra, L. K. Sahu, M. R. Kumar, and K. K. Gupta, “A Survey on Fault Tolerant and Diagnostic Techniques of Multilevel Inverter,” IEEE Access, vol. 11, pp. 608666–60888, 2023.

[100] I. Marzo, A. Sanchez-Ruiz, J. A. Barrena, G. Abad, and I. Muguruza, “Power Balancing in Cascaded H-Bridge and Modular Multilevel Converters Under Unbalanced Operation: A Review,” IEEE access, vol. 9, 110525-110543, 2021.

[101] Y. Cho, T. Labella, J. S. Lai, and M. K. Senesky, “A carrier-based neutral voltage modulation strategy for multilevel cascaded inverters under unbalanced DC sources,” IEEE Trans. Ind. Electron., 2014, vol. 61, no. 2, pp. 625–636, 2014.

[102] Z. B. Ye, and T. T. Wang, “A PWM strategy based on state transition for cascaded H-bridge inverter under unbalanced DC sources,” IEEE J. Emerg. Sel. Top. Power Electron., pp.

1686–1700, 2020.

[103] J. Kim, and Y. Cho, “Neutral voltage modulation for maximizing the linear modulation region and limp-home mode operation of multilevel cascaded inverters under DC-Link imbalance conditions,” IEEE Access vol. 10, pp. 13515-13524, 2022.

[104] Z. Xia, Q. Wu, Z. Ye, D. Yu, L. Zhu, and W. Hu, “A Novel DC-Power Control Method for Cascaded Converter under DC Voltage-Imbalance Condition,” Journal of Electrical and Computer Engineering, 2022.

[105] B. Xiao, L. Hang, J. Mei, C. Riley, L. M. Tolbert, and B. Ozpineci, “Modular cascaded h-bridge multilevel PV inverter with distributed MPPT for grid-connected applications,” IEEE Trans. Ind. Appl., vol. 51, no. 2, pp. 1722–1731, 2015.

[106] Y. Yu, G. Konstantinou, C. D. Townsend, and V. G. Agelidis, “Comparison of zero-sequence injection methods in cascaded H-bridge multilevel converters for large-scale photovoltaic integration,” IET Renewable Power Gener., vol. 11, no. 5, pp. 603–613, May 2017.

[107] S. Rahimpour, O. Husev, D. Vinnikov, and V. N. Kurdkandi, H. Tarzamni, “Fault management techniques to enhance the reliability of power electronic converters: An overview,” IEEE Access, vol. 11, pp. 13432–13446, 2023.

[108] O. Lopez, T. Komrska, J. Alvarez, and J. Adam, “Post-fault operation strategy for cascaded H-Bridge inverters driving a multi-phase motor,” IEEE Trans. Ind. Electron., 2024, 71,5, 4309–4319.

[109] P. Lezana, and G. Ortiz, “Extended operation of cascade multicell converters under fault condition,” IEEE Trans. Ind. Electron., vol. 56, pp. 2697–2703, 2009.

[110] W. Zhang, et al, “Survey on fault-tolerant techniques for power electronic converters,” IEEE Trans. Power Electron. vol. 29, no. 12, pp. 6319–6331. 2014.

[111] P. W. Hammond, “Enhancing the reliability of modular medium-voltage drives,” IEEE Trans. Ind. Electron., vol. 49, no. 5, pp. 948–954, 2002.

[112] F. Carnielutti, H. Pinheiro, and C. Rech, “Generalized carrier-based modulation strategy for cascaded multilevel converters operating under fault conditions,” IEEE Trans. Ind. Electron., vol. 59, no. 2, pp. 679–689, 2012.

[113] M. Aleenejad, H. Mahmoudi, and R. Amhadi, “Unbalanced space vector modulation with fundamental phase shift compensation for faulty multilevel converters,” IEEE Trans. Power Electron., vol. 31, no. 10, pp. 7225–7233, 2016.

[114] J. Lamb, B. Mirafzal, and F. Blaabjerg, “PWM common mode reference generation for

maximizing the linear modulation region of CHB converters in islanded microgrids," IEEE Trans. Ind. Electron., vol. 65, no. 7, pp. 5250–5259, Jul. 2018.

[115] Sharif Zadeh, M. ; Al-Haddad, K. "Packed E-Cell (PEC) converter topology operation and experimental validation," *IEEE Access*, 2019, 7, 93049-93061.

[116] Laib, A. ; Krama, A. ; Sahli, A. ; Kihal, A. ; Abu-Rub, H. "Reconfigurable Model Predictive Control for Grid Connected PV Systems Using Thirteen-Level Packed E-Cell Inverter," *IEEE Access*, 2022, 10, 102210-102222

[117] US Department of Energy, "Hydropower Basics," *Energy.gov*, Jan 5, 2023, www.energy.gov/eere/water/hydropower-basics.

[118] R. Uría-Martínez, M. Johnson, and R. Shan, "Hydropower Market Report," *U.S.* 2021.

[119] V. Koritarov, Q. Ploussard, J. Kwon, and P. Balducci, "A Review of Technology Innovations for Pumped Storage Hydropower," ANL-22/08, 2022, doi :10.2172/1867238.

[120] R. K. Mohanta, T. R. Chelliah, *et al*, "Sources of vibration and their treatment in hydro power stations – A Review," *Engineering Science and Technology, an International Journal*, vol. 20, pp. 637-648, 2017

[121] Y. Thakur, G. Goga b, V. Shrivastava. "Hydraulic-mechanical coupling vibration performance of pumped storage power station with two turbine units sharing one tunnel," *Journal of Energy Storage*, vol. 53, Sept. 2023.

[122] I. Ahmad, A. Rashid, I. Ahmad, A. Rashid, "On-line monitoring of hydro power plants in Pakistan," *Information Techn. Journal*, pp. 919–923, 2007.

[123] D. Momčilovi ć, Z. Odanovi, *et al*, "Failure analysis of hydraulic turbine shaft, Engineering Failure Analysis," *Engineering Failure Analysis*, vol. 20, pp 54–66, 2012.

[124] R. K. Mohanta. "Sources of vibration and their treatment in hydro power stations-A review," *Engineering Science and Technology, an International Journal.,* vol. 20, no. 2, pp.637-648, April 2017.

[125] I. Kougias, *et al*, "A review study on the improvement of stator frame design and prediction of electromagnetic vibration of hydro generators," *Renew Sustainable Energy Reviews*, Vol. 102, pp.96-110, March 2019.

[126] E. Georgievskaia, "Destruction of the hydraulic unit shaft : Why it is possible," *Forces in Mechanics*, vol. 4, pp. 1-10, 2021.

[127] R.M. Pindoriya, R. K. Thakur, B. S. Rajpurohit, and R. Kumar, "Numerical and experimental analysis of torsional vibration and acoustic noise of PMSM coupled with DC generator," *IEEE Trans. Ind. Electron.*, vol. 69, no. 4, pp. 3345–3356, Apr. 2022.

[128] W. Zhao, *et al*, “Investigation of Winding Configuration on Electromagnetic Vibration in Modular Dual Three-Phase PM Machine,” *IEEE Trans. Ind. Electron*., vol.71, no.2, pp.1257-1267, 2024.

[129] J. Song-Manguelle, S. Schröder, T. Geyer, G. Ekemb, and J. M. Nyobe-Yome, “Prediction of Mechanical Shaft Failures du taux Variable Frequency Drives,” *IEEE Trans. on Ind. Appl*., vol. 25, no. 4, pp. 130-138, Jan. 2010.

[130] G. Ekemb, J. Song-Manguelle, and J. M. Nyobe-Yome, “Instantaneous Electromagnetic Torque Components in Synchronous Motors Fed by Load-Commutated Inverters,” *Energies*, 2021, 14, 3223.

[131] M. Rossi, K. Elshawarby, M. Bruha, M. Mauri, M.S. Carmeli, and F. Castelli-Dezza, “Performance Evaluation Methods for VSD Control Systems Affected by Torsional Vibrations : Sensitivity and Energetic Analyses,” *2019 International Conference on Clean Electrical Power (ICCEP)*, pp.605-610, 2019.

[132] *American Petroleum Institute API standard 617*., Axial and Centrifugal Compressors and Expander-compressors, 8th ed., Errata 1, Aug. 2016.

[133] *American Petroleum Institute API standard 672*, Packaged, Integrally Geared Centrifugal Air Compressors for Petroleum, Chemical, and Gas Industry Services, 4th Ed. Errata 2, July 2010.

[134] *American Petroleum Institute API standard 672*, Centrifugal Fans for Petroleum, Chemical, and Gas Industry Services, 3rd Ed. Dec. 2014.

[135] S. P. Betoka Onyama, *et al*, “A Tool for Power Quality Assessment in Electric Submersible Pump Systems with Variable Frequency Drives” *Society of Petroleum Engineers (SPE) Guld coast section-Electric Submersible Pump Workshop*, the Woodlands, Texas, USA, Oct. 29-Nov. 2, 2023.

[136] T. Joseph *et al*, “Dynamic average converter model for MVDC link harmonic analysis,” *in Proc. IEEE Milan Power Tech*, 2019, pp. 1–6.

[137] T. Joseph *et al.*, “Analysis of harmonic transfer through an MVDC link,” in *Proc. 15th IET Int. Conf. AC DC Power Transmiss,* 2019, pp. 1–6.

[138] T. Sahrakorpi, A. Khosravi and M. E. H. Assad. “Design and performance optimization of renewable energy systems-Chapter 12, Hydropower,” *Academic Press*, ISBN. 978-0-12-821602-6, pp. 181-194, 2021.

[139] P. M. Lingom**,** *et al* “A Power Quality Assessment of Electrical Submersible Pumps Fed by Variable Frequency Drives under Normal and Failure Modes,” *Energies*., vol. 16, no.

4, pp. 1–34, July. 2023.

[140] H. Wang, O. Ahmed, B. Brennan, and B. Bellgraph, "Developing a digital twin for hydropower systems - an open platform framework," *Journal of Waterpower & Dam Construction Magazine*, vol. 81, no. 3, pp. 24-28, Nov. 2021

[141] A. Mirza, W. Chen, A. Nguyen, Y. Cao, and L. Hao, "Modeling Electrical Aging of Polyimide Kapton HN Under High-Voltage High-Frequency Pulse Waveforms," *IEEE Trans. On Diel and Elec Insul*, vol.29, no.6, pp.2394-2401, 2022.

[142] G. C. Montanari and L. Simoni, "Aging Phenomenology and modeling," *IEEE Trans. on Electrical Insulation*, vol. 28, no. 5, pp. 755-776, Oct. 1993.

[143] IEC 505, *Evaluation, and Identification of Electrical Insulation Systems. Part 1 : General Principles and Guide to Application*, 1975 ; IEC TC 63 (Sec.) 75, 1992.

[144] IEEE 1064, *IEEE Guide for Multifactor Stress Functional Testing of Electrical Insulation Systems*, 1991.

[145] M. Miner, "Cumulative Damage in Fatigue," *Journal of Applied Mech*., pp. 159-164, 1945.

[146] K. Hectors, "Cumulative Damage and Life Prediction Models for High-Cycle Fatigue of Metals : A Review," *Metals 2021*, vol. 11, no. 2, pp-4-32, 2021.

[147] F. Conti. *et al* "Vibration Signals for Condition Based Maintenance of Hydraulic Valves," *2021 IEEE International Workshop on Metrology for Industry 4.0 & IoT (MetroInd4.0&IoT)*

[148] R. Alimardani, A. Rahideh, S. H. Kia, "Mixed Eccentricity Fault Detection for Induction Motors Based on Time Synchronous Averaging of Vibration Signals," *IEEE Trans on Ind Electronics*, vol. 71, no.3, pp.3173-3181, 2024.

[149] B. Akin, S. Choi, U. Orguner, H. A. Toliyat, *etal*, "A Simple Real-Time Fault Signature Monitoring Tool for Motor-Drive-Embedded Fault Diagnosis Systems," *IEEE Trans. Ind. Electron*, vol. 58, no. 5, pp. 1990-2001, May 2001.

[150] M. E. H. Benbouzid. "A review of induction motors signature analysis as à medium for faults detection," *IEEE Trans. Ind. Electron*., vol. 47, no. 5, pp. 984–993, Oct. 2000.

[151] Xu Han, and A. Palazzolo, "VFD Machinery Vibration Fatigue Life and Multilevel Inverter Effect," *IEEE Trans. on Ind. Appl*., vol. 49, no. 6, pp. 2562-2575, Nov./Dec. 2013.

[152] D. G. Dorrell, W. T. Thomson, and S. Roach, "Analysis of airgap flux, current, vibration signals as a function of the combination of static and dynamic air gap eccentricity in 3-phase induction motors," *IEEE Trans. Ind. Appl*., vol. 33, no. 1, pp. 24–34, Jan./Feb. 1997.

[153] B. Akin, U. Orguner, H. A. Toliyat, and M. Rayner, "Low order PWM inverter harmonics

contributions to the inverter-fed induction machine fault diagnosis," *IEEE Trans. Ind. Electron*., vol. 55, no. 2, pp. 610–619, Feb. 2008

[154] Lin-Chuan Tsai, "Design and Implementation of a Three-Section Transmission Line Transformer," *Iranian Journal of Science and Technology, Transactions of Electrical Engineering*, 2018.

[155] C. M. Ong, "Dynamic Simulation of Electric Machinery using Matlab/Simulink," *Prentice Hall*, Perdue, 1999.

[156] P. M. Lingom, *et al*, "Electrical Submersible Pumps : A System Modeling Approach for Power Quality Analysis with Variable Frequency Drives," *IEEE Trans on Power Elec*, vol. 37, no. 6, pp.7039-7054, June 2022.

[157] J. Song-Manguelle, Ekemb, *et al*, "A Theoretical Analysis of Pulsating Torque Components in AC Machines with Variable Frequency Drives and Dynamic Mechanical Loads," *IEEE Trans. on Ind. Elec*, vol. 65, no. 12, pp. 9311-9324, Dec. 2018.

[158] K. R. Vasudevan, "Variable speed pumped hydro storage : A review of converters, controls and energy management strategies," *Renew and Sust Energ Rev*., vol.135, pp.110156, 2021.

[159] J. Anto, and R. C Thanga, "A Review of Power Electronic Converters for Variable Speed Pumped Storage Plants : Configurations, Operational Challenges, and Future Scopes," *IEEE Jour of Emerg and Select Topics in Power Elec*, vol. 6, no. 1, pp. 103-119, March 2018.

[160] D. Mon-Nzongo, G. Ekemb, J. Song-Manguelle, *et al*, "LCIs vs PWM-VSIs : A Torque Oriented Evaluation for Torsional Analysis Purpose," *IEEE Trans. on Power Elec*., vol. 34, no. 9, pp. 8956-8970, Sept. 2019.

[161] S. Schröder, *et al*, "Modular high-power shunt-interleaved drive system : A realization up to 35 MW for oil and gas applications," *IEEE Trans. on Ind. Appl*., vol. 25, no. 4, pp. 130-138, Jan. 2010.

[162] P. W. Hammond, "Enhancing the reliability of modular medium-voltage drives," *IEEE Trans. Ind. Appl.*, vol. 49, no. 5, pp. 948–954, Oct. 2002.

[163] F. Carnielutti, H. Pinheiro, and C. Rech, "Generalized carrier-based modulation strategy for cascaded multilevel converters operating under fault conditions," *IEEE Trans. Ind. Electron.*, vol. 59, no. 2, pp. 679–689, Feb. 2012.

[164] P. M Lingom, J. Song-Manguelle, D. La Mon-Nzongo, R. C. C. Flesch, and J. Tao, "Analysis, and control of PV cascaded H-bridge multilevel inverter with failed cells and

changing meteorological conditions," *IEEE Trans. Power Elec*., vol. 36, no. 2, pp. 1777–1789, 2020.

[165] P. M. Lingom, J. Song-Manguelle, M. L. Doumbia, *et al*, "A generalized modulation strategy for cascaded H-bridge multilevel inverter under unequal DC sources," *IEEE Energy Conversion Congress and Exposition (ECCE)*, Detroit, Michigan, USA, Oct. 9-13, 2022.

[166] D. G. Holmes, and T. A. Lipo "Pulse Width Modulation for Power Converters : Principle and Practice," *IEEE Press*, Series on Power Eng., Wiley Inter., 2003.

[167] S. Poster. "Challenges of Large Converter-Fed Synchronous Machines for Variable-Speed Pumped Hydro Storage," *Energies*., vol. 16, no. 22, pp. 2–18, Oct. 2023.

[168] S. Rahimpour, *et al,* "Fault management techniques to enhance the reliability of power electronic converters : An overview," *IEEE Access*, vol. 11, pp. 13432–13446, 2023.

ANNEXES

A.1. Synthèse des contributions scientifiques et industrielles

- ❑ **(05) Articles de Journaux**
  - **IEEE Journal of Emerging and Selected Topics in Power Electronics, 2025**
  - **IEEE Access, 2024**
  - **Energies MPIDI, 2023**
  - **IEEE Transactions on Power Electronics, 2022**
- ❑ **(06) Articles de conférences**
  - **IEMDC 2025**
  - **ECCE 2024, 2023, 2022**
  - **PEDS 2023**
- ❑ **(09)** Articles collatéraux comme interaction avec d'autres chercheurs
- ❑ **(02)** Subventions de recherche Mitacs Accélération-Project Industriels

A.2. Approbation bourse de recherche Mitacs pour un projet de recherche industrielle entre l'UQTR et C-Fer Technologies

September 1, 2021

Application Ref. IT25920

RE: Mitacs Accelerate Proposal

Project Title:	**A Simulation Tool for Power Quality of Electric Submersible Pumps (ESPPQST)**
Internship Supervisor(s):	**Mamadou Lamine Doumbia**
Intern(s):	**Fils Pascal Mpomboum Lingom, TBD**
Department:	**Département de génie électrique et génie informatique**
Institution:	**Université du Québec à Trois-Rivières**
Partner Organization:	**C-FER Technologies**

Dear applicants,

Your application to Mitacs Accelerate has successfully passed research review. Your **research project** has been approved for a total grant of $195,000.00 that will be delivered through **eligible internships**. Your internship should not start prior to confirmation of eligibility as outlined below:

1. Mitacs must receive partner funds before each internship start date to pay the intern(s) on time;
2. Project leads must confirm intern name(s) and start date(s). No costs for an internship can be incurred prior to the research project approval and the receipt of partner funds for the internship;
3. To identify a new intern, the Intern Profile form (including CV and memorandum) must be submitted to Mitacs before the applicable internship's start date and obtain Mitacs approval is/are required to conduct their activities.

All awards are subject to ongoing program eligibility, continuation of funding by the partner organization(s), and continuation of funding by our government partners. Mitacs-Accelerate gratefully acknowledges the financial support of the Government of Canada and the Government of Québec through the Ministère de l'Économie et de l'Innovation (MEI).

Welcome to Mitacs Accelerate. With this program, interns can apply their specialized expertise while companies gain a competitive advantage. We look forward to the success of your project.

If you have any questions, please contact Mariam Ladha, Grant Management Specialist, at mladha@mitacs.ca.

Sincerely,

R. Ben Mrad,

Ridha Ben Mrad
Chief Research Officer and Associate Academic Director

Enclosures:
- Appendix A: Referee comments
- Appendix B: Terms and Conditions of the Award
- Attachment: Intern Onboarding Information

A.3. Interface graphique développé pour l'analyse de la qualité de puissance dans les Pompes Electriques Submersibles

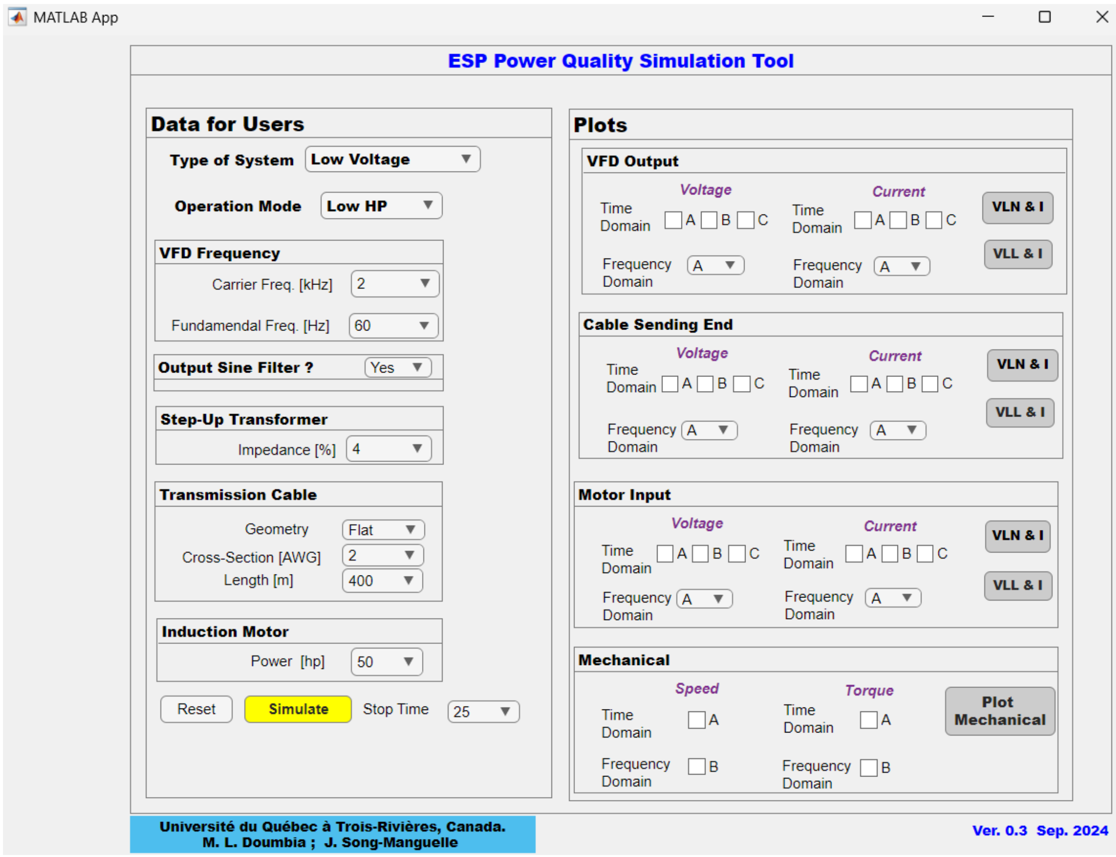

A.3. Approbation bourse de recherche Mitacs pour un projet de recherche industrielle entre l'UQTR et Opal-RT Technologies

August 11, 2022

Application Ref. IT31972

RE: Mitacs Accelerate Proposal

Project Title:	**Rapid control prototyping of adjustable speed drive systems for OPAL-RT coursewares with the OP8666 module**
Internship Supervisor(s):	**Mamadou Lamine Doumbia**
Co-Supervisor(s):	**Joseph Song-Manguelle**
Intern(s):	**Fils Pascal Mpomboum Lingom**
Department:	**Département de génie électrique et génie informatique, Département de génie électrique et informatique**
Institution:	**Université du Québec à Trois-Rivières**
Partner Organization:	**OPAL-RT Technologies Inc.**

Dear applicants,

Your application to Mitacs Accelerate has successfully passed research review. Your **research project** has been approved for a total grant of $30,000.00 that will be delivered through **eligible internships**. Your internship should not start prior to confirmation of eligibility as outlined below:

1. Mitacs must receive partner funds before each internship start date to pay the intern(s) on time;
2. Project leads must confirm intern name(s) and start date(s). No costs for an internship can be incurred prior to the research project approval and the receipt of partner funds for the internship;
3. To identify a new intern, the Intern Profile form (including CV and memorandum) must be submitted to Mitacs before the applicable internship's start date and obtain Mitacs approval

All awards are subject to ongoing program eligibility, continuation of funding by the partner organization(s), and continuation of funding by our government partners. Mitacs-Accelerate gratefully acknowledges the financial support of the Government of Canada and the Government of Québec through the Ministère de l'Économie et de l'Innovation (MEI).

Welcome to Mitacs Accelerate. With this program, interns can apply their specialized expertise while companies gain a competitive advantage. We look forward to the success of your project.

A.4. Modèle de simulation temps réel d’un système de conversion d’énergie éolienne de 2 MW avec DFIG et commande back-to-back développé dans le cadre du Project avec OPAL-RT